

**Phosphoinositides and Rho Proteins Conspire to
Spatially Regulate Actin Polymerization in Motile Cells**

by

Adriana Tiamae Dawes

A THESIS SUBMITTED IN PARTIAL FULFILMENT OF
THE REQUIREMENTS FOR THE DEGREE OF

Doctor of Philosophy

in

The Faculty of Graduate Studies

(Mathematics)

The University Of British Columbia

August 3, 2006

© Adriana Tiamae Dawes 2006

Abstract

Cells that move in response to an external signal are crucial for diverse physiological processes such as embryogenesis, neurogenesis, wound healing and immune surveillance. Motile cells are also implicated in disease processes such as rheumatoid arthritis and metastatic cancer. Polymerization of the protein actin, one of the three proteins in a cell's cytoskeleton, generates the force required to propel a cell in response to a stimulus. The goal of this thesis is to use mathematical modelling to gain a better understanding of how spatial asymmetries in signalling molecules are established and how these signalling molecules direct actin polymerization to produce characteristic actin densities and persistent directed motion.

As a first step in understanding the complicated signalling cascades activated by an external signal, I identify modules important for regulation of actin polymerization in motile cells. Based on experimental evidence, I focus on phosphoinositides (PIs), membrane-bound lipids that mediate sensing of external gradients, and Rho proteins, potent regulators of the actin cytoskeleton. I consider models of actin dynamics, Rho proteins and PIs in isolation based on known or observed biochemical events. I then formulate a combined model that simulates actin polymerization dynamics under the regulation of both PIs and Rho proteins. I base all the models proposed here on experimental observations that indicate how PIs and Rho proteins interact with each other and how they affect actin dynamics.

The models presented here generate behaviours consistent with experimental observations of both normal and mutant cells and suggest possible mechanisms for recent experimental observations. I show that a model based on biological evidence using reasonable parameter values gives rise to spatial profiles of signalling molecules and actin filaments that are consistent with experimental observations. I find that crosstalk between Rho proteins is required for maintenance of directed motion. I suggest how actin polymerization could be involved in the maintenance of the spatial gradients of PIs and propose experiments to test my hypothesis. These testable hypotheses can be used to guide experiments that could then be used to further refine the models

and shed light on the regulatory processes involved in cell motility.

Contents

Abstract	ii
Contents	iv
List of Tables	xi
List of Figures	xii
Acknowledgements	xvi
Co-authorship statement	xvii
1 Introduction and motivation	1
1.1 Introduction	1
1.2 Cell types studied	2
1.2.1 Fibroblasts and neutrophils	2
1.2.2 Neural growth cones	2
1.2.3 Keratocytes	4
1.3 Experimental techniques to study cell motility	5
1.3.1 Electron microscopy and gold particle tagging	5
1.3.2 Fluorescence imaging	6
1.3.3 Regulation of protein expression	7
1.4 Structure of a motile cell	7
1.4.1 Size scale of tens of microns	8
1.4.2 Size scale of ten microns	8
1.4.3 Size scale of one micron	8
1.4.4 Size scale of 0.1 microns	8
1.5 Cell repertoire of interest	9

1.5.1	Gradient detection	9
1.5.2	Polarization	9
1.5.3	Amplification and adaptation	9
1.5.4	Cytoskeletal remodelling and cell shape changes	10
1.5.5	Directed movement	10
1.6	Signalling cascade	10
1.7	Modelling cell movement in a 1D domain	14
1.8	General questions addressed in this thesis	15
1.9	Structure of the thesis	17
	}	
2	Introduction to actin and cell motility	22
2.1	Actin	22
2.1.1	Speed of actin polymerization	23
2.1.2	Force generation by actin polymerization	24
2.2	Actin Associated Proteins	26
2.2.1	Capping Proteins	27
2.2.2	Nucleating Proteins	27
2.2.3	Filament Depolymerizing Proteins	28
2.2.4	Sequestering Proteins	28
2.2.5	Time scales of actin dynamics	28
2.3	Signalling Molecules	29
2.3.1	Rho Proteins	29
2.3.2	Phosphoinositides	29
2.4	Stages of cell movement	30
2.4.1	Spatial asymmetries in signalling molecules	30
2.4.2	Cytoskeletal rearrangement	30
2.5	Observations of motile cells	32
3	Filament branching and protrusion velocity in a 1D model of a motile cell .	33
3.1	Regulation of actin polymerization in motile cells	33
3.1.1	Role of filament capping and decay	33
3.1.2	Role of Arp2/3 nucleation	34

3.1.3	Localization of Arp2/3 and barbed ends in motile cells	34
3.2	Previous modelling efforts	35
3.3	Questions to address	36
3.4	Assumptions about model geometry	36
3.5	Model definitions	37
3.6	Assumptions about actin dynamics	38
3.7	Model equations	39
3.7.1	Derivation of model equations using conservation laws	39
3.7.2	Model equations with kinetic terms	41
3.8	Analysis of travelling wave solutions: spontaneous branching	42
3.8.1	Membrane speed in terms of parameter values	46
3.8.2	Tip and side branching	46
3.9	Discussion	46
4	Dependence of membrane speed on biochemical rates	48
4.1	Simulations	48
4.1.1	Initial attempts	48
4.1.2	Successful computational algorithm	51
4.2	Parameter values	52
4.2.1	Rate of Arp2/3 branching	52
4.2.2	Rate of Arp2/3 diffusion	53
4.3	Results	54
4.3.1	Analytic and simulation results of spontaneous branching case agree	54
4.3.2	All three branching types support travelling wave solutions	54
4.3.3	Side branching provides best fit to experimental data	57
4.3.4	Dependence of membrane speed in biochemical rates	62
4.4	Discussion	66
5	Effect of retrograde flow on spatial profiles and membrane speed	69
5.1	Model incorporating retrograde flow	70
5.1.1	Analysis of modified model	71

5.2	Retrograde flow and Arp2/3 transport mechanism have little effect on the spatial profile of barbed ends, Arp2/3 and filament density	71
5.3	Discussion	76
6	Rho proteins and cell motility	77
6.1	Biological background	77
6.1.1	Small G proteins	77
6.1.2	Rho protein subfamily of small G proteins	78
6.1.3	Polarization and total concentration of the Rho proteins	79
6.1.4	GAPs, GEFs and GDIs regulate Rho protein activation	79
6.1.5	Role of Rho proteins in cell motility	80
6.1.6	Crosstalk between the Rho proteins	82
6.1.7	Theoretical models of Rho protein crosstalk	83
6.2	Observations and questions to address with a theoretical model	84
6.3	Spatial model of Rho protein dynamics	84
6.3.1	Model variables	84
6.3.2	Model assumptions	85
6.3.3	Model equations	86
6.4	Parameter values	89
6.5	Simulations	89
6.6	Results	91
6.6.1	Small G proteins establish stable spatial domains in response to a spatially graded input to Cdc42	91
6.6.2	Small G proteins establish stable spatial domains in response to a random input to Cdc42	93
6.6.3	Rho proteins establish domains on both sides of the cell in response to two stimuli	95
6.7	Discussion	97
7	Regulation of actin polymerization by Rho proteins in a 1D model cell . . .	98
7.1	Regulation of actin polymerization by Rho proteins	98
7.1.1	Cdc42 enhances nucleation by Arp2/3	99

7.1.2	Rac inhibits capping of barbed ends	99
7.2	Observations and questions to address with a model	99
7.3	Integrated model of Rho proteins and actin dynamics	100
7.3.1	Additional assumptions	100
7.3.2	Model equations	101
7.4	Parameters	103
7.5	Simulations	103
7.6	Results	105
7.6.1	1D cell model can initiate and maintain directed movement in response to a graded stimulus	105
7.6.2	Random stimuli cause the 1D cell model to initiate and maintain directed movement	108
7.7	Discussion	110
8	Phosphoinositides regulate Rho protein activation	111
8.1	Biological background	111
8.1.1	Phosphoinositides	111
8.1.2	Phosphatases and kinases regulate the phosphorylation state of the PIs	112
8.1.3	PIs regulate activation of Rho proteins	113
8.1.4	Rho proteins regulate phosphorylation state of the PIs	114
8.1.5	Role of phosphoinositides in cell motility	114
8.2	Previous modelling efforts	116
8.3	Model of PI and small G protein interactions	117
8.3.1	Definitions	118
8.3.2	Model assumptions	118
8.3.3	Description of the model	118
8.4	Parameter values	121
8.5	Simulations	123
8.6	Results	123
8.6.1	PIs and Rho proteins establish stable asymmetric spatial profiles in re- sponse to a graded stimulus	123

8.6.2	Activation of Cdc42, not Rac, by PIP ₃ required for proper asymmetric spatial profiles	126
8.6.3	Activation of PI5K or PI3K by Rac leads to asymmetric spatial profiles of PIs and Rho proteins	128
8.6.4	Asymmetric spatial profiles of PIs and Rho proteins can be reversed in response to a second stimulus	130
8.6.5	Cdc42 excludes PTEN by inhibiting activation of Rho	130
8.6.6	PIs and Rho proteins accumulate on one side of the cell in response to two chemoattractant sources	132
8.6.7	PIs prevent the formation of multiple Cdc42 domains in response to a random stimulus	134
8.6.8	PTEN activation by Rho not necessary to properly sense gradients	136
8.7	Summary of results and comparison to previous modelling efforts	138
8.8	Discussion	139
9	Phosphoinositides and Rho proteins regulate actin polymerization	141
9.1	Biological background	141
9.1.1	PIP ₂ inhibits capping of barbed ends	142
9.1.2	PIP ₂ enhances activation of Arp2/3	142
9.1.3	<i>De novo</i> actin polymerization is required for maintenance of the PI asymmetry	142
9.2	Experimental observations and questions to address	143
9.3	Model of PIs, Rho proteins and actin dynamics	144
9.3.1	Model Assumptions	144
9.3.2	Model equations	145
9.4	Results	146
9.4.1	1D cell model initiates and maintains directed movement in response to spatial gradients of PI3K and PTEN	146
9.4.2	Weak stimulus or short time exposure to stimulus causes delay in initiation of motion	149
9.4.3	Polymerization-dependent Rac activation of PI5K and PI3K causes loss of PI asymmetry but not Rho protein asymmetry	150

9.5 Discussion	154
10 Results and discussion	155
10.1 Model of actin dynamics	155
10.2 Model of Rho proteins and actin dynamics	155
10.3 Model of PIs and Rho proteins	156
10.4 Model of PIs, Rho proteins and actin dynamics	156
10.5 Discussion of general questions posed in Chapter 2	157
10.6 Experimentally testable predictions	159
10.7 Main results	161
10.8 Model limitations	162
10.9 Future work	163
Bibliography	165
A C code for simulating Equations (4.1)	180
B Estimate of conversion factor l	183

List of Tables

2.1	Typical biochemical rates involved in actin dynamics.	32
4.1	Definitions of model parameters and typical values based on biological literature.	53
6.1	Parameter estimates relevant to the Rho-proteins and their interactions.	90
7.1	Parameter estimates relevant to actin dynamics when coupled with a model of Rho proteins.	104
8.1	Parameter estimates relevant to phosphoinositide dynamics.	123

List of Figures

1.1	Image of a migrating fibroblast.	2
1.2	Image of a migrating neutrophil.	3
1.3	Image of a neural growth cone.	4
1.4	Electron micrograph of a migrating keratocyte, showing details of the actin meshwork in the lamellipodium	12
1.5	Some of the signalling cascades activated by an external signal that regulate actin polymerization in motile cells	13
1.6	A simplified signalling cascade investigated in this thesis.	14
1.7	Schematic of simplified signalling cascade considered in this thesis.	14
1.8	Geometry of the model	16
1.9	Flow chart of the thesis, indicating connections between the different chapters.	17
1.10	Schematic of interactions investigated in Chapters 3 - 5.	18
1.11	Schematic of interactions investigated in Chapter 6	18
1.12	Schematic of interactions investigated in Chapter 7	19
1.13	Schematic of interactions investigated in Chapter 8	20
1.14	Schematic of interactions investigated in Chapter 9	21
2.1	Schematic of actin filament polymerization.	23
3.1	Schematic diagram of the one dimensional domain to determine the flux of barbed ends and Arp2/3.	39
3.2	Comparison of analytic and simulation results	45
4.1	Schematic of first attempt at a computational algorithm	49
4.2	Schematic of second attempt at a computational algorithm	50
4.3	Schematic of successful final computational algorithm	51

4.4 Travelling wave solutions in the spontaneous nucleation, tip, and side branching cases	56
4.5 Plot of experimental data	59
4.6 Model predictions of spatial profiles of barbed ends compared to experimental data	60
4.7 Model predictions of filament density profiles fit to experimental data	61
4.8 Membrane speed increases as nucleation and Arp2/3 diffusion rates increase . . .	63
4.9 Membrane speed decreases as capping, depolymerization and membrane resistance rates increase	65
5.1 Comparison of spatial profiles in the presence of retrograde flow in the spontaneous branching case.	73
5.2 Comparison of spatial profiles in the presence of retrograde flow in the side branching case	74
5.3 Effect of retrograde flow speed on calculated membrane speed	75
6.1 General signalling cascade of the Rho-proteins Rho, Rac and Cdc42.	78
6.2 Schematic diagram of Rho protein localization and activation cycle, mediated by GEFs, GAPs and GDIs.	80
6.3 Experimentally proposed interactions of Rho/Rac/Cdc42.	83
6.4 Proposed Rho protein crosstalk as presented in Giniger (2002)	85
6.5 Schematic of Rho protein interactions used in Chapter 6	85
6.6 "Effective" Rho protein concentration combines concentrations in both membrane and cytoplasm.	86
6.7 Active Cdc42, Rac and Rho establish stable asymmetric spatial profiles in response to graded activation of Cdc42	92
6.8 Active Cdc42, Rac and Rho establish stable asymmetric spatial profile in response to a random activation of Cdc42	94
6.9 Active Cdc42, Rac and Rho establish two stable spatial domains in response to two stimuli	96
7.1 Schematic diagram of Rho protein signalling to the actin cytoskeleton	98
7.2 Barbed ends, Arp2/3 and filament density are elevated near the leading edge in response to graded activation of Cdc42	106

7.3	Membrane speed and change in barbed end profile in response to a gradient in the Cdc42 activation rate	107
7.4	Barbed ends, Arp2/3 and filament density are elevated in several distinct domains in response to random activation of Cdc42	109
8.1	Schematic of all possible phosphoinositides and interconversion between different forms	112
8.2	Simplified schematic of the phosphoinositides, showing lipids, kinases and phosphatase included in the model	112
8.3	Schematic diagram of proposed interactions between the phosphoinositides PI, PIP, PIP ₂ and PIP ₃ and the small G proteins Cdc42, Rac and Rho.	117
8.4	Schematic diagram of interactions shown in Figure 8.3 using the notation of Equations (8.3).	120
8.5	Spatial profiles of phosphoinositides and Rho proteins in response to a graded transient stimulus	125
8.6	Spatial profiles of phosphoinositides and Rho proteins in response to a graded transient stimulus when PIP ₃ enhances only Cdc42 or Rac activation	127
8.7	Rac-enhanced activity of PI5K or PI3K is required for maintenance of polarity but only Rac-enhanced activity of PI5K is required for persistent directed movement.	129
8.8	PTEN activity and active Cdc42 concentration before and stimulus in the full model and without inhibition of Rho by Cdc42	131
8.9	Spatial distribution of Cdc42 before, during and after the application of two stimuli on opposite sides of the cell	133
8.10	PIs prevent establishment of multiple domains of high Cdc42 in response to a random stimulus	135
8.11	PIs and Rho proteins establish and maintain asymmetric spatial gradients when PTEN activity is constant everywhere in the cell	137
9.1	Schematic diagram of proposed interactions between the phosphoinositides PI, PIP, PIP ₂ and PIP ₃ , the Rho proteins Cdc42, Rac and Rho and actin dynamics.	144
9.2	Change in membrane speed and barbed end profile in response to a transient stimulus.	147

9.3	Spatial profiles of PIs, Rho proteins and barbed ends, Arp2/3 and filament density in response to a transient stimulus corresponding to intracellular translocation of PI3K and PTEN	148
9.4	Initiation of movement and membrane speed resulting from different stimulus application time lengths	149
9.5	Spatial asymmetries in PIs and directed motion are not established in latrunculin treated cells if PI5K and PI3K activation relies on actin polymerization	153
10.1	Updated schematic of interactions between PIs, Rho proteins and actin dynamics.	160
10.2	Simulations of Rho protein and actin dynamics in a 2D model cell, reprinted with permission from Marée et al. (2006)	163

Acknowledgements

My work is not a solitary effort and would not exist without the help and support of many individuals. Thank you to everyone at UBC for taking a chance on me and allowing me to pursue graduate studies. Thank you to the Department of Mathematics and the Institute of Applied Mathematics for great facilities but, above all, wonderful colleagues and a very supportive work environment. Thank you to the students and faculty of the Math Bio group, past and present. It has been a pleasure to work with all of you. Thank you to my collaborators, Eric Cytrynbaum, Sasha Jilkin, Bard Ermentrout and Stan Marée, for their contributions to my thesis. I am indebted to Leah Keshet for her patience, persistence and enthusiasm as my research supervisor. I am honoured to be her student. Thank you to my funding sources, NSERC, MITACS and NSF (grant DMS-0240770 to Anders Carlsson, Washington University, St Louis), whose financial support made graduate studies feasible. Thank you to Leo for his incomparable personal and technical support. Thank you to mom and dad for their unwavering belief in me. Finally, thank you to all my friends and family for their love, support and encouragement. I owe a debt of gratitude to everyone who made this work possible.....

Co-authorship statement

The model of actin dynamics discussed in Chapters 3-5 arose out of discussions with Leah Edelstein-Keshet (UBC), Bard Ermentrout (U Pittsburgh) and Eric Cytrynbaum (UBC). In collaboration with Leah Edelstein-Keshet, I refined the model to its eventual form presented here, and examined the literature to estimate parameter values.

The Rho protein model discussed in Chapter 6 was developed primarily by Alexandra Jilkiné (UBC) and Leah Edelstein-Keshet and expanded by Stan Marée (U of Utrecht). I produced all figures in Chapter 6 based on parameter values compiled by Alexandra Jilkiné and Stan Marée.

I developed the phosphoinositide model proposed in Chapter 8, in conjunction with Leah Edelstein-Keshet. I derived parameter values based on experimental evidence.

All simulations in this thesis were performed using C code written by me. I produced all plots of simulation results in this thesis using Grace (plasma-gate.weizmann.ac.il/Grace). I created all schematics (not from other sources) with XFig (www.xfig.org). The thesis was typeset using L^AT_EX 2_ε (www.latex-project.org). All the writing, simulations and data plots in this thesis are my own work and I am entirely responsible for any errors and inaccuracies.

Chapter 1

Introduction and motivation

1.1 Introduction

If cells did not have the ability to move, organisms from amoebae to vertebrates would not be able to survive. Motile cells that respond to external stimuli are required for many fundamental physiological processes. Fibroblasts crawl to the site of a wound or tissue injury and provide a scaffold upon which healthy tissue can grow. Neutrophils migrate in response to an infection and kill invading bacteria. Cells must correctly interpret and respond to chemical signals for proper neural and embryonic development. Cell motility is also implicated in pathological processes. Metastatic cancer cells migrate to distant parts of the body where they proliferate and cause damage. Pathogens such as *Listeria* and *E coli* hijack many of the proteins used for cell motility to ensure their own survival and propagation.

Actin is a common protein found in virtually all eukaryotic cells. Most motile cells rely on polymerization of actin to generate sufficient force for membrane protrusion and movement. Actin polymerizes into thin filaments that cross link to form part of a cell's internal scaffolding, called the cytoskeleton.

Actin filaments are continually adding and losing individual actin monomers. The dynamic nature of the cytoskeleton allows cells to respond swiftly to external stimuli. Stimuli can cause internal changes in cells that manifest as asymmetric protein distributions and cytoskeletal rearrangement, which in turn leads to directed cell movement.

The aim of this thesis is to develop and explore models of actin polymerization and its regulation by upstream effectors. Many signalling cascades are activated by external signals but not all of these cascades lead to directed movement. By investigating and assimilating experimental results, I identify major modules containing families of signalling molecules that are involved in the cascade that leads to directed movement. The goal is to develop a better understanding of how these various signalling molecules conspire to give rise to directed cell movement and how those interactions lead to characteristic behaviours of both normal and

mutant cells.

1.2 Cell types studied

Many cell types have the ability to move in response to a stimulus. The following are some of the most common cell types used in experiments to explore the regulation of actin polymerization during cell movement.

1.2.1 Fibroblasts and neutrophils

Fibroblasts and neutrophils move by extending long thin processes called filopodia, followed by the extension of a lamellipodium, a thin membrane sheet which is hundreds of nanometers thick and tens of microns wide. Filopodia and lamellipodia are discussed further in Chapter 2. The extension of filopodia and lamellipodia cause large cell membrane deformations and leads to an overall cell shape change from a rounded cell, when stationary, to a tear-drop shape with a long, flat lamellipodium at the leading edge, when moving. A migrating fibroblast is shown in Figure 1.1 while a migrating neutrophil is shown in Figure 1.2. The membrane at the leading edge of a fibroblast or neutrophil is constantly reshaping as filopodia and lamellipodia extend and retract. Movement of fibroblasts tends to be slow (approximately $0.02 \mu\text{m/s}$, Nobes and Hall (1995)) while neutrophils move more rapidly (around $0.3 \mu\text{m/s}$, Iijima and Devreotes (2002)).

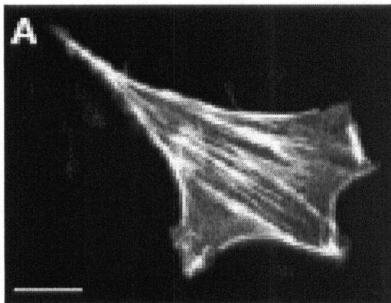


Figure 1.1: Image of a migrating fibroblast. Reprinted with permission from JM Vasiliev: Cytoskeletal mechanisms responsible for invasive migration of neoplastic cells. *International Journal Of Developmental Biology* 48(5-6):425-439 (2004).

1.2.2 Neural growth cones

During development, neurons also display a form of motility. The axon, which relays electrical signals to target cells, must migrate to appropriate target cells during formation of the nervous system. While the cell body itself does not move, an actin rich process called the growth cone

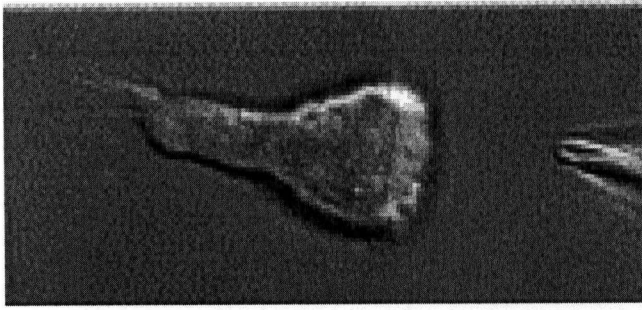


Figure 1.2: Image of a migrating neutrophil. Reprinted from *Current Opinion In Cell Biology* 16(1), CA Parent, Making all the right moves: chemotaxis in neutrophils and Dictyostelium, 4-13 (2004), with permission from Elsevier.

migrates along a chemical gradient, extending the axon (Kalil and Dent, 2005), as shown in Figure 1.3. Many of the same proteins that regulate motile cells are required for proper growth cone movement. Hence, growth cones are also studied as a model system for cell motility (Giniger, 2002; Gungabissoon and Bamberg, 2003).

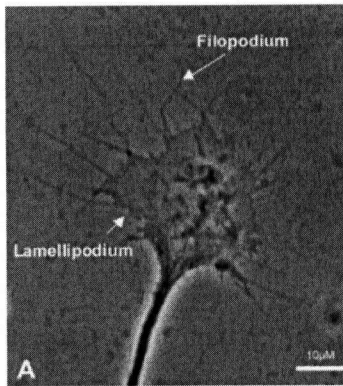


Figure 1.3: Image of a neural growth cone. Reproduced, with permission, from RA Gungabissoon and JR Bamberg: Regulation of growth cone actin dynamics by ADF/cofilin. *Journal of Histochemistry & Cytochemistry* 51(4):411-420, 2003.

1.2.3 Keratocytes

In contrast to fibroblasts and neutrophils, keratocytes (fish epithelial cells that rapidly repair wounds) maintain a consistent shape during movement. Typically, motile keratocytes take on a crescent shape with a long flat lamellipodium leading the way and a large bulge containing the nucleus at the rear of the cell. The shape of a keratocyte has been compared to a fried egg or a taco, as shown in Figure 1.4. Keratocytes do not extend filopodia during motility and do not exhibit large membrane deformations. Keratocytes move swiftly, at approximately $0.3\text{-}0.5 \mu\text{m/s}$ (Pollard and Borisy, 2003; Svitkina et al., 1997).

Unfortunately, it is difficult to produce mutant keratocyte cells to explore the role of various proteins in cell motility so there is little data available specifically for keratocytes. However, theoretical models of cell motility often use keratocytes as a model system (Grimm et al., 2003; Marée et al., 2006; Mogilner and Edelstein-Keshet, 2002) for the following reasons. Keratocytes have smooth, gliding motion at constant speed, with only minor shape deformation. Their adhesion to the substrate is relatively uniform, and hence plays a secondary role in motility compared to forward protrusion. Keratocytes have prototypical behaviours that form a basic repertoire upon which more elaborate behaviours are superimposed. Many other cell types with more complex dynamics have mutant forms that display such phenotypical behaviours, such as the epithelial cell line NBT-II, which can display keratocyte-like movement under certain conditions (Huang et al., 2003a). Thus, keratocytes present a good model system as a starting point for exploring directed movement.

In all the cell types discussed here, actin polymerization dynamics are regulated by a variety of signalling proteins and membrane bound lipids. A common feature of many motile cells is the asymmetric distribution of signalling molecules that is set up in response to an external signal. This leads to greater actin polymerization in one area of the cell, which then leads to membrane protrusion and cell migration. Although the models developed in this thesis explore keratocyte motility, data about the signalling pathways in keratocytes is lacking. Hence, I exploit the similarities in actin polymerization regulation by the cells described here by relying on results from different cell types to motivate and justify the models proposed in this thesis.

1.3 Experimental techniques to study cell motility

Motile cells are imaged and manipulated by experimentalists in an effort to understand how motile cells initiate and maintain directed movement. Below I briefly discuss some of the major experimental techniques used to produce the data referred to in this thesis.

1.3.1 Electron microscopy and gold particle tagging

Viewing cells using electron microscopy (EM) allows experimentalists to visualize details of fixed cells at extremely high resolution, on the order of tens of nanometers (Egelman, 1985). EM uses a beam of electrons instead of visible light to examine a sample, giving a magnification of approximately 500,000 \times . This imaging process provides information about the shape and structure of a sample and in motile cells, it is possible to visualize individual actin filaments in a lamellipodium (an electron micrograph of a keratocyte lamellipodium is shown in Figure 1.4).

To prepare a cell for EM imaging, the cell is fixed, halting all biochemical activity. The cell is then processed. Exposing the cell to a detergent removes the cell membrane, exposing the actin cytoskeleton in the lamellipodium. Once the cell is prepared, the actin meshwork can be directly imaged by an electron microscope. Experiments comparing EM images with details of the actin meshwork visible in live cells using phase contrast microscopy confirmed that the fixation process does not distort the actin meshwork and the angular structure of the actin meshwork is preserved during fixation (Verkhovsky et al., 2003).

It must be remembered that EM images are a static picture of a highly dynamic structure, in this case the lamellipodium, that do not capture temporal changes. This point was eloquently expressed by Dr. Lionel Harrison (Harrison (1993), p. 30):

The electron micrograph is like a mariner's chart or a map in an atlas. A famous story among opera lovers is that the conductor Franz Lachner, while rehearsing Wagner's *The Flying Dutchman* in 1864, complained about "the wind that blows out at you wherever you open the score." Anyone can feel this wind on hearing the remarkably evocative music played. Only a fully trained musician can feel it when looking silently at the printed score. When one contemplates an electron micrograph, and then a diagram of chemical changes in biochemical cycles, one should feel first the storm which raises the question and then the great determined flows through it which shape the organism.

EM can also be used in conjunction with other experimental techniques to reveal additional information about the actin meshwork in a lamellipodium. During cell processing, antibodies attached to gold particles can be used to tag specific proteins in the cell. The gold particles visible in an EM image are counted to give an approximate count of a certain protein in an imaged area. This technique was used in Bailly et al. (1999) to determine the number of free filament tips and branch points in the lamellipodium of a motile cell, compared to my model predictions in Chapter 4.

1.3.2 Fluorescence imaging

A popular technique that can be used with both live and fixed cells relies on fluorescent markers to indicate the spatial localization of specific proteins. When used with live cells, this allows experimentalists to observe dynamic changes in both the spatial localization and the relative increase or decrease of specific proteins. Proteins attached to fluorescent tags can be introduced into cells by permeabilization (where the cell membrane is slightly degraded to allow the passage of the large fluorescent molecules attached to the proteins of interest), by microinjection (where the tagged proteins are directly inserted into the cell) or using mutant cells (cells that express a fluorescent tag along with the protein of interest). Detectors collect the light emitted by the fluorescent proteins when excited, giving snapshots of protein localization and density at a series of time points.

Fluorescence microscopy, at much lower resolution than electron microscopy, can resolve features no closer together than 200nm (Stark et al., 2003). Fluorescence microscopy does not give an indication of the absolute quantity of a particular protein (unlike gold tagged proteins

in EM discussed above), but does provide a relative measure that can be used to determine the relative increase or decrease of a particular protein.

In this thesis, I use fluorescence data to determine the time course of the increase or decrease of particular molecules (Chapter 8, data taken from Huang et al. (2003b); Insall and Weiner (2001)) as well as the spatial profile of particular proteins in a moving cell (Chapter 4, data taken from Bailly et al. (1999); Redmond and Zigmond (1993); Svitkina and Borisy (1999)).

1.3.3 Regulation of protein expression

The techniques described above, electron and fluorescence microscopy, are useful for imaging the localization and dynamics of specific proteins, but not to examine the effect of individual proteins on cell motility. Fortunately, there are experimental techniques that allow an experimenter to adjust (up or down regulate) the expression of a particular protein, or modify its behaviour.

RNA interference (RNAi) is an experimental protocol used to block translation of specific RNA sequences into a protein. Double stranded RNA (dsRNA), containing the sequence for the target protein to be downregulated, is introduced into a cell. This causes the degradation of all RNA with the target sequence before they can be translated into proteins. In Chapter 8, I use data from RNA interference experiments in the construction of a model.

Experimentalists use mutant cells to observe the effect of different proteins in cell motility. To produce a mutant cell, the DNA sequence corresponding to a certain protein is altered so that the target protein created in this cell does not behave like the normally expressed protein. Target proteins in mutant cells can either have no effect on downstream effectors (constitutively inactive) or a stronger effect than usual (constitutively active). Data from mutant cells that express constitutively active or inactive proteins is used in Chapter 6.

To understand the role of certain proteins in cell motility, mutant cells or RNAi treated cells are exposed to a chemoattractant and the resulting behaviour is observed and compared to unaltered motile cells. Comparing observations of mutant and normal cells provides clues about which proteins are crucial for directed migration and what role those proteins play.

1.4 Structure of a motile cell

Figure 1.4 is an electron micrograph of a keratocyte, a scale of the fish Black tetra, at various levels of magnification, showing the organization of the actin cytoskeleton in the lamellipodium.

The cell is oriented so that the direction of motion is toward the top of the page in all images. Here I discuss features of the actin meshwork that are visible at each level of magnification.

1.4.1 Size scale of tens of microns

At the lowest magnification, Figure 1.4 (a), the entire cell is visible. A keratocyte is several tens of microns across its largest diameter. In Figure 1.4 (a), the lamellipodium is the thin sheet-like structure extended in the direction of motion (toward the top of the page), with width $\sim 10 \mu\text{m}$. Keratocyte lamellipodia are approximately 200 nm thick (Abraham et al., 1999). The lighter area in this figure is the cell body, containing the nucleus, organelles and other cell components (several microns thick, Laurent et al. (2005)). Unlike other motile cells, the leading edge of the keratocyte lamellipodium is smooth, with no visible filopodia.

1.4.2 Size scale of ten microns

At the next level of magnification, Figure 1.4 (b), the overall structure of the actin cytoskeleton in the lamellipodium is more apparent. Most filaments are oriented in the direction of motion and are interconnected to form a dense meshwork. The meshwork shown here extends approximately $9 \mu\text{m}$ into the cell. The scale bar shown in the image represents $1 \mu\text{m}$.

1.4.3 Size scale of one micron

As the magnification is increased further (Figure 1.4 (c) and (d)), individual actin filaments can be distinguished. Near the leading edge, (c), many barbed ends are visible and there is little distance between branch points. Farther from the leading edge, (d), barbed ends are less apparent and there is greater distance between branch points along a single filament.

1.4.4 Size scale of 0.1 microns

Figure 1.4 (e)-(h) show details of the actin meshwork at high magnification. In these images, it is possible to identify single filaments and their branches. These images show the branch points nucleated by the Actin Related Protein, Arp2/3 (Arp2/3 associates with actin filaments, forming a new filament oriented at 70° to the parent filament). Arp2/3, and its role in actin polymerization, is discussed further in Chapters 2 and 3. At this magnification, it is also possible to see how filaments weave together as they grow, giving rise to a crosslinked network that can resist deformation under the applied load force during cell motility.

1.5 Cell repertoire of interest

Motile cells exposed to an external stimulus go through a series of steps to initiate directed motion. Here, I outline this repertoire and indicate which aspects of cell motility I will be modelling in this thesis.

1.5.1 Gradient detection

In order to migrate toward a source of chemoattractant, motile cells must be able to detect a gradient as shallow as 1-2% across the diameter of the cell (Servant et al., 2000). A gradient of chemoattractant can be established by molecules diffusing from a micropipette (Wang et al., 2002; Weiner et al., 1999), or by experimental methods that construct a stable spatial gradient (Fisher et al., 1989). In normal motile cells, the direction of the gradient determines the eventual direction of cell movement. Motile cells remain sensitive to chemoattractant gradients and are able to turn and follow a new gradient if the micropipette is moved (Iijima et al., 2002; Xu et al., 2003). A gradient of chemoattractant is not always necessary for directed movement as some cell types appear to initiate directed movement in the absence of spatial cues (Wedlich-Soldner and Li, 2003). In this thesis, I explore how detection of an external gradient can lead to directed movement (Chapters 7 and 9).

1.5.2 Polarization

Once a cell has detected an external signal, the cell polarizes, establishing a distinct front and back. This results from internal responses that differ along the length of the cell, causing various proteins to accumulate and different biochemical processes to occur at the front and back of the cell (Iijima et al., 2002; Ridley et al., 2003). The direction of polarization determines the eventual direction of movement. A more detailed description, and qualitative modelling will be an important focus in Chapters 3, 6 and 8. Using mathematical modelling, I simulate cell polarization and investigate how a cell can establish and maintain a distinct front and back in response to an external signal (Chapters 8 and 9).

1.5.3 Amplification and adaptation

In a polarized cell, various proteins and lipids establish internal gradients (Merlot and Firtel, 2003; Weiner et al., 2002). The macroscopic internal gradients observed in polarized cells have a similar magnitude in response to both weak and strong external signals (Levchenko and Iglesias,

2002; Wang et al., 2002). Internal amplification of shallow external gradients allows a motile cell to respond consistently to signals of differing strengths. In contrast to internal amplification to an external gradient, cells exposed to a uniform increase in chemoattractant display a transient increase in certain molecules. After approximately one minute, the cell adapts to the homogeneous stimulus and returns to its resting state (Janetopoulos et al., 2004). However, not all motile cells adapt to a uniform stimulus; some randomly choose a direction and initiate directed motion (Wedlich-Soldner and Li, 2003). In the models presented here, I am concerned with gradient amplification and I do not explore possible mechanisms for adaptation.

1.5.4 Cytoskeletal remodelling and cell shape changes

The events described above, gradient detection, polarization and amplification, culminate in reorganization of the actin cytoskeleton. This causes the cell to change its shape from a rounded resting cell, to a tear-drop, or crescent shaped cell, with a lamellipodium extended in the direction of motion. In this thesis, I implement the proposed models in a 1D cell transect in the direction of motion. I do not explore shape changes that occur as a result of cell polarization. However, in my joint paper (Marée et al., 2006), we develop and explore a model similar to the one I present in Chapter 8, implemented in 2D. In that paper, we specifically address how cell shape change and polarization can occur.

1.5.5 Directed movement

Reorganization of the actin cytoskeleton gives rise to the lamellipodium and to directed motion up the chemoattractant gradient (chemotaxis). Polarization of the cell gives rise to a front and back and a defined leading edge. The cell remains sensitive to changes in the external signal and readjusts its trajectory quickly when the chemoattractant source is moved (Xu et al., 2003). Initiation and persistence of directed motion in response to an external signal will be explored in Chapters 7 and 9.

1.6 Signalling cascade

Research in molecular biology has uncovered a huge number of molecules, interactions, and functions relevant to cell motility. Out of such work, pictures such as Figure 1.5 have emerged. These signalling diagrams represent the current state of the art in experimental biology. Different experimental groups working on different signalling molecules contribute their results to

enormous databases such as KEGG (Kyoto Encyclopedia of Genes and Genomes), from which Figure 1.5 was taken. This exhaustive information is then assembled like puzzle pieces, to form immensely complicated signalling pathways. Even with access to an enormous quantity of data, not all components involved in signalling to the actin cytoskeleton are included in Figure 1.5. Further, it is not at all clear which components are essential for cell motility, and which are not. It is also not possible to deduce from these signalling diagrams how these components interact with each other, both spatially and temporally, to produce typical behaviours of motile cells.

In the next phases of cell biology, it will be desirable to use the vast experimental literature investigating cell motility to make sense of the dynamic behaviour of the components in the signalling pathways, not just the effect of the presence or absence of different components. Identifying regulatory modules or "circuits", understanding their individual functions, how they interconnect, and what roles these play in cell behaviour will be important. My thesis addresses a limited part of this goal in the context of cell motility.

Based on a review of the literature, I focus on the following modules involved in cell motility: phosphoinositides (PIs), discussed in Chapter 8, Rho proteins, presented in Chapter 7, and actin polymerization dynamics are introduced in Chapter 3 and considered further in Chapters 7 and 9. PIs mediate detection of external signals and regulate Rho proteins and actin dynamics. Rho proteins act as biological switches and interact with the PIs in a positive feedback loop. This results in accumulation of PIs and Rho proteins at the leading edge (polarization), in response to an external signal. Actin dynamics are crucial for cell motility as polymerization of actin generates the mechanical force needed for directed movement. In Chapter 9, I demonstrate that spatial regulation of actin dynamics by PIs and Rho proteins gives rise to the characteristic macroscopic spatial profiles of actin filaments in motile cells, as well as typical aspects of behaviour described in Section 1.5.

Some members of PI, Rho protein and actin modules, indicated by a thick circle, are included in the signalling cascade shown in Figure 1.5. A simplified signalling cascade showing the modules investigated in this thesis is given in Figure 1.6 and a more detailed schematic showing some interactions and localization of the lipids and proteins in Figure 1.7. The specific components shown in Figure 1.7 are discussed in more detail in Chapter 2.

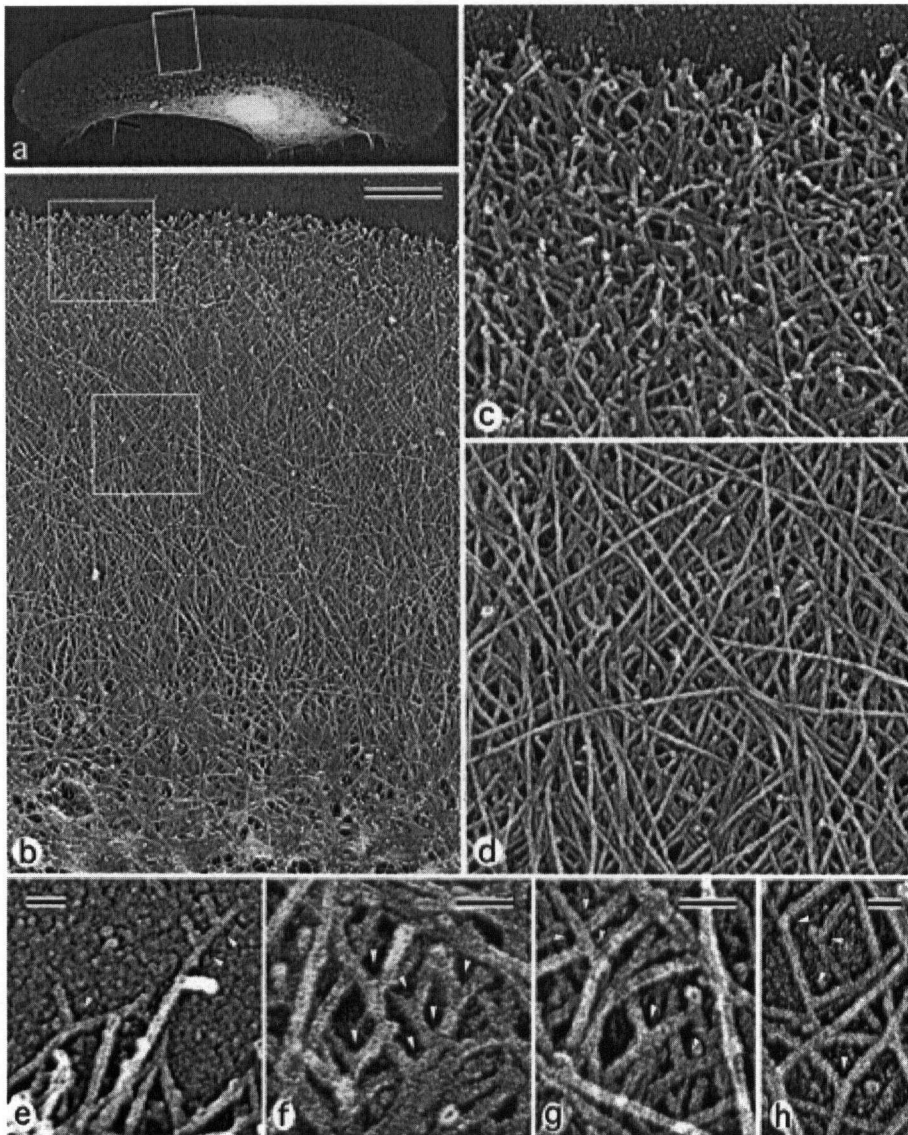


Figure 1.4: Electron micrograph of a migrating keratocyte with its typical crescent shape, showing details of the actin meshwork in the lamellipodium. The membrane is removed during the fixation process to reveal the actin meshwork. The whole cell, shown in (a), is moving toward the top of the page. The lamellipodium is the flat, broad structure extended in front of the cell. The cell body, containing the nucleus and other organelles, is thicker than the lamellipodium and appears brighter in this image. (b) shows more detail of the actin meshwork in the lamellipodium, enlarged from the box in (a). Filaments in the actin meshwork form a uniform angular mesh with a characteristic angle of 70° due to branching by the protein Arp2/3. The shape of the cell is preserved as it moves (not shown). The scale bar is $1 \mu\text{m}$. (c) and (d) are further enlargements of the actin meshwork from the two boxes in (b). At this magnification, individual filaments in the actin meshwork are visible. (e)-(h) show even further detail of actin filaments in the meshwork. Branch points are clearly visible and the intertwining of filaments is apparent. The scale bars in (e)-(h) indicate 50 nm . Reproduced from Svitkina et al. (1997), *Journal of Cell Biology*, 1997, 139, 397-415, by copyright permission of The Rockefeller University Press.

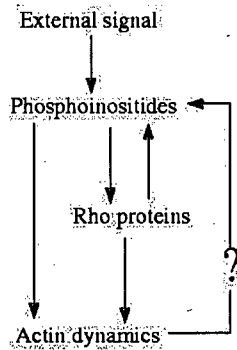


Figure 1.6: A simplified signalling cascade believed to regulate actin polymerization in motile cells and investigated in this thesis. Arrows indicate positive interactions.

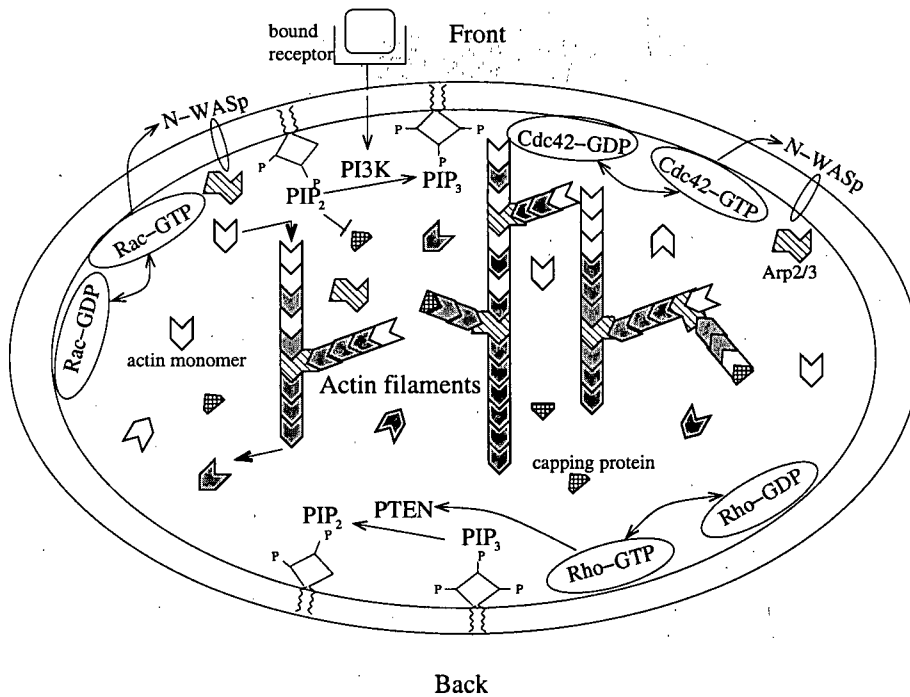


Figure 1.7: Schematic of simplified signalling cascade considered in this thesis.

1.7 Modelling cell movement in a 1D domain

In this thesis, I implement all models in a 1D domain, representing a 1D transect of a keratocyte lamellipodium, shown schematically in Figure 1.8. While this modelling approach cannot take into account all the features of a lamellipodium shown in Figure 1.4, I believe that this approach is able to capture the essential dynamics in a cell that lead to polarization and directed move-

ment. By taking a 1D transect, I am assuming that the actin meshwork in a large area in the middle of the lamellipodium is homogeneous and that the number of barbed ends growing into the transect is equivalent to the number growing out. While I do not keep track of individual actin filaments, new filaments nucleated by Arp2/3 in the transect at a 70° angle to the parent filament will be lost from the domain as the filament grows, but approximately the same number of new filaments will be gained as filaments nucleated outside the 1D transect grow into the domain. This allows the flux of filaments across the transect to remain close to zero. I am also assuming that the lamellipodium is not very thick so that the vertical thickness can be ignored. This has been verified experimentally, showing the thickness of the lamellipodium is approximately 200 nm, while the width and length of the lamellipodium is tens of microns (Abraham et al., 1999).

Investigating dynamics in a 1D domain has advantages over more complicated 2D or 3D implementations. A simple domain is important for proof of principle and provides more insight into underlying dynamics than more complicated domains. It is best to analyze complex signalling pathways in 1D to gain a thorough understanding of the underlying dynamics before extending the models to 2D. Current (Marée et al., 2006) and future work that investigates these models in a 2D setting arose out of a collaboration that relied on the model being initially developed and analyzed in 1D. This thesis describes those initial investigations, where the models are developed, parameters are estimated and the resulting behaviour is analyzed.

1.8 General questions addressed in this thesis

In order to gain a better understanding of cell motility, and motivated by a wealth of empirical observations of moving cells, I use mathematical modelling to investigate the following general questions:

1. How do we begin to understand pathways that signal to actin? (Chapters 2, 7, 9)
2. Is it possible to identify modules that are involved in cell motility? (Chapters 3, 6, 9)
3. How do these modules behave and how are they linked? (Chapters 4, 6, 7, 9)
4. How do biochemical rates affect the speed of a cell and the spatial distribution of actin filaments? (Chapters 4, 7, 9)

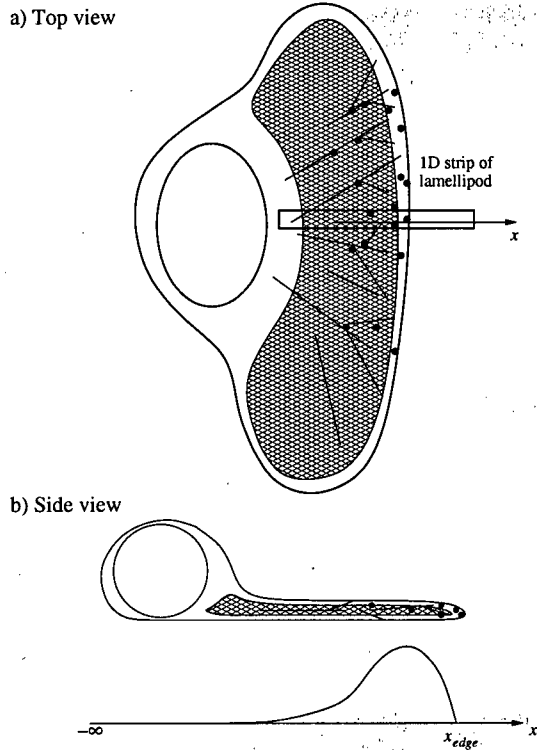


Figure 1.8: Geometry of the model. Shown is a schematic diagram of a moving keratocyte. (The arrow indicates the direction of filament growth and the direction of protrusion.). The boundary $+\infty$ is ahead of the cell, $-\infty$ is at the rear of the lamellipodium (a thin sheet-like structure that forms at the leading edge of the cell). a) is a top view of a keratocyte lamellipodium, showing the 1D transect used as the modelling domain in this thesis. b) is a side view, showing the relative thickness of the lamellipodium, as compared to the rest of the cell body. A typical distribution of actin filament density predicted by our model (and seen experimentally) is shown along the axis on the bottom. Figure courtesy of Leah Edelstein-Keshet.

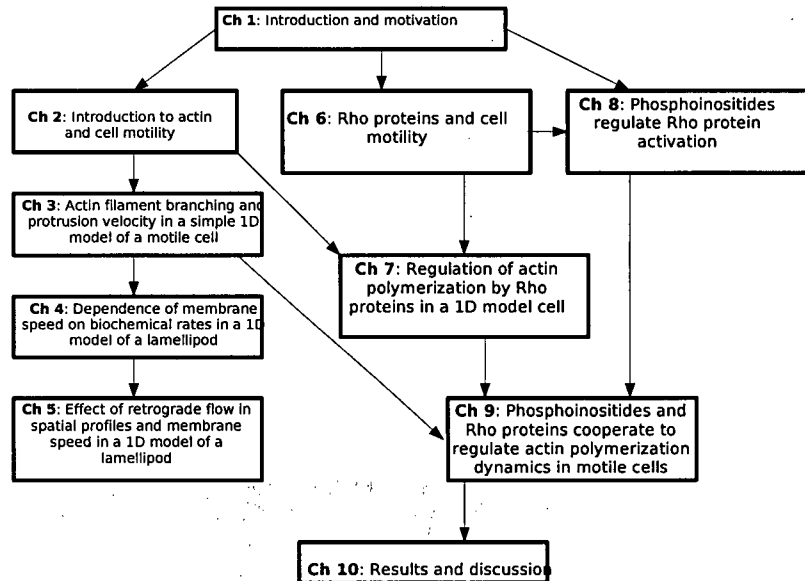


Figure 1.9: Flow chart of the thesis, indicating connections between the different chapters.

5. Which signalling cascades or direct or indirect feedback loops or interactions could lead to spatially stable actin profiles? (Chapters 7, 8, 9)
6. Which interactions within and between modules are crucial for cell motility? (Chapters 9, 10)

1.9 Structure of the thesis

In this thesis, I focus on regulation of actin polymerization and its role in initiating and maintaining directed motion. I do not take into account many mechanical aspects of cell motility such as cell adhesion to the substrate or contraction of the cell body. Each chapter in this thesis explores modules involved in actin dynamics in motile cells. Below is a short summary of each chapter and Figure 1.9 is a flow diagram indicating the relationship between the chapters.

Chapter 2: This chapter gives an in-depth introduction to actin and actin-related proteins, surveys current experimental research and poses general questions arising from experimental observations.

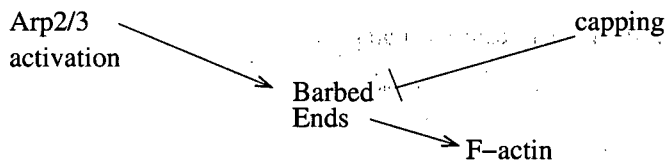


Figure 1.10: Schematic of interactions investigated in Chapters 3 - 5. To indicate a negative effect, the symbol \dashv is used, while a positive effect is indicated using \rightarrow .

Chapter 3: In this chapter, I develop a model of actin dynamics to investigate the distribution of actin filaments in a 1D lamellipodium. Under simplifying assumptions, it is possible to determine an analytic solution that demonstrates how cell speed and actin density are influenced by biochemical parameters. Chapters 3 - 5 formed the main subject of my paper Dawes et al. (2006).

Chapter 4: This chapter builds on the actin model developed in Chapter 3 and uses simulations to explore cases not easily solved using analytic techniques. I describe how parameter values are determined and I investigate the effect of these parameters on membrane speed. I compare experimental data with the spatial profiles produced by the model to determine which type of filament branching is most likely.

Chapter 5: In this chapter, I incorporate a small rearward flow of the actin meshwork, termed retrograde flow, into the actin model presented in Chapter 3. Retrograde flow of the actin meshwork has been observed in lamellipodia of motile cells and I wish to determine what effect, if any, this flow has on the membrane speed and spatial profile of actin as determined by my model.

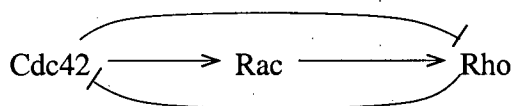


Figure 1.11: Schematic of interactions investigated in Chapter 6

Chapter 6: Rho proteins, shown schematically in Figure 1.11, form a module in my proposed simplified signalling cascade, Figure 1.6. In this chapter, I review a model of interactions between Rho proteins developed in Jilkin (2005) and Marée et al. (2006). These interactions lead to spatially asymmetric profiles in response to a graded signal.

Chapter 7: In this chapter, I present experimental evidence suggesting how Rho protein regulate actin

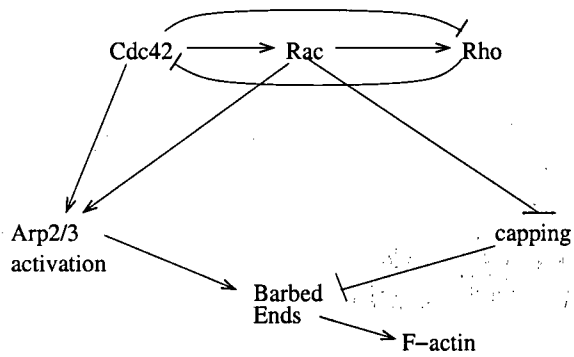


Figure 1.12: Schematic of interactions investigated in Chapter 7

polymerization dynamics. I modify and combine the models presented in Chapters 3 and 6 to simulate Rho protein regulation of actin dynamics in a 1D model of a lamellipodium. I find that combining these two modules leads to directed movement at biologically reasonable speeds in response to a graded stimulus, although some behaviours are not consistent with experimental observations. These aspects are corrected in following chapters.

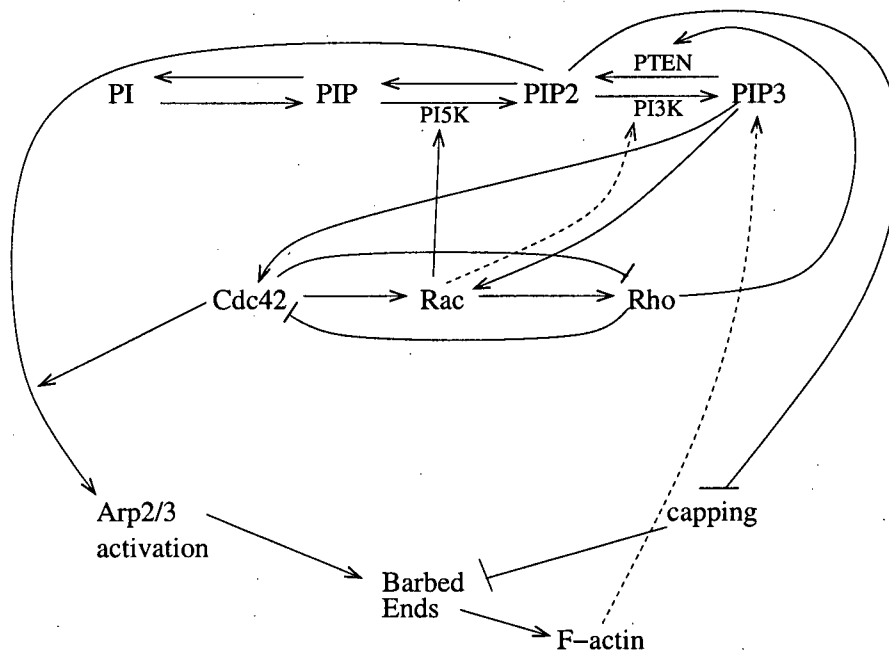


Figure 1.14: Schematic of interactions investigated in Chapter 9

Chapter 9: The final model proposed in this thesis combines the modules of actin dynamics (Chapter 3), Rho proteins (Chapter 6) and PIs (Chapter 8) into one whole system. I review evidence suggesting how PIs regulate actin dynamics and modify the models accordingly. I investigate initiation of movement in response to a graded stimulus and compare the resulting spatial profiles to experimental observations. I use this model to investigate the effect of actin polymerization on PIs and propose experiments to further elucidate the role of actin polymerization in the signalling cascade shown in Figure 1.5.

Chapter 10: In this Chapter, I summarize the results of my thesis and address the general questions posed in Chapter 2. Mathematical modelling can help to make sense of the interactions within and between modules and I discuss how this work expands our understanding of actin polymerization in motile cells. I suggest ways that the models proposed here can guide experiments, and eventually be refined and expanded.

Chapter 2

Introduction to actin and cell motility

The protein actin polymerizes to form long, thin filaments. These filaments crosslink to form a major part of a cell's cytoskeleton. The cytoskeleton provides an internal scaffold, determining a cell's shape and providing mechanical resistance to external forces. The cytoskeleton is a dynamic structure that undergoes continuous actin polymerization and can rapidly remodel itself in response to a stimulus. Motile cells respond to an external stimulus, such as a gradient of chemoattractant, by polarizing. This manifests as segregation of PIs and Rho proteins in specific areas of the cell. Among their other downstream effects, these molecules influence actin polymerization, causing enhanced actin polymerization in one area of the cell. The force generated by actin polymerization against the cell membrane is sufficient to propel the cell forward. The aim of this thesis is to develop mathematical models to better understand how actin polymerization is spatially regulated in a motile cell.

In this chapter, I discuss the protein actin and the role played by actin polymerization and its regulators in motile cells. In Chapter 3, I propose a model of actin dynamics in a motile cell based on the biological background presented here.

2.1 Actin

Actin, a small protein with molecular weight ~ 40 kDa, polymerizes from a monomeric form (G-actin) into long filaments (F-actin). G-actin binds to the nucleotide Adenosine Triphosphate (ATP) which hydrolyzes to Adenosine Diphosphate (ADP). Actin filaments are polar with different monomer association and dissociation kinetics at the so called "barbed" and "pointed" ends, shown schematically in Figure 2.1. ATP-bound actin monomers have faster barbed end binding kinetics than the ADP form. At a free barbed end of a filament, the newly assembled portion of F-actin is ATP-bound, forming an ATP-actin cap. Eventually the ATP is hydrolysed and older parts of a filament consist of ADP-actin, which are more prone to breakage and disas-

sembly. Overall, the rate of monomer addition is higher at the barbed end, and polymerization occurs more favourably there.

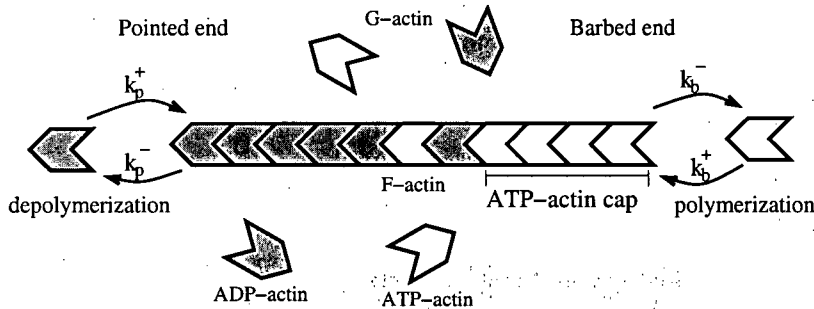


Figure 2.1: Schematic of actin filament polymerization. ATP-bound actin monomers are white while ADP-bound actin monomers are gray.

Actin binding proteins regulate the concentration of actin monomers available for polymerization. Sequestering proteins bind to actin monomers, preventing them from associating with filament barbed ends. Other proteins such as profilin, bind to actin monomers and catalyze the exchange of ADP for ATP, increasing the pool of monomers available for polymerization. I do not focus on the various bound forms of actin monomers in this thesis (see Mogilner and Edelstein-Keshet (2002) for a thorough treatment of the actin monomer cycle and its effect on filament growth at the leading edge of a motile cell).

2.1.1 Speed of actin polymerization

Actin monomers associate with both the barbed and pointed ends of a filament, but with different kinetics. *In vitro* experiments have determined the monomer association (k^+) and dissociation (k^-) rates for ATP-actin at both ends of a filament (k_b^\pm at the barbed end and k_p^\pm for the pointed end, shown schematically in Figure 2.1). At the barbed end, $k_b^+ = 11.6\mu\text{M}^{-1}\text{s}^{-1}$, $k_b^- = 1.4\text{s}^{-1}$, and at the pointed end, $k_p^+ = 1.3\mu\text{M}^{-1}\text{s}^{-1}$, $k_p^- = 0.8\text{s}^{-1}$ for ATP-actin (Bonder et al., 1983). A filament gains approximately $\delta = 2.7$ nm of length when a monomer is added. The typical concentration of ATP-actin monomers available for polymerization (ie. those monomers not sequestered or otherwise made unavailable for polymerization) in a cell is approximately $a = 20\mu\text{M}$ (Pollard et al., 2000). At this monomer concentration, there is a greater net gain of monomers at the barbed end than at the pointed end. This leads to filament "treadmilling" where a monomer added to the barbed end cycles through the filament and is eventually lost from the pointed end. It is possible to determine the speed at which a barbed end grows in a

motile cell as a result of actin polymerization:

$$\begin{aligned} v &= (\text{rate of monomer addition} - \text{rate of monomer loss})\text{length gained} \\ &= (k_b^+ a - k_b^-)\delta \end{aligned} \quad (2.1)$$

$$\approx 0.6\mu\text{m/s}. \quad (2.2)$$

for a monomer concentration of $a = 20\mu\text{M}$. For this estimate, I do not take into account polymerization at the pointed end since most filament pointed ends are capped by Arp2/3 and unavailable for polymerization. Continuous disassembly of the actin meshwork at the rear of the lamellipodium maintains the pool of actin monomers available for polymerization.

From these rate constants, it is possible to determine the critical concentration of ATP-actin (a_{crit}), the concentration of monomers below which polymerization will not occur (Pollard, 1986). If the rate of monomer dissociation (k^-) is greater than or equal to the rate of monomer addition (k^+), a filament cannot grow. At the pointed end, the critical concentration is

$$a_{crit}^p = \frac{k_p^-}{k_p^+} = \frac{0.8\text{s}^{-1}}{1.3\mu\text{M}^{-1}\text{s}^{-1}} \approx 0.6\mu\text{M}.$$

Similarly, the critical concentration at the barbed end is

$$a_{crit}^b = \frac{k_b^-}{k_b^+} = \frac{1.4\text{s}^{-1}}{11.6\mu\text{M}^{-1}\text{s}^{-1}} \approx 0.12\mu\text{M}.$$

Note the critical concentration at the barbed end is lower than at the pointed end due to different monomer binding kinetics. I do not explicitly keep track of actin monomers in the models presented here but instead assume that monomers are freely available and filament polymerization takes place at a constant rate everywhere in the cell. The rate of barbed end growth is an important parameter in the model of actin polymerization dynamics proposed in Chapter 3.

2.1.2 Force generation by actin polymerization

It has been proposed that actin filaments operate as Brownian ratchets that exert a forward force on the membrane when monomers are added (Oster, 2002). Peskin et al. (1993) hypothesized that actin filaments are rigid and thermal fluctuations in the membrane create a space between the filament tips and the membrane. When this gap is sufficiently large, a monomer can associate, lengthening the filament. The membrane can no longer diffuse back to its original

position. Many such monomer addition events compel the membrane to move forward. It was later proposed in Mogilner and Oster (2003, 1996) that the actin filaments are subject to greater thermal fluctuations than the membrane, creating a gap large enough for monomer addition. After monomer addition, the newly lengthened filament exerts force on the membrane as it straightens. By averaging over many barbed ends and assuming that each barbed end shares the load force of the membrane equally, Mogilner and Oster (1996) derived a force-velocity relation that specifies the velocity of the membrane due to the force exerted by polymerizing barbed ends, described briefly below.

Mogilner and Oster (1996) first consider the case of a single filament with fast thermal fluctuations compared to the rate of monomer addition. The velocity of the membrane, c , is then approximately given by:

$$c = \delta(k_b^+ a_0 e^{-\delta f/k_B T} - k_b^-), \quad (2.3)$$

where f is the load force of the membrane, a_0 is concentration of actin monomers at the membrane, k_B is the Boltzmann constant, T is temperature and k_b^\pm and δ have the same meaning as above. The load force f is a combination of two factors: membrane surface tension and binding energy dissipation as the membrane is pushed forward (Mogilner and Edelstein-Keshet, 2002). Membrane surface tension exerts an inward force since the membrane resists deforming in response to pushing filaments, due to stretch and compression of the membrane lipid bilayer. Binding energy dissipation occurs as links between the actin cytoskeleton and the membrane are severed as the membrane is pushed forward.

However, as shown in Section 2.1.1, the rate of monomer dissociation at the barbed end is small compared to the rate of addition, provided the concentration of actin monomers is sufficiently high. In typical motile cells, actin monomers are freely available, making monomer loss from barbed ends insignificant (filament length gained in one second is $\sim 0.63\mu\text{m}$ while length loss is $\sim 0.004\mu\text{m}$). The velocity of the membrane can then be written as:

$$c \approx \delta k_b^+ a_0 e^{-\delta f/k_B T}. \quad (2.4)$$

This equation can be understood as follows. The exponential term $e^{-\delta f/k_B T}$, is the probability that a gap of size δ forms, where $0 < e^{-\delta f/k_B T} < 1$. The factor determining this probability, $\frac{-\delta f}{k_B T}$, is a ratio of two energies. The numerator is the energy required to make a δ -sized gap,

and is analogous to the "activation energy" in physical chemistry since it is the minimum energy necessary for monomer addition. The denominator is the thermal energy, which uses Boltzmann's constant to determine kinetic energy at the temperature T .

To extend this relation to a large number of barbed ends pushing on the membrane, it is assumed that each barbed end shares the load force of the membrane equally, so that each barbed end feels a force $f = F/B_0$ where F is the membrane resistance force and B_0 is the number of barbed ends pushing on the membrane. This leads to the following expression for the force-velocity relation for many barbed ends pushing on the membrane:

$$c = v \exp\left(-\frac{F\delta}{k_B T B_0}\right) \quad (2.5)$$

where $v = \delta k_b^+ a_0$ is the free polymerization speed in the absence of the membrane. I use this Brownian ratchet force-velocity relation to determine the speed of membrane movement in the actin polymerization model developed in Chapter 3.

The idea of actin filaments operating as Brownian ratchets has been explored further in recent papers. Expanding on their earlier model, Mogilner and Oster (2003) separate actin filaments into two groups: attached filaments that are transiently bound to the membrane and exert a force opposite to the direction of motion, and working filaments that are actively pushing on the membrane. They use this model to investigate the motion of the pathogen *Listeria* and specially coated polystyrene beads. Dickinson and Purich (2002); Dickinson et al. (2004) suggest that proteins that track the tips of actin filaments are responsible for monomer addition, not thermal fluctuations. Future work includes exploring different mechanisms for membrane protrusion suggested by these theoretical investigations.

2.2 Actin Associated Proteins

Many proteins are involved in regulating actin polymerization dynamics in motile cells. Some directly influence actin polymerization and depolymerization while others provide structural stability or sequester actin monomers. The biochemical rates that result from the activity of these proteins are listed in Table 2.1. These are used extensively in the models developed in this thesis.

2.2.1 Capping Proteins

Capping proteins bind to barbed ends of actin filaments, preventing further polymerization activity. In the absence of capping protein, filaments grow unconstrained until the concentration of monomers falls below a_{crit} . Capping proteins (including gelsolin and CapZ in muscle cells) bind to barbed ends with a high affinity ($k_+ = 3\mu\text{M}^{-1}\text{s}^{-1}$) and unbind very slowly ($k_- = 5 \times 10^{-4}\text{s}^{-1}$); it takes over 1000 s for a barbed end to be uncapped (Feinberg et al., 1998; Pollard et al., 2000; Schafer et al., 1996). At the concentration of capping proteins found in cytoplasm, a free barbed end has a half life of about 0.25 s (Pollard et al., 2000). Regulation of capping in motile cells ensures that free barbed ends are polymerizing only in specific areas of the cell. I incorporate the activity of capping protein into the model for actin dynamics in Chapter 3.

2.2.2 Nucleating Proteins

Arp2/3, a seven subunit complex that associates with actin, has been identified as the key nucleator of new filaments. Arp2/3 mediates branching of actin filaments by binding to an existing filament and creating a new tip oriented at 70° to the parent filament (Cameron et al., 2001). It is not entirely clear if Arp2/3 binds to the tip (Falet et al., 2002; Pantaloni et al., 2000) or the side (Amann and Pollard, 2001; Fujiwara et al., 2002) of existing filaments. While it is not possible to directly observe the nucleation activity of Arp2/3, current theoretical and experimental analyses strongly suggest that side branching is the most likely mechanism (Carlsson et al., 2004; Dawes et al., 2006). I explore different branching mechanisms in Chapter 4 and provide further evidence that side branching by Arp2/3 is most likely. On average, branches nucleated by Arp2/3 appear $1.56\ \mu\text{m}$ from the barbed end of a parent filament with an average density of one branch every $4.4\ \mu\text{m}$ (Amann and Pollard, 2001).

Arp2/3 is required for cell motility and is responsible for the orthogonal meshwork of actin filaments observed in lamellipodia (thin actin-rich protrusions that are characteristic of many motile cells, Bailly et al. (2001)). Arp2/3 is distributed in the cytoplasm of unstimulated cells and accumulates at the leading edge of stimulated cells (Falet et al., 2002) where it interacts with the membrane-associated protein WASp (found mostly in hematopoietic cells Orange et al. (2004)) or N-WASp (found in many different cell types). WASp and N-WASp dramatically enhance the rate of Arp2/3 nucleation (Suetsugu et al., 2001). Once Arp2/3 nucleates a new

barbed end, it remains localized to the branch point in the actin mesh with the pointed end of the new filament attached to the parent filament (Cameron et al., 2001). I explicitly include the concentration of active Arp2/3 in the models for actin dynamics explored in Chapters 3, 7 and 9.

2.2.3 Filament Depolymerizing Proteins

Filament disassembly frees up actin monomers, making them available for polymerization elsewhere in the cell. Filament decay can occur by several means including depolymerization at the pointed end, severing, or degradation of older parts of an actin filament. While monomers do spontaneously dissociate from filaments, this process can be accelerated by actin depolymerizing factor (ADF)/cofilin (Bamburg, 1999), which severs filament portions that are ADP-bound. Observations of filament assembly and disassembly in motile cells shows that actin filaments turn over approximately every 30 s (Pollard et al., 2000). In the models discussed in Chapters 3, 7 and 9, I do not keep track of whether a filament is ATP or ADP bound and instead assume that all filaments have an average lifetime of 30 seconds.

2.2.4 Sequestering Proteins

Sequestering proteins vary the availability of monomers, enhancing or impeding the rate of filament growth. Proteins such as thymosin β 4 bind to G-actin, making the monomer unavailable for polymerization. Profilin binds to G-actin, enhancing polymerization by rapidly exchanging ADP for ATP (Dos Remedios et al., 2003). The actin monomer cycle and its influence on actin polymerization dynamics near the leading edge of a motile cell is not explicitly considered here (see Mogilner and Edelstein-Keshet (2002) for an investigation of sequestering proteins).

2.2.5 Time scales of actin dynamics

Actin dynamics have a variety of time scales, as discussed above. Bound capping protein has a half-life of 1000 s while a filament in a motile cell turns over approximately every 30 s. Since capping protein binds to filament tips away from the leading edge, this binding persistence ensures that filaments are disassembled and recycled back into the pool of available monomers without becoming uncapped and resuming polymerization. Capping protein also prevents depletion of the monomer pool, since filament growth is rapid compared to filament turn over. Without capping protein limiting the number of actively polymerizing barbed ends, the rate of filament

decay would be insufficient to replenish the monomer pool.

2.3 Signalling Molecules

Cytoskeletal remodelling in response to an external signal results from the spatial redistribution of signalling molecules that influence actin dynamics. Below I briefly describe specific signalling molecules that are known to regulate actin dynamics in motile cells. An integrated model that combines these signalling molecules with actin dynamics is investigated in Chapter 9.

2.3.1 Rho Proteins

The Rho proteins Cdc42, Rac and Rho, also called Rho GTPases, are known regulators of the actin cytoskeleton. Cdc42 leads to activation of Arp2/3 (via enhanced activation of N-WASp, Higgs and Pollard (2000)) while Rac inhibits the activity of capping protein (Arcaro, 1998). Although I do not include the downstream effects of the Rho protein Rho here, Rho inhibits depolymerization by inactivating ADF/cofilin (Gungabissoon and Bamberg, 2003) and enhances polymerization by increasing the activity of profilin (Da Silva et al., 2003). The Rho proteins act as molecular switches by cycling between an inactive GDP-bound (guanosine diphosphate, the nucleoside guanosine bound to two phosphates) state and an active GTP-bound (guanosine triphosphate, guanosine bound to three phosphates) state. There is crosstalk between the Rho proteins with experiments indicating that Cdc42 activates Rac which activates Rho and there is evidence for an antagonistic relationship between Cdc42 and Rho (Burrige, 1999; Giniger, 2002; Li et al., 2002), which I discuss in more detail in Chapter 6. Rho proteins form asymmetric spatial gradients when a motile cell is exposed to an external signal. I explore a model of Rho protein regulation of actin dynamics in Chapter 7.

2.3.2 Phosphoinositides

Phosphoinositides (PIs), membrane associated lipids, are required for cell motility as they mediate spatial sensing of external signals (Wang et al., 2002). PIs directly affect actin dynamics by inhibiting capping (DiNubile and Huang, 1997; Schäfer et al., 1996) and indirectly affect actin dynamics by influencing the activation state of Rho proteins (Aoki et al., 2005; Li et al., 2003; Welch et al., 2002). Rho proteins in turn affect the PIs (van Hennik et al., 2003; Welch et al., 2003). A model of PI and Rho protein interaction is explored in Chapter 8. Like the Rho proteins, PIs form spatial gradients in stimulated cells (Weiner et al., 2002).

PIs and Rho proteins act cooperatively to regulate actin polymerization, decreasing the rate of capping (Tolias et al., 2000) and increasing the rate of Arp2/3 nucleation (Higgs and Pollard, 2000). A schematic of the general signalling cascade believed to regulate actin polymerization in motile cells and the basis for the models developed in this thesis is shown in Figure 1.6. A model that combines PIs and Rho proteins with actin dynamics is explored in Chapter 9.

2.4 Stages of cell movement

A series of events must occur for a cell to move in response to an external signal. These events are regulated by signalling molecules that determine where in a cell the activity takes place.

2.4.1 Spatial asymmetries in signalling molecules

Phosphoinositides are the first signalling molecules to establish spatial gradients in response to an external signal (Merlot and Firtel, 2003; Wang et al., 2002; Weiner et al., 2002). After the establishment of a PI asymmetry, the Rho proteins establish spatial asymmetries with Cdc42 and Rac elevated at the front of the cell and Rho elevated at the rear (Kraynov et al., 2000; Nalbant et al., 2004; Srinivasan et al., 2003; Xu et al., 2003). It is not clear if the observed spatial asymmetries of PIs and Rho proteins are due to interactions between the Rho proteins and PIs or if PIs and Rho proteins maintain their own asymmetries in isolation.

2.4.2 Cytoskeletal rearrangement

The asymmetry of PIs and Rho proteins spatially regulate actin polymerization dynamics, leading to changes in cell shape. In particular, there is a massive generation of new barbed ends and enhanced actin polymerization in response to a stimulus at the leading edge of a motile cell.

Extension of filopodia

Cdc42 causes the formation of filopodia, long thin structures that protrude from the leading edge of the cell, generally in the direction of motion (Burrige, 1999; Matozaki et al., 2000; Ridley, 2001c; Takai et al., 2001). Filopodia consist of parallel bundles of actin filaments, that may form in areas of the cell where capping is inhibited (Mejillano et al., 2004). Filopodia are usually 0.2 to 0.4 μm in diameter (Jacinto and Wolpert, 2001), and 5 -35 μm long but can grow to 70 μm in length (Adams, 2001; Jacinto and Wolpert, 2001; Wood and Martin, 2002). They can extend and retract at approximately 10 $\mu\text{m}/\text{min}$ (Jacinto and Wolpert, 2001; Wood and

Martin, 2002). Filopodia are not necessary for gradient sensing or directed movement as some motile cells do not display these membrane instabilities.

Extension of lamellipodia

Actin polymerization drives the extension of lamellipodia (Adams, 2001), a broad but thin actin-rich protrusion. Lamellipodia vary greatly in size but can spread several μm across and extend many μm into a cell (Small et al., 2002). Arp2/3 is required for lamellipodium formation and causes the actin filaments to be organized into an orthogonal mesh with a characteristic branching angle of 70° (Cameron et al., 2001; Svitkina and Borisy, 1999). In the lamellipodium, approximately 80% of the actin filaments are oriented with their barbed ends toward the leading edge (Svitkina et al., 1997). Most filaments are oriented at an angle of $\pm 35^\circ$ to the membrane, making monomer addition more likely during thermal fluctuations than filaments that are oriented perpendicular to the membrane. Also, filaments oriented at $\pm 35^\circ$ are able to exert more force on the membrane than those filaments oriented away from the membrane (Maly and Borisy, 2001). I do not keep track of filament orientation in the models presented here but I assume that all filaments are oriented in the direction of motion, as discussed in Chapter 3. Please see Marée et al. (2006) for a model of actin dynamics that does consider filament directionality.

Retraction of the cell body

As the cell extends forward, adhesions keep the cell from slipping backward (Wehrle-Haller and Imhof, 2002). However, the cell can extend only so far before the connection between the rear of the cell and the substrate must be severed.

Rho enhances contraction of the cell body, allowing the rear of the cell to detach from the substrate (Burrige, 1999; Ridley, 2001b). In this thesis, I do not include cell body retraction, but several models have investigated the role of cell body adhesion and contraction in cell motility. Gracheva and Othmer (2004) developed a viscoelastic model of a motile cell to investigate the effect of contraction and adhesion on the speed of movement. Marée et al. (2006) proposed a 2D model of a motile cell that includes retraction of the cell body. Another model, presented in Bottino et al. (2002); Bottino and Fauci (1998), treats the actin meshwork in the lamellipodium as a lattice of interconnected springs.

For sustained cell movement, extension and retraction must be continuously and smoothly coordinated, suggesting that actin polymerization is tightly regulated in motile cells.

2.5 Observations of motile cells

The typical speed of cells that rely on actin polymerization for movement can vary widely. Amoebae and neutrophils (immune surveillance cells) have been observed moving at speeds around $0.3 \mu\text{m/s}$ (Iijima and Devreotes, 2002) (the speed of free actin polymerization, Section 2.1.1) while keratocytes (fish epithelial cells) move at approximately $0.3\text{-}0.5 \mu\text{m/s}$ (Pollard and Borisy, 2003; Svitkina et al., 1997). In contrast, fibroblasts (cells involved in wound healing) move more slowly at approximately $0.02 \mu\text{m/s}$ (Nobes and Hall, 1995). In this thesis, I focus on keratocytes as a model cell. In contrast to fibroblasts and other motile cell types, keratocytes display smooth, persistent motion at a roughly constant speed, have few membrane instabilities (such as extension and retraction of filopodia) and maintain a regular shape that varies little during motion, making keratocytes a good choice of cell for the purposes of modelling.

Parameter	Meaning	Value	Source
κ	rate of capping	1 sec^{-1}	[1]
γ	rate of depolymerization	$1/30 \text{ sec}^{-1}$	[2]
v	growth rate of uncapped barbed end	$0.1 \mu\text{m}/\text{sec}$	[3]
η	rate of nucleation by Arp2/3	$100 \mu\text{m}^{-1}\text{sec}^{-1}$	[1]

Table 2.1: Typical biochemical rates involved in actin dynamics. Cited sources: [1]: Pollard et al. (2000), [2]: Mogilner and Edelstein-Keshet (2002), [3]: Sanger et al. (1996).

Chapter 3

Actin filament branching and protrusion velocity in a simple 1D model of a motile cell¹

In the previous chapter, I presented experimentally determined information about actin and the regulation of actin polymerization in motile cells. In this chapter, I formulate and analyze a 1D model for the spatial distribution of actin density at the leading edge of a motile cell, assuming the cell is already polarized and in motion at a constant speed. The model incorporates nucleation, capping, growth and decay of actin filaments, and known parameter values based on the literature, as discussed in Chapter 2. As polymerization of actin is known to generate the force required for membrane protrusion, I develop this model to investigate under what conditions a polarized cell can maintain steady state motion and characteristic actin profiles. Using a simplified geometry, and reasonable assumptions about the biochemical processes, I derive PDEs for the density of actin filaments and their tips. This model of actin dynamics is the focus of this thesis. However, this model of actin dynamics cannot address cell polarization or initiation of motion so in later chapters, I use a variant of this model to investigate actin dynamics regulated by upstream effectors, such as Rho proteins (Chapter 7) and phosphoinositides (Chapter 9).

3.1 Regulation of actin polymerization in motile cells

Polymerization of actin in the lamellipodium is tightly regulated by many factors that cap, nucleate, and depolymerize the filaments (Small et al., 2002; Wood and Martin, 2002).

3.1.1 Role of filament capping and decay

Regulation of the number of actively polymerizing barbed ends by capping protein is necessary for efficient cell protrusion; otherwise the pool of available actin monomers would be quickly

¹A version of the material presented in Chapters 3-5 is in press. AT Dawes, GB Ermentrout, EN Cytrynbaum and L Edelstein-Keshet. Actin filament branching and protrusion velocity in a simple 1D model of a motile cell. *Journal of Theoretical Biology*, In Press, 2006.

depleted by a large number of polymerizing barbed ends. Filaments are disassembled by simple loss of monomers, by cutting, or by some combination thereof. Experiments suggest that depolymerization tends to occur more frequently away from the leading edge (Valloton et al., 2004), where filaments are more likely to be in the ADP-actin form. In the model presented here, I assume barbed end capping occurs at a constant rate, meaning that capping protein is plentiful everywhere in the cell. I also assume filament decay occurs at a constant rate regardless of the age or position of the filament in the cell.

3.1.2 Role of Arp2/3 nucleation

It is known that Arp2/3, essential for cell motility (Bailly et al., 2001), is responsible for the branched actin network seen in the lamellipodium (Suetsugu et al., 2002). It is not clear if Arp2/3 must remain bound to the membrane, or if it diffuses away from the membrane before binding to a filament and nucleating a new barbed end. Once activated by membrane bound proteins such as WASp or N-WASp, Arp2/3 can associate with an existing filament to nucleate a new barbed end at 70° to the parent filament (Amann and Pollard, 2001). Arp2/3 is incorporated into the filament during the nucleation process. I explicitly include Arp2/3 concentration in the model developed here so that new barbed ends are generated only in areas where active Arp2/3 is present.

3.1.3 Localization of Arp2/3 and barbed ends in motile cells

As discussed in Chapter 2, active polymerization in motile cells occurs almost exclusively at the leading edge (Bailly et al., 1999; Ponti et al., 2004; Redmond and Zigmond, 1993; Svitkina et al., 1997). Moreover, Arp2/3 is also incorporated into the actin meshwork near the leading edge (Bailly et al., 1999; Falet et al., 2002; Svitkina and Borisy, 1999). Electron micrographs of fixed cells that have gold particles attached to Arp2/3 and barbed ends, provide an absolute measure of the number of free tips and branch points in some small region near the leading edge. These measures are consistent with fluorescence experiments, showing most barbed ends within $0.5 \mu\text{m}$ of the leading edge and Arp2/3 incorporated into the meshwork over $2\text{-}3 \mu\text{m}$ near the leading edge (Bailly et al., 1999; Svitkina and Borisy, 1999). Experiments using both live and fixed imaging of motile cells have determined that approximately 80% of filaments up to $8 \mu\text{m}$ away from the leading edge are oriented with their barbed ends pointing toward the leading edge (Small et al., 1995; Svitkina et al., 1997; Verkhovsky et al., 2003). To simplify the model

of actin dynamics, I assume all barbed ends are oriented toward the leading edge.

3.2 Previous modelling efforts

A number of models have been proposed to investigate actin dynamics in motile cells. Some models focus primarily on the actin monomer cycle and actin polymerization at the leading edge (Grimm et al., 2003; Mogilner and Edelstein-Keshet, 2002). Using a 1D model, Mogilner and Edelstein-Keshet (2002) showed how membrane speed depends on barbed ends and ATP-actin monomer concentration at the leading edge of a cell. Grimm et al. (2003) made predictions regarding the shape of the leading edge. Both papers employed a force-velocity relationship as the basis for membrane protrusion, but neither is concerned with the profiles of actin density or the biochemistry of branching mediated by Arp2/3. Edelstein-Keshet and Ermentrout (2000) proposed a model to investigate actin length distribution in a 1D strip of the lamellipodium but the focus was on cutting and severing, rather than branching.

Carlsson (2001) used a stochastic 3D model to simulate the growth of an actin network against an obstacle. While this approach was able to qualitatively reproduce many of the features of the actin meshwork in lamellipodia, it was not possible to draw general conclusions regarding the branching mechanism of Arp2/3 based on these simulations. To investigate more fully whether Arp2/3 nucleates new filaments off the tip or side of existing filaments, Carlsson et al. (2004) combined *in vitro* experimental work with a model of actin dynamics in a well-mixed, spatially homogeneous setting. Comparison between the simulation and experimental data provided compelling evidence that side branching is the most likely mechanism.

The model of actin dynamics proposed in this chapter complements previous approaches in several respects. First, (like Edelstein-Keshet and Ermentrout (2000) but unlike Mogilner and Edelstein-Keshet (2002)) I am concerned with spatial distribution of actin filaments and their barbed ends; the model can then be used to compare against actin density distributions observed in experiments. I explore actin density evolution in a simplified 1D geometry (see Figure 1.8) to investigate the interplay between filament branching, growth, and decay in proximity to the leading edge. As with many previous models mentioned above, I use both analytic (this chapter) and simulation techniques (Chapter 4) to explore different possible behaviours of actin dynamics in motile cells. However, since I study a minimal model, it is possible to find (in the simplest case) explicit forms of travelling waves that represent the steady state motion of a

motile cell. This leads to analytic expressions for experimentally measurable quantities such as protrusion velocity and spatial density profiles in terms of kinetic parameters such as rates of capping, nucleation, polymerization and disassembly of filaments. A primary focus is on the role of Arp2/3 in initiating branches on filaments. By explicitly incorporating Arp2/3 activation at the leading edge, its diffusion, and its role as a nucleator of new actin filament tips that push the membrane, I can investigate consequences of distinct types of branching on the resultant actin dynamics, distribution and cell speed.

3.3 Questions to address

Taking into account experimental observations and the results of previous modelling efforts, I wish to address the following questions this chapter:

1. Can a minimal model for actin filament nucleation, capping, and depolymerization account for observed typical density profiles in a rapidly moving cell?
2. Under what conditions can this actin profile sustain traveling wave solutions typical of steady state cell motion?
3. By comparing model outputs with experimental data, is it possible to determine if Arp2/3 nucleation is more likely to form side or tip branches?

3.4 Assumptions about model geometry

The following simplifying assumptions are made regarding the geometry of the model cell.

1. The lamellipodium is a thin flat sheet, approximately 10 μm long. Its vertical thickness (~ 200 nm, Abraham et al. (1999)) is here ignored.
2. The domain is a one dimensional strip of lamellipodium (see Figure 1.8).
3. Forward protrusion of the leading edge occurs at a rate that depends on the number of barbed ends at the membrane. I mainly consider steady state motion for which the rate of membrane protrusion is constant.
4. The membrane provides constant resistance to movement.
5. Dynamic processes such as capping, branching and depolymerization are modelled using first order kinetics.

6. The actin dynamics of interest take place near the leading edge, assumed to be far from any physical barriers.
7. The number of barbed ends at the rear of the lamellipodium is negligible.

Assumption 1 about the lamellipodium geometry, made for analytical ease, is reasonable since the lamellipodium is long and flat. Assumption 2 is a simplification. 2D and 3D effects could be important, and will be examined in a later treatment. This 1D transect includes both cytoplasm and membrane. Because the lamellipodium is very thin, membrane and cytoplasmic components can easily interact and I do not treat the membrane and cytoplasm as distinct physical compartments. I use the thermal ratchet mechanism for membrane protrusion derived by Mogilner and Oster (1996). Here I simplify the dependence of the membrane speed on the number of barbed ends in assumptions 3 and 4. Capping and nucleation dynamics (Assumption 5) are likely to be more complicated than linear kinetics and I ignore saturation effects due to limited pools of the required proteins (ie. Arp2/3 and capping proteins). Assumptions 6 and 7 are based in experimental evidence suggesting that active actin polymerization takes place only at the leading edge of motile cells. Since all uncapped barbed ends are capable of polymerization, Assumptions 6 and 7 are reasonable.

3.5 Model definitions

The model employs the following variables and parameters:

$B(x, t)$	Density of actively growing barbed ends, $\#/\mu\text{m}$
$F(x, t)$	Filament length density, $\mu\text{m}/\mu\text{m}$
$A(x, t)$	Arp2/3 concentration, scaled
x_{edge}	Position of leading edge
c	Membrane speed, $\mu\text{m}/\text{s}$
v	Speed of tip growth, $\mu\text{m}/\text{s}$
x	Spatial coordinate
t	Time coordinate
z	Position relative to leading edge in moving coordinates

3.6 Assumptions about actin dynamics

I make the following further assumptions about actin dynamics in the model:

8. Nucleation events (spontaneous, tip or side branching) require active Arp2/3.
9. Arp2/3 is activated only at the membrane where it interacts with membrane-associated proteins of the SCAR/WASp family.
10. Arp2/3 diffuses in the cell and advects due to the motion of the leading edge.
11. Arp2/3 is used up by nucleation events.
12. All filaments point toward the membrane and grow in the direction of motion at a constant rate of polymerization, v .
13. Filaments are fixed with respect to the substrate and cannot cross the membrane.
14. At the leading edge, Arp2/3 is maintained at a constant concentration.

I assume that the rate of increase of barbed ends due to nucleation by Arp2/3 (in full generality) is $\eta_0 A + \eta_1 AB + \eta_2 AF$, where η_0 , the spontaneous *de novo* nucleation rate, η_1 and η_2 , the tip and side branching rates, are here approximated as constants (possibly zero). Barbed ends are capped by capping protein that stops polymerization from occurring at that tip. I take barbed end loss due to capping as $-\kappa B$ where κ is a per tip mean rate of capping. Filaments are static but barbed ends move at the speed of polymerization v , which I assume to be constant. Arp2/3 is generated at the leading edge and maintained at a constant level there, diffuses freely on the domain with diffusion rate D_R , and is used up by nucleation events. I consider three possible nucleation events: spontaneous nucleation, tip branching, and filament side branching (each proportional to Arp2/3 concentration, with rates $\eta_0, \eta_1, \eta_2 \geq 0$, respectively.) The level of Arp2/3, A , is scaled with respect to its maximal value at the cell membrane so A is dimensionless and ranges between 0 and 1.

Filaments grow by elongation at a rate that depends on tip velocity: the rate of filament length density gain by polymerization is Bv . I model filament loss as a simple linear decay, i.e. $-F\gamma$ where $1/\gamma$ is mean filament lifetime, and represents active filament turnover. Note that this is general degradation, not merely depolymerization at the pointed end of the filament.

3.7 Model equations

The model keeps track of freely polymerizing barbed ends (B), filament length density (F) and the density of Arp2/3 (A).

3.7.1 Derivation of model equations using conservation laws

Here I derive the flux terms of the actin equations in a 1D domain by keeping track of the flux of each variable, using conservation laws to ensure I am using the appropriate equations in my model.

I divide the domain into equally spaced subintervals, with size Δx (Figure 3.1). In general, I wish to determine the amount of a certain variable (barbed ends or Arp2/3) entering and leaving the subinterval $(x, x + \Delta x)$. I do not consider the flux of filaments since I am assuming that filaments are fixed with respect to the substrate (Assumption 13). As discussed in Edelstein-Keshet (1988), the rate of change of a particular variable can be expressed in terms of the flux as follows:

$$\begin{aligned} \text{rate of change in } (x, x + \Delta x) \text{ per unit time} &= \text{rate of gain in } (x, x + \Delta x) \text{ per unit time} \\ &- \text{rate of loss in } (x, x + \Delta x) \text{ per unit time} \\ &\pm \text{rate of local creation/decay per unit time} \end{aligned}$$

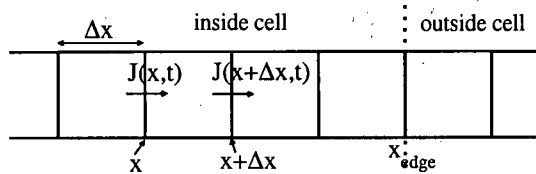


Figure 3.1: Schematic diagram of the one dimensional domain to determine the flux of barbed ends and Arp2/3.

Flux terms for barbed ends

As discussed in Chapter 3, I assume all barbed ends are oriented toward the leading edge and those inside the cell grow at a constant rate v , while those at the membrane grow at the rate of membrane movement. I define the following quantities.

$$B(x, t) = \text{number of barbed ends per unit length at } (x, t),$$

$$J_B(x, t) = \text{flux of barbed ends at } (x, t),$$

$$\theta_B(x, t) = \text{creation/decay of barbed ends per unit time in } (x, t),$$

$$\Delta x = \text{length of grid space.}$$

Then,

$$\begin{aligned} J_B(x, t) &= (\text{tips growing from left to right across } x) \\ &\quad - (\text{tips growing from right to left across } x) \\ &= vB(x - \Delta x, t) - 0. \end{aligned}$$

Similarly,

$$J_B(x + \Delta x, t) = vB(x, t).$$

Balancing the units so that both sides of the equation have units of number per unit length per unit time, the rate of change of barbed ends is

$$\begin{aligned} \frac{\partial}{\partial t}(B(x, t)\Delta x) &= J_B(x, t) - J_B(x + \Delta x, t) + \theta_B(x, t)\Delta x \\ \Rightarrow \frac{\partial}{\partial t}B(x, t) &= \frac{v}{\Delta x}(B(x - \Delta x, t) - B(x, t)) + \theta_B(x, t). \end{aligned}$$

Taking $\Delta x \rightarrow 0$,

$$\frac{\partial B}{\partial t} = -v\frac{\partial B}{\partial x} + \theta_B(x, t), \quad (3.1)$$

which is Equation (3.2a).

Using a similar argument, it is possible to derive equations describing the diffusion and advection of Arp2/3.

3.7.2 Model equations with kinetic terms

The model equations are:

$$\frac{\partial B}{\partial t} = -v \frac{\partial B}{\partial x} + \eta_0 A + \eta_1 AB + \eta_2 AF - \kappa B, \quad (3.2a)$$

$$\frac{\partial A}{\partial t} = -\frac{\partial}{\partial x} \left(-D_R \frac{\partial A}{\partial x} + \sigma A \right) - \eta_0 A - \eta_1 AB - \eta_2 AF, \quad (3.2b)$$

$$\frac{\partial F}{\partial t} = Bv - F\gamma. \quad (3.2c)$$

where σ is advective movement of Arp2/3 molecules due to cytoplasmic flow. I assume that monomers are pulled by the leading edge at the rate of motion so that

$$\sigma = \frac{dx_{edge}}{dt}.$$

In these equations, first order spatial derivatives capture the retrograde flow and/or other convective processes such as tip motion. For ease, I absorb the units and magnitude of the source of Arp2/3 at the membrane into the nucleation parameters η_i .

The corresponding boundary conditions are:

$$B(-\infty, t) = 0, \quad (3.3a)$$

$$A(-\infty, t) = 0, \quad (3.3b)$$

$$A(x_{edge}, t) = A_0. \quad (3.3c)$$

The boundary conditions for barbed ends and Arp2/3 away from the leading edge (at $x = -\infty$) are derived from Assumptions 7, 9 and 11 which suggest that barbed ends and active Arp2/3 are not found far from the leading edge. The boundary condition for Arp2/3 at the membrane is from Assumption 9, indicating that active Arp2/3 is generated only at the leading edge and is maintained at a constant level there. Since A is scaled with respect to its maximum value and the only source of active Arp2/3 is at the membrane, $A_0 = 1$.

I use a force-velocity relation based on the thermal ratchet mechanism (see Section 2.1.2 and Mogilner and Oster (1996)) to determine the speed of the membrane:

$$\frac{dx_{edge}}{dt} = v \exp\left(-\frac{\phi\delta}{k_B T B(x_{edge})}\right) = v \exp(-w/B(x_{edge})), \quad (3.4)$$

where ϕ is the load force carried by a single filament tip, δ is the filament length gained by the addition of a single monomer, k_B is the Boltzmann constant, T is temperature, and $w = \phi\delta/k_B T$

is assumed to be constant. $B(x_{edge})$ is the number of barbed ends at the membrane. I assume that barbed ends cannot cross the membrane. Equation 3.4 means that, at the membrane, tips move more slowly than immediately further back, but capping prevents unlimited accumulation of tips at the membrane. The model investigated here consists of Equations (3.2) and by looking at travelling wave solutions, I wish to determine the membrane speed, c (Equation (3.4)). Parameter values used with this model are discussed in Section 4.2.

3.8 Analysis of travelling wave solutions: spontaneous branching

In this section, I consider the situation where barbed ends are formed only by spontaneous Arp2/3 nucleation events ($\eta_0 \neq 0$, $\eta_1 = \eta_2 = 0$). The model equations are:

$$\frac{\partial B}{\partial t} = -v \frac{\partial B}{\partial x} + \eta_0 A - \kappa B, \quad (3.5)$$

$$\frac{\partial A}{\partial t} = -\frac{\partial}{\partial x} \left(-D_R \frac{\partial A}{\partial x} - \sigma A \right) - \eta_0 A, \quad (3.6)$$

$$\frac{\partial F}{\partial t} = vB - \gamma F, \quad (3.7)$$

with boundary conditions and edge motion as above.

I investigate whether this model can give rise to travelling wave solutions. I assume that the membrane moves to the right with constant speed

$$c = \frac{dx_{edge}}{dt}$$

so that $\sigma = c$. I designate the moving coordinate as $z = x - ct$ and specify that the membrane lies at the origin in this moving frame.

Transforming to moving coordinates so that

$$b(z) = b(x - ct) = B(x, t), \quad a(z) = a(x - ct) = A(x, t) \quad \text{and} \quad f(z) = f(x - ct) = F(x, t);$$

$$(v - c) \frac{db}{dz} = \eta_0 a - \kappa b, \quad (3.8)$$

$$-c \frac{da}{dz} = D_R \frac{d^2 a}{dz^2} - c \frac{da}{dz} - \eta_0 a, \quad (3.9)$$

$$-c \frac{df}{dz} = vb - \gamma f, \quad (3.10)$$

with boundary conditions:

$$b(-\infty) = 0, \quad (3.11)$$

$$a(-\infty) = 0, \quad (3.12)$$

$$f(0) = 0, \quad (3.13)$$

$$a(0) = A_0. \quad (3.14)$$

Equation (3.9) is a second order linear ODE with constant coefficients and is thus fully solvable in explicit form. Consider solutions for a of the form $a = \bar{c} \exp(\lambda z)$. Substituting this expression into equation (3.9), I find the characteristic equation:

$$D_R \lambda^2 - \eta_0 = 0$$

which has two roots:

$$\lambda_{\pm} = \pm \sqrt{\frac{\eta_0}{D_R}}, \quad (3.15)$$

where $\lambda_+ > 0$, $\lambda_- < 0$, and λ_{\pm} are always real valued. Then, the general solution to Equation (3.9) is:

$$a(z) = c_1 e^{\lambda_+ z} + c_2 e^{\lambda_- z}. \quad (3.16)$$

However, there is no active Arp2/3 far from the membrane ($a(-\infty) = 0$) making $c_2 = 0$. I also specify $a(0) = A_0$ which makes $c_1 = A_0$. So the specific solution for a is

$$a(z) = A_0 e^{\lambda_+ z}. \quad (3.17)$$

Substituting the solution for a into equation 3.8 for barbed ends and using $b(-\infty) = 0$, I find that the solution for b is

$$b(z) = \frac{\eta_0 A_0}{(v - c)(\lambda_+ + \kappa/(v - c))} e^{\lambda_+ z}. \quad (3.18)$$

I now substitute the solution for b into the equation for f (equation 3.9) and since there are no filaments at the membrane ($f(0) = 0$), the solution for f is

$$f(z) = \frac{\eta_0 A_0 v}{c(v - c)(\lambda_+ + \kappa/(v - c))(\lambda_+ - \gamma/c)} \left(e^{\gamma z/c} - e^{\lambda_+ z} \right). \quad (3.19)$$

The spatial profiles of B , A and F are shown in Figure 3.2, using parameter values from Table 4.1. Using biologically reasonable parameter values, discussed in Chapter 2 and explored further in Chapter 4, the analytic solution derived here produces spatial profiles of barbed end

and filament density that are consistent with experimental observations, satisfying Question 1. As shown in Figure 3.2, barbed ends are located very close to the leading edge while the filament density increases away from the leading edge before decaying. Active Arp2/3 is found close to the leading edge, ensuring that new barbed ends are generated where they can exert force on the membrane. This analysis shows that non-trivial travelling wave solutions are possible, addressing Question 2.

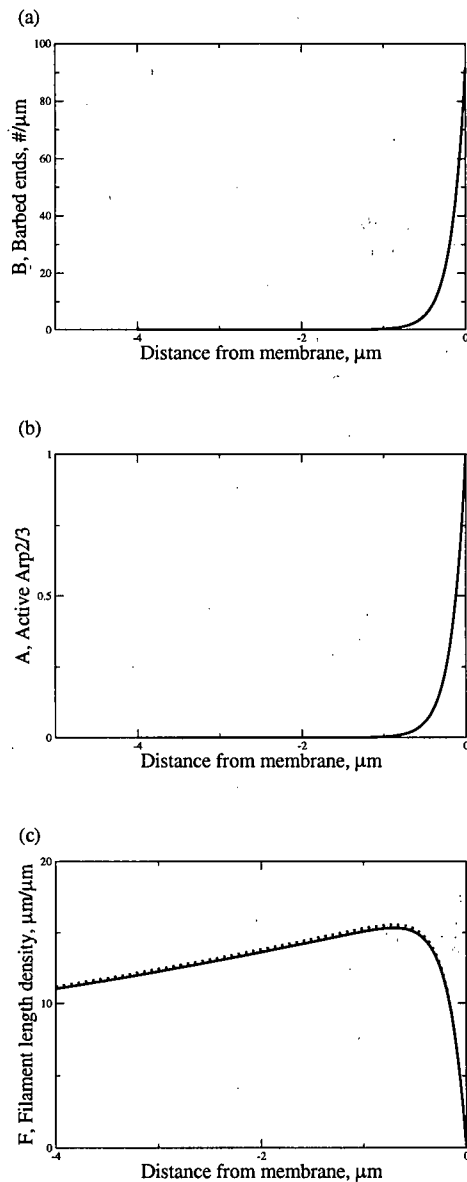


Figure 3.2: Comparison of analytic and simulation results. Plot of analytic solution (solid line) of a travelling wave solution in the spontaneous branching case as determined in Section 3.8 using $\eta_0 = 100$, and other parameter values as given in Table 2.1. (a) Profile of barbed ends, (b) Profile of Arp2/3 concentration, (c) Filament length density profile over the region $-4 \leq z \leq 0$, where z is position in μm relative to the cell membrane. Also shown is the simulation result (dotted line) discussed in Chapter 4. Arbitrary initial density distributions converged, after some transient, to the steady state wave profile shown, indicating the stability of these travelling wave solutions. There is good agreement between the analytic result and the simulations (the profiles are almost indistinguishable), suggesting this numerical implementation is adequate for capturing the model dynamics.

3.8.1 Membrane speed in terms of parameter values

I can also determine an expression for the membrane speed in the spontaneous branching case in terms of parameters. Using equations (3.4) and (3.18), I find

$$c = v \exp\left(-\frac{w}{b(0)}\right) = v \exp\left(-\frac{w(\lambda_+(v-c) + \kappa)}{\eta_0 A_0}\right). \quad (3.20)$$

For the case of spontaneous branching, this is an implicit equation that directly relates biochemical rates to the speed of membrane protrusion. In the case of spontaneous branching, it is clear from Equation (3.20) that the membrane speed will increase as the polymerization speed or nucleation rate increases and decrease as the membrane resistance force or capping rate increases. The membrane speed dependence on parameters will be explored more fully in Chapter 4. The membrane speed determined by Equation 3.20 using the parameters in Table 4.1 is $c \approx 0.3 \mu\text{m/s}$, which is consistent with observed cell speeds (Section 2.5).

3.8.2 Tip and side branching

In the case of tip ($\eta_1 \neq 0$, $\eta_0 = \eta_2 = 0$) and side ($\eta_2 \neq 0$, $\eta_0 = \eta_1 = 0$) branching, equations (3.2) are nonlinear and not easily solved using analytic techniques. To explore these two cases, I will rely on numerical simulations to produce the solution to this model in the next chapter.

3.9 Discussion

The model proposed in this chapter addresses experimental observations and builds on previous theoretical modelling efforts by studying the profile of barbed ends and filaments behind the leading edge, while taking into account spatial effects of biochemical events such as nucleation and capping. I also incorporate the "ratchet" mechanism for actin filament ends pushing forward on the membrane and generating the force that causes protrusion.

By making simplifying assumptions in constructing the model, I am able to determine an analytic formula connecting membrane speed to kinetic parameters, at least for one model variant (spontaneous nucleation). In this variant, the analytic solution for barbed end and filament length density demonstrates the existence of travelling wave solutions and produces spatial profiles and membrane speeds that correspond to experimental observations when biologically reasonable parameter values are used, even though this minimal model includes only basic events such as actin filament nucleation, capping, and depolymerization. However, with

these analytic tools I cannot easily address the stability of the travelling waves (local or global), what happens from arbitrary initial conditions or how to handle the more complicated branching types ($\eta_1 \neq 0$, $\eta_2 \neq 0$). I am also not able to compare the spatial profiles of the different branching mechanisms using the analytic approach of this chapter. For this, I perform numerical simulations, investigated in the next Chapter.

Chapter 4

Dependence of membrane speed on biochemical rates in a 1D model of a lamellipodium

In Chapter 3, I derived a model to describe the density of actin nucleated by Arp2/3 close to the cell membrane. I studied this model analytically in the case of spontaneous branching. In this chapter, I describe how biological parameter values are determined and how the equations are simulated numerically. I use simulations in this chapter to explore other cases such as tip and side branching that can not be easily solved analytically, to determine the stability of this model and its sensitivity to initial conditions. I also compare the resulting spatial profiles with experimental data to determine if certain branching types provide a better fit to the data.

4.1 Simulations

Simulating Equations (3.2) proved challenging, but transforming the equations to moving coordinates with variable membrane speed allowed me to produce a numerically stable computing algorithm. As stated, Equations (3.2) are in PDE form, and the membrane moves forward at the rate x'_{edge} (Equation (3.4)) which depends on the the number of barbed ends adjacent to the membrane. In all numerical implementations discussed here, first order transport terms are discretized using Forward Euler while second order diffusion terms are discretized using explicit centered differencing. This fully explicit scheme is often referred to as the FTCS (Forward Time Centered Space) scheme (Press et al., 1992). All simulations are performed on a 1D domain with equal grid spacing with space step size Δx . Readers not interested in the details of the initial attempts may skip ahead to Section 4.1.2.

4.1.1 Initial attempts

In my first attempt to simulate Equations 3.4, I used two variables to track the position of the membrane as it moved forward, as shown Figure 4.1. The first real valued variable, R_m ,

kept track of the distance travelled by the membrane during each time step while the second integer variable, Z_m , kept track of the grid space occupied by the membrane. For numerical stability, the membrane was not able to move the distance spanned by one grid space in one time step so several time step were needed before the membrane moved into the next grid space, incrementing the second variable, Z_m .

Although this method could be successfully implemented, I found that "jumps" in the membrane position represented by Z_m created an empty grid space immediately behind the leading edge, containing no barbed ends or filaments. This led to large variations in the number of barbed ends pushing on the membrane, making the membrane speed highly variable. Since I am interested in the steady state behaviour of this model, this implementation was not satisfactory.

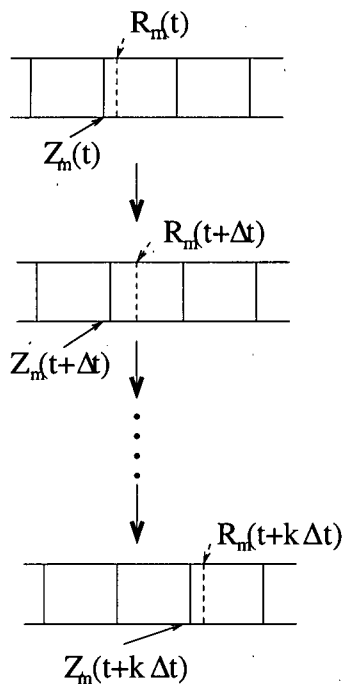


Figure 4.1: Schematic of first attempt at a computational algorithm using two variables to track the membrane position: R_m kept track of the actual membrane position as it changed at each iteration while Z_m kept track of the integer grid position designating the membrane position.

My next attempt sought to eliminate this variation caused by the membrane jumps by allowing barbed ends and filaments to grow in the space between the membrane and the closest grid space inside the cell, shown schematically in Figure 4.2. In this implementation, a sliding grid square, that contained densities of barbed ends, filaments and Arp2/3, tracked the membrane

position. The portion of the sliding grid square with width Δx_{m-1} that overlapped an interior grid square adopted the densities of that interior grid square, multiplied by the fraction of the grid space covered by the sliding grid square ($\Delta x_{m-1}/\Delta x$). The portion of the sliding grid square Δx_m that did not overlap any interior grid spaces updated the variables in the usual manner using the existing densities from the previous time step. These densities were then multiplied by ($\Delta x_m/\Delta x$) to reflect the proportion of the sliding grid square occupied by these quantities. Note that $\Delta x_{m-1} + \Delta x_m = \Delta x$ so the sum of the densities from these two parts of the sliding grid square is equivalent to an entire grid square used in the simulations. For instance, suppose the membrane is located between the boundaries of grid spaces k and $k+1$, as shown in Figure 4.2. To determine the number of barbed ends in the sliding grid square, I use the number of barbed ends already calculated for grid square k to get $B_k \Delta x_{m-1}/\Delta x$. I then use the density of barbed ends from the previous time step to calculate B_{k+1} which adds $B_{k+1} \Delta x_m/\Delta x$ barbed ends to the sliding grid square. Adding these densities together, I have

$$B_m = (B_k \Delta x_{m-1} + B_{k+1} \Delta x_m)/\Delta x,$$

where B_m is the number of barbed ends in the entire sliding grid square.

However, the membrane can sometimes move very small distances, making Δx very small and forcing the time step to be very small at each iteration for numerical stability. Even with a variable time step, this method is highly unstable and uses a substantial amount of computer time.

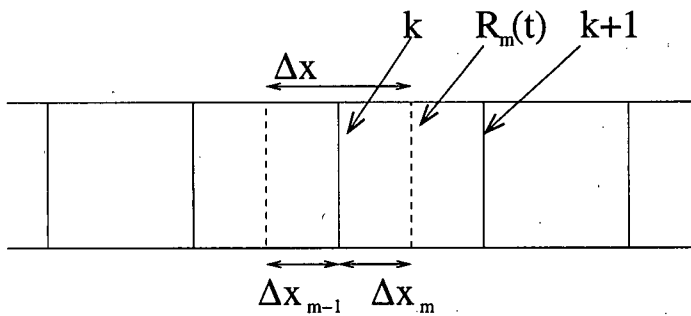


Figure 4.2: Schematic of second attempt at a computational algorithm using a sliding grid space (dashed line) to avoid membrane jumps. R_m denotes the membrane position while k and $k+1$ denote the grid space boundaries closest to the membrane position. Δx_{m-1} is the width of overlap with an internal grid space and Δx_m is the distance from the k th boundary and the membrane position R_m .

4.1.2 Successful computational algorithm

For my final attempt, I transformed Equations (3.2) to moving coordinates, as done in Section 3.8, but without assuming a constant membrane speed, shown schematically in Figure 4.3. The moving coordinates are:

$$\begin{aligned}\tau &= t, \\ z &= x - x'_{edge} \cdot t.\end{aligned}$$

The resulting transformed equations are:

$$\frac{\partial b}{\partial \tau} = (x'_{edge} - v) \frac{\partial b}{\partial z} + \eta_0 a + \eta_1 ab + \eta_2 af - \kappa b, \quad (4.1a)$$

$$\frac{\partial a}{\partial \tau} = D_R \frac{\partial^2 a}{\partial z^2} - \eta_0 a - \eta_1 ab - \eta_2 af, \quad (4.1b)$$

$$\frac{\partial f}{\partial \tau} = x'_{edge} \frac{\partial f}{\partial z} + bv - f\gamma, \quad (4.1c)$$

where x'_{edge} is calculated according to Equation (3.4) at each iteration using the number of barbed ends in the grid space adjacent to the membrane position (which is the origin in moving coordinates).

Although these are still PDEs, the frame of reference is fixed on the membrane and the equations are easily discretized and implemented numerically. I use this method for all the simulations presented in this thesis and a copy of my C code for simulating Equations (4.1) is given in Appendix A.

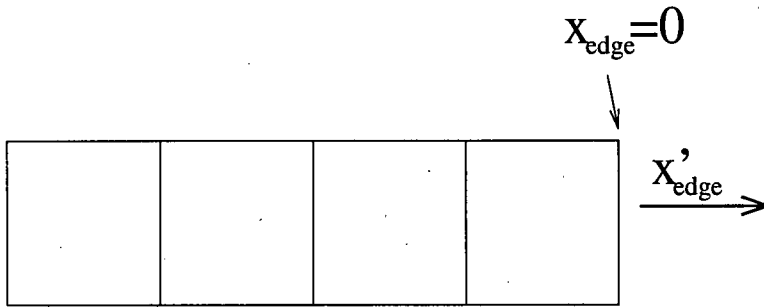


Figure 4.3: Schematic of successful final computational algorithm: I transformed Equations 3.2 to moving coordinates with variable speed. The membrane is stationary and located at the origin and barbed ends, filaments and Arp2/3 appear to experience a rearward flow at speed x'_{edge} in this coordinate system.

As mentioned above, the model is simulated numerically using explicit (upwind) differencing

for transport terms and centered differencing for diffusion terms. Where possible, the simulation results are tested against analytical predictions of Section 3.8. The discretized equations of the model in moving coordinates, coded in C, are iterated on a 1D domain $10 \mu\text{m}$ in length with step size $\Delta x = 0.01 \mu\text{m}$ and an appropriate time step Δt for stability. The simulations can be initiated from arbitrary initial distributions of the variables, but all runs are started with a non-zero density of barbed ends to assure propagation in all branching variants.

To ensure that the boundary conditions $B(-\infty) = 0$ and $A(-\infty) = 0$ are satisfied, B and A are initially set to zero on the left boundary and are not changed during the course of the simulation. A simulation run terminates at $t = 200$ seconds. Unless otherwise indicated, parameter values from Table 4.1, discussed in Section 4.2, are used.

4.2 Parameter values

Before I simulate Equations 3.2, I require parameter values. Some of these can be estimated directly from reported biological experiments. I use the capping, polymerization and filament decay rates discussed in Chapter 2 and compiled in Table 2.1.

4.2.1 Rate of Arp2/3 branching

There are no direct observations of rates of Arp2/3 nucleation in motile cells. To derive reasonable estimates for branching rates, I compared the three types of branching mechanisms, in the hypothetical case that each acts on its own. Since each branching parameter (η_0, η_1, η_2) has a distinct set of units, to make this comparison, I picked values that would lead to a similar level of actin density at the leading edge.

For spontaneous branching alone ($\eta_0 \neq 0, \eta_1 = \eta_2 = 0$) at steady state locomotion, there should be a balance between nucleation and capping so that $\eta_0 A \approx \kappa B$. Since I have scaled the activated Arp2/3 concentration so that its maximal value is $A = 1$, the parameter η_0 is an effective maximal spontaneous nucleation rate. This rate is corrected by the fraction of Arp2/3 available in a given location, relative to that at the membrane. Experiments suggest there are approximately $B(0) = 100$ barbed ends along each micron of membrane at the leading edge (Abraham et al., 1999; Bailly et al., 1999). At steady state cell locomotion, using the known capping rate, this leads to the estimate $\eta_0 A_0 \approx \kappa B(0)$ so that $\eta_0 \approx 100 \mu\text{m}^{-1} \text{s}^{-1}$. For side branching on its own ($\eta_0 = \eta_1 = 0$), the balance between branching and capping at the leading

edge implies $\eta_2 AF \approx \kappa B$, leading to the estimate $\eta_2 = \kappa B(0)/FA$. I assume that at the leading edge, there is roughly one tip per $1 \mu\text{m}$ length filament, then $\eta_2 \approx 1 \mu\text{m}^{-1}\text{s}^{-1}$. Finally, using the fact that average spacing between branch points is $\sim 0.1 \mu\text{m}$ (Wiesner et al., 2003), I can determine an equivalent value of the branching parameter in the case of tip branching on its own, i.e. $\eta_1 \approx (1 \mu\text{m}^{-1}\text{s}^{-1})(0.1 \mu\text{m}) = 0.1\text{s}^{-1}$. This reasoning leads to the set of approximately comparable branching rates:

$$\eta_0 \approx 100 \mu\text{m}^{-1}\text{s}^{-1}, \quad \eta_1 \approx 0.1\text{s}^{-1}, \quad \eta_2 \approx 1 \mu\text{m}^{-1}\text{s}^{-1}.$$

These values would produce a roughly similar leading edge density of actin if each of the three nucleation mechanisms were acting alone. Note that because in 1D the filament density is essentially dimensionless (length of filaments per unit distance), the units of η_0 and η_2 coincide.

4.2.2 Rate of Arp2/3 diffusion

To determine the diffusion rate of Arp2/3, D_R , I note the diffusion coefficient of an actin monomer, whose molecular weight is approximately 40 kDa, is $50 \mu\text{m}^2/\text{s}$ in pure water but due to effects of electrolytes, other globular proteins, and possible non-specific binding to intracellular structures, it has been revised downwards to $5 \mu\text{m}^2/\text{s}$ (James McGrath, Diffusion of actin monomers in the cell, ICAMS workshop on Biophysics of actin-based motility, Aspen Co, Sept 3-6, 2004, <http://icam.ucop.edu/workshops.html>). Since Arp2/3 has a molecular weight of approximately 220 kDa, I use the Stokes-Einstein relation to approximate its diffusion coefficient as $D_R \approx 3 \mu\text{m}^2/\text{s}$.

Parameter	Meaning	Value	Source
D_R	diffusion rate of Arp2/3	$3 \mu\text{m}^2/\text{s}$	Pollard et al. (2000)
v	polymerization velocity	$0.3 \mu\text{m}/\text{s}$	Pollard and Borisy (2003)
v_r	retrograde flow rate	$0.01 \mu\text{m}/\text{s}$	Vallotton et al. (2005)
η_0	spontaneous nucleation rate	$100 \mu\text{m}^{-1}\text{s}^{-1}$	estimated in text
η_1	nucleation rate: tip branching	0.1s^{-1}	estimated in text
η_2	nucleation rate: side branching	$1 \mu\text{m}^{-1}\text{s}^{-1}$	estimated in text
κ	capping rate	1s^{-1}	Schafer et al. (1996)
δ	depolymerization rate	$1/60\text{-}1/300 \text{s}^{-1}$	Pollard and Borisy (2003)

Table 4.1: Definitions of model parameters and typical values based on biological literature.

4.3 Results

Results shown here are for a linear initial profile of barbed ends. All other variables were set to 0 at $t = 0$. The diffusion of Arp2/3 from the edge then leads to nucleation of new tips, whose growth fills the domain with filaments. I tested the simulations with a variety of other initial barbed end distribution profiles (with compact support, i.e. $B(x, 0) = 0$ for $x \geq x_{edge}$) and found that all simulations converge after some time to a similar steady state profile. Under certain conditions, described in Section 4.3.4, steady state motion is established.

4.3.1 Analytic and simulation results of spontaneous branching case agree

As shown in Figure 3.2, the profile of barbed ends and filament length density produced by the code (dotted line) matches the analytic solution (solid line) well in the spontaneous branching case. This ensures that the simulations are accurately capturing the model dynamics and boundary conditions. Further, as shown in Figure 4.8(a), the membrane speed predicted by the numerical simulations matches the analytically predicted speed (the solid line indicating the membrane speed as determined by simulations is indistinguishable from the analytically predicted membrane speed (dot-dash line)).

4.3.2 All three branching types support travelling wave solutions

Figures 3.2 and 4.4 show the travelling wave solutions in the spontaneous, tip and side branching cases. Simulations of the spontaneous branching case agree with the analysis, while simulations of the tip and side branching extend the results to variants of the model that are not easy to treat analytically. The simulations also provide evidence for the stability of the traveling wave solutions, an issue that was not treated analytically. In all three cases, Arp2/3 has its highest value near the membrane, as expected, since Arp2/3 is activated by membrane-associated proteins (Figures 3.2, middle plot, and 4.4). Barbed ends achieve a peak density at or close to the membrane and decay rapidly towards the rear (Figures 3.2, top plot, and 4.4), while filament length density peaks further away from the membrane and decays towards the rear (Figures 3.2, bottom plot, and 4.4).

Spontaneous branching case

In the spontaneous branching case, Figure 4.4 (a), the profile of barbed ends reflects the Arp2/3 distribution since, at steady state motion, $\eta_0 r \approx \kappa b$ (from Equation 3.8). Thus the Arp2/3 profile, determined by diffusion from a source at $x = 0$, essentially leads to the b profile.

Tip branching case

In the tip branching case, Figure 4.4 (b), there is exponential growth of the barbed ends very close to the membrane where $\eta_1 A > \kappa$ and exponential decay further back. Thus, Arp2/3 is depleted at the membrane before it can diffuse into the cell.

Side branching case

In the side branching case, Figure 4.4 (c), the profile of barbed ends is a compromise between the area of high Arp2/3 and the area of high filament density. Since, by mass action, the creation of new tips is a product of the concentration of Arp2/3 and filament density, the side branching rate used in Figure 4.4 ($\eta_2 = 25 \mu\text{m/s}$) is much higher than estimated in Section 4.2 due to an overestimate of the filament density near the leading edge.

In all three cases, the filament density profile is an integral of the barbed end profile, ie. a record of barbed end motion, discounted by the actin filament decay rate.

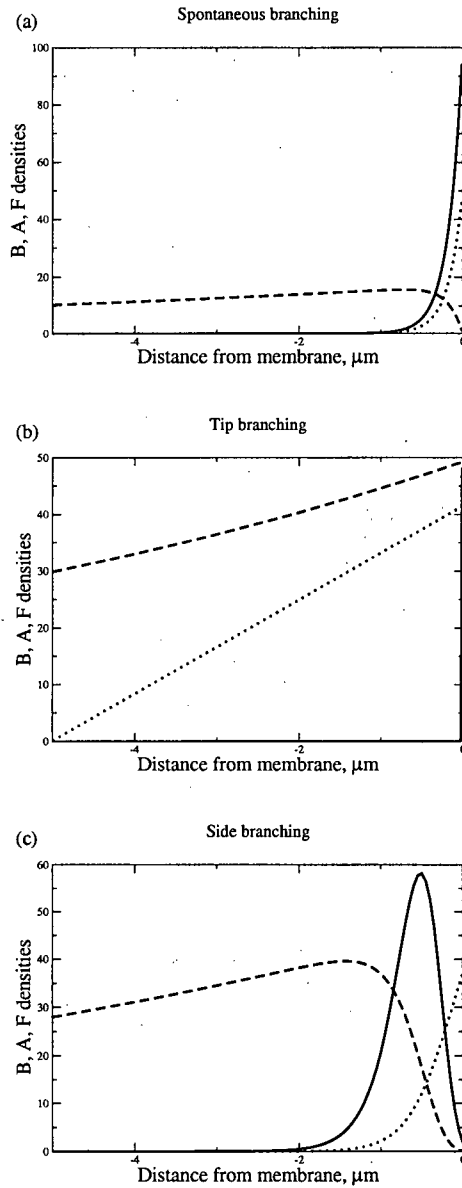


Figure 4.4: Travelling wave solutions in (a) the spontaneous nucleation, (b) tip, and (c) side branching cases. Parameter values are (a) $\eta_0 = 100\mu\text{m}^{-1}\text{s}^{-1}$, (b) $\eta_1 = 1.2\text{s}^{-1}$, (c) $\eta_2 = 25\mu\text{m}^{-1}$, and all other values as in Table 2.1. Solid line: Barbed ends (divided by 100 in (b) to enhance visibility on the same plot), dotted line: Arp2/3 (multiplied by 50 for visibility), dashed line: filament length density. Stable nontrivial travelling wave solutions exist in all three cases. Note that Arp2/3 level is maximal at the leading edge. The profiles of barbed ends and filaments are model-dependent: In the spontaneous and tip branching cases, barbed ends are maximal at the leading edge, whereas in the side branching case, their profile peaks inside the cell, at some small distance from the membrane. In the tip branching case (b), values of η_1 that lead to a travelling wave profile produce explosive growth and an unrealistically high number of tips.

4.3.3 Side branching provides best fit to experimental data

I used experimental results from Bailly et al. (1999) to compare the experimental observations with the model predictions of the number of barbed ends near the leading edge. As the tip branching case produces an unrealistic explosive growth of tips, I omit this case from parameter fitting. Figure 4.6 shows the best fit of the spontaneous and side branching cases to the data published in Bailly et al. (1999), when the data is recalibrated to include data points that appear to be outside the cell. The best fit was determined by using least squares, i.e., I minimized the sum of square differences between data points and predicted points. The parameter value that led to the smallest sum was chosen.

Experimental data

In Bailly et al. (1999), the number of barbed ends in a motile cell was determined by capping barbed ends with gelsolin then tagging gelsolin with gold particles. These gold particles could then be counted from an electron micrograph of a fixed cell. Filament density is determined from fluorescence images of polymerized actin in fixed cells. Electron and fluorescence microscopy were discussed in Chapter 1.

With this experimental protocol, the membrane is destroyed during the fixation process and is not visible in the imaged sample. They assert the membrane position is determined by the presence of a dense actin meshwork, making the peak number of barbed ends occur at the membrane. However, careful scrutiny of their data reveals barbed ends lying outside the cell. They believe these barbed ends continued polymerizing after permeabilization, causing them to grow past the membrane. Under these assumptions, the data presented in Bailly et al. (1999) is consistent with new barbed ends being generated by spontaneous branching, as shown in Figure 4.6. However, if I horizontally recalibrate their data so that non zero data points are located inside the cell, the data is consistent with side branching (Figure 4.6). Away from the leading edge, the number of barbed ends in the experimental data decays to a non-zero value. Fluorescence imaging in live cells suggests free barbed ends are only found very close to the leading edge in motile cells (Lorenz et al., 2004; Redmond and Zigmond, 1993; Symons and Mitchison, 1991). It may be that the antibody staining used in Bailly et al. (1999) is detecting barbed ends that were previously capped by endogenous gelsolin. To account for this, I also vertically recalibrate the experimental data for the purpose of data fitting.

Estimate of capping rate based on experimental data

In moving coordinates, Equation 3.8 for barbed ends far from the leading edge, assuming nucleation is negligible, is:

$$-c \frac{db}{dz} \approx -\kappa b, \quad \Rightarrow b(z) \approx \exp\left(\frac{\kappa}{c} z\right), \quad \Rightarrow \ln(b(z)) \approx \frac{\kappa}{c} z.$$

The value of κ/c can thus be estimated from a plot of the natural logarithm of the number of barbed ends as a function of distance from the leading edge, as shown in Figure 4.5. The trailing edge of the profile of barbed ends, and least squares minimization for points 0.8 - 1.1 μm away from the leading edge, suggests that $\kappa/c \approx 0.3 - 0.5 \mu\text{m}^{-1}$. If the leading edge were to move at close to its maximum speed, $c \approx 0.3 \mu\text{m/s}$, then I estimate that $\kappa \approx 0.09 - 0.15 \text{s}^{-1}$. By taking sample points closer to the leading edge, I can find higher capping rate estimates. For the profiles shown in Figure 4.6, I use $\kappa = 0.1 \text{s}^{-1}$. This is surprisingly low, given that capping rates in the lamellipodium are estimated to be in the range of 1s^{-1} .

Estimate of nucleation rate based on experimental data

I find those values for the nucleation rate that best match the peak value of barbed ends in the experimental data to be $\eta_0 \approx 25 \mu\text{m}^{-1} \text{s}^{-1}$ and $\eta_2 \approx 2 \mu\text{m}^{-1} \text{s}^{-1}$. The ratio of η_0/η_2 is much smaller here than would be expected from the estimates in Section 4.2 due to an overestimate of the filament density at the leading edge. The lower absolute value of both nucleation rates is due to the lower capping rate: barbed ends are not capped as quickly so do not need to be nucleated as quickly.

Comparison of barbed end spatial profiles to experimental data

Figure 4.6 shows the predicted model profiles in comparison to the manually re-digitized data from Bailly et al. (1999). Both the spontaneous nucleation (Figure 4.6(a)) and the side branching (Figure 4.6(b)) cases are shown. Some aspects, including quantitative comparison, demonstrate differences.

When the experimental data is shifted 0.2 μm to the left and down by 25 $\#/\mu\text{m}$, the side branching case (b) matches the experimental data better, especially close to the leading edge. It is possible to shift the peak of barbed ends to better match the experimental data by increasing the capping and nucleation rates, but this causes an even sharper decay in the barbed end profile.

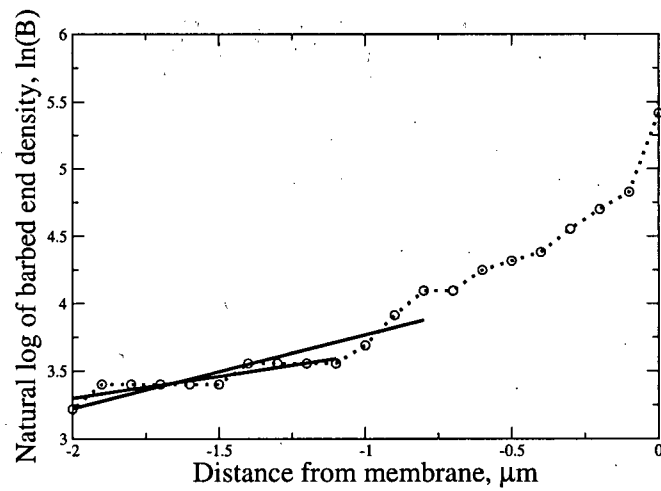


Figure 4.5: Experimental data from Bailly et al. (1999) (dotted line with circles), plotted as the natural log of the number of barbed ends, $\ln(B)$, as a function of distance from the leading edge. The slope of this curve (as shown by the solid lines) is used to estimate the range of κ/c in the model, from which we estimate the effective capping rate, κ . See Section 4.3.3 for details.

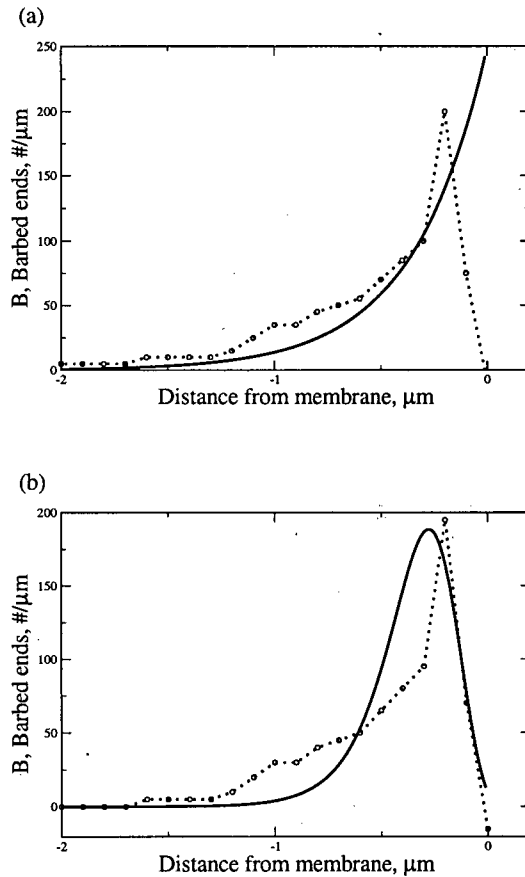


Figure 4.6: Model predictions of barbed end profiles (solid line) fit to experimental data (dotted line) in the spontaneous (a) and side (b) branching cases. The experimental data is reproduced from Bailly et al. (1999), Figure 10, left panel, then shifted down and to the left, as discussed in Section 4.3.3. The tip branching case is omitted due to explosively high tip growth. The parameter values used to produce the profiles shown here are $\kappa = 0.1\text{s}^{-1}$ in both plots, $\eta_0 = 25\mu\text{m}^{-1}\text{s}^{-1}$ in (a) and $\eta_2 = 2\mu\text{m}^{-1}\text{s}^{-1}$ in (b). (The parameters η_i were adjusted to fit the height of the profiles.) See Section 4.3.3 for a discussion of the capping rate approximation. The side branching case provides the best fit to the data.

Comparison of filament density profiles to experimental data

I compare the predicted filament density profile in the side branching case to data from Bailly et al. (1999) that has been scaled to have the same maximum value as the simulation profile. I find that a depolymerization rate of $\gamma = 0.1s^{-1}$ provides the best fit to experimental data when the experimental data is shifted $0.4 \mu\text{m}$ to the left (Figure 4.7(a)). The profile of filament density in the side branching case is also consistent with fluorescence profiles of polymerized actin in Svitkina and Borisy (1999) and Redmond and Zigmond (1993) (not shown).

Fluorescence profiles of Arp2/3 concentration in lamellipodia have been published in Bailly et al. (1999) and Svitkina and Borisy (1999), but these include Arp2/3 that has been incorporated into branch points of the actin meshwork which does not allow for a direct comparison to this model. Overall, I find that the side branching case in this model captures the dynamics at the leading edge better than the spontaneous or tip branching cases.

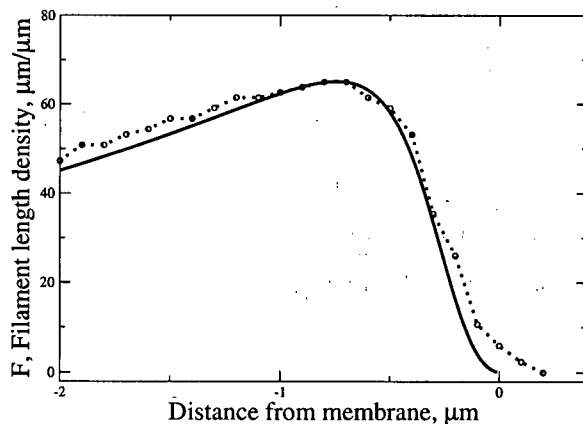


Figure 4.7: Model predictions of filament density profiles (solid line) fit to experimental data (dotted line) in the side branching case. The height of the experimental data has been scaled to match the height of the simulation result. (The spontaneous and tip branching cases are not considered here, as the side branching case was found to produce the best fit to experimental data for the number of barbed ends near the leading edge; see Figure 4.6). The best fit of filament density in the side branching case to the experimental data from Bailly et al. (1999) was found using $\gamma = 0.1s^{-1}$ and shifting the experimental data $0.4 \mu\text{m}$ to the left. The simulation profile also matches favourably to fluorescence data of filament density in Svitkina and Borisy (1999).

4.3.4 Dependence of membrane speed in biochemical rates

I compared the dependence of membrane speed on various parameters in the three branching variants of the model. In general, influences that lead to a reduction in the density of barbed ends at the membrane will impede protrusion, whereas processes that lead to an increase in those barbed ends will lead to higher protrusion velocity. To base a comparison on the values of the branching rates, I chose a range of values of each of the parameters η_0, η_1, η_2 in proportion of 100: 0.1: 1 units, as explained in Section 4.2. Figures 4.8 and 4.9 were generated by running simulations of Equations 4.1 with different parameter sets for 200 seconds, ensuring that a steady-state velocity was reached. Parameters were varied one at a time and the resulting membrane speeds were compiled in Figures 4.8 and 4.9.

Effect of nucleation rate

Figure 4.8(a) shows that the membrane speed increases as the nucleation rate increases. This is intuitively clear since, all else being equal, for greater nucleation rates, there will be a higher density of barbed ends pushing the membrane. As shown in Figure 4.8(b), in all three cases, the cell moves very slowly at a rate close to zero if the nucleation rate is too low; very low values of nucleation cannot sustain traveling wave solutions in the model because not enough barbed ends are available to push the membrane forward. The few barbed ends pushing on the membrane are unable to overcome the membrane's resistance to movement and the cell moves at a very slow rate (from Equation 3.4, the membrane speed can only be zero when $b=0$, but for low nucleation rates, the membrane speed is very close to zero). In the spontaneous and side branching cases, the membrane speed smoothly increases as η_0, η_2 increases.

For tip branching, the membrane speed jumps from zero to near its maximum (see equation 3.4) as η_1 varies in a small range from 1.1 to 1.2 s^{-1} , with all other parameter values as given in Table 2.1. This can be understood from equation (3.2a): if $\eta_1 r < \kappa$, the solution decays to zero everywhere whereas for $\eta_1 r > \kappa$, the solution grows exponentially. In this tip branching case, the discontinuity in the membrane speed suggests that the model is inadequate: a higher nonlinearity in the tip decay term would be required to prevent explosive growth, as, for example, with logistic growth. Based on these simulations, the tip branching case, as is, cannot be considered as a workable mechanism, and requires modification.

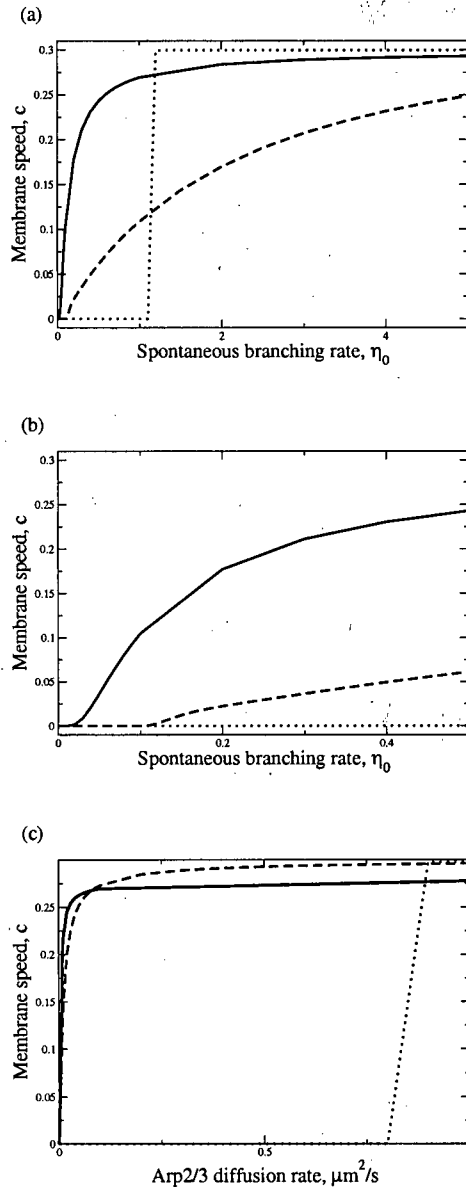


Figure 4.8: Dependence of the predicted cell protrusion speed, c , on parameters in the model. Speed increases as nucleation rates and Arp2/3 diffusion rate increase (with all other parameters as in Table 2.1.) In each panel the spontaneous (solid line), tip (dotted line) and side (dashed line) branching cases are shown. (a) Speed versus nucleation rates over a range equivalent to $0 \leq \eta_0 \leq 4 \mu\text{m}^{-1} \text{s}^{-1}$: Note that the rates η_1, η_2 used for tip and side branching were scaled in proportion to η_0 as discussed in Section 4.3.4. (The analytically predicted membrane speed in the spontaneous branching case agrees so closely with the simulation predictions that it superimposes exactly on the solid curve.) (b) Same as in (a) but for a smaller range $0 \leq \eta_0 \leq 0.4 \mu\text{m}^{-1} \text{s}^{-1}$, showing that the cell stalls ($c \approx 0$) if nucleation rates are too low. (c) Speed c versus Arp2/3 diffusion. Membrane speed increases to a maximum value determined by Equation 3.4 as Arp2/3 diffusion increases. The membrane speed increases sharply for Arp2/3 diffusion in the range $0 \leq D_R \leq 0.1 \mu\text{m}^2/\text{s}$, significantly lower than our estimated Arp2/3 diffusion rate of $3 \mu\text{m}^2/\text{s}$. In the spontaneous and side branching cases, the membrane speed varies smoothly as parameters of interest are varied while in the tip branching case, motion is all-or-none.

Effect of Arp2/3 diffusion rate

I find that increasing the rate of Arp2/3 diffusion causes the membrane speed to increase, up to a maximum value determined by Equation 3.4 (Figure 4.8(c)). Increasing the Arp2/3 diffusion rate causes the profile of Arp2/3 to decay more slowly, allowing more barbed ends to be nucleated further into the cell, away from the leading edge. These tips then grow forward to the membrane (since polymerization speed is faster than the membrane speed) where they exert force on the membrane.

Effect of membrane resistance, filament decay and capping rate

Increasing membrane resistance leads to a slight decrease in membrane speed (Figure 4.9(a)). This is consistent with the thermal ratchet equation (Equation 3.4) since membrane resistance impedes motion. Importantly, increasing the rate of filament decay causes a decrease in the membrane speed only in the side branching case as fewer filaments are available for new tip formation (Figure 4.9(b)). The decrease in the membrane speed as the capping rate increases is due to barbed ends being capped more rapidly (Figure 4.9(c)).

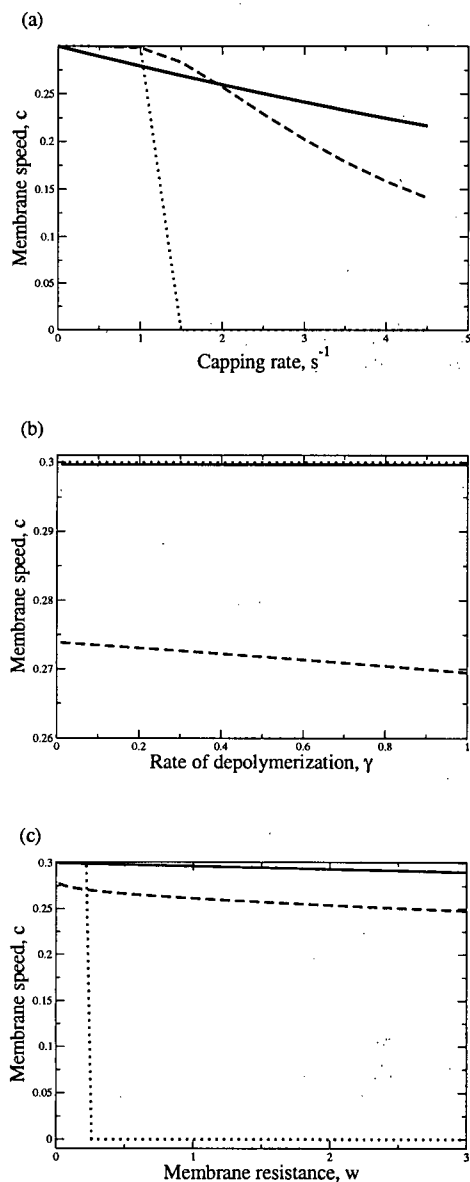


Figure 4.9: Membrane speed versus (a) capping rate (s^{-1}), (b) depolymerization rate (s^{-1}), and (c) membrane resistance ($\#/\mu\text{m}$). (all other parameters as in Table 2.1). The spontaneous (solid line), tip (dotted line) and side (dashed line) branching cases are shown. As the depolymerization rate increases in (b), only the side branching case displays decreased membrane speed, as expected. As in Figure 4.8, the membrane speed in the spontaneous and side branching cases varies smoothly as parameters of interest are varied while in the tip branching case, motion is all-or-none.

4.4 Discussion

In this chapter, I explored Arp2/3-mediated actin dynamics (Equations (3.2)) numerically. I found that analytic and simulation results agree to close precision. Simulations of the side branching case, which is analytically challenging even with simplifying assumptions, provides support for the existence of traveling wave solutions. Travelling wave solutions can be interpreted as "steady state" motion of a crawling cell.

I explored distinct nucleation mechanisms (spontaneous, tip branching, or filament side branching) to study how these would affect the observed density profiles and speeds. Tip branching in the presence of linear capping kinetics generates aberrant behaviour, including explosive growth or collapse of the barbed end density close to the membrane. Thus, this variant of the model should be rejected, or modified with suitable nonlinear (e.g. logistic) growth terms to be biologically relevant. These results suggest that the tip branching of actin filaments would be a less robust or reliable mechanism than filament side branching for controlling actin density. Some papers in the literature have suggested that Arp2/3 mediates tip-branching (Pantaloni et al., 2000). Recently, experimental and theoretical evidence for side branching has been compelling (see, for example, Carlsson et al. (2004), and references therein). The model presented here provides further support that the tip-branching hypothesis has some difficulties.

I investigated the dependence of the wave speed (i.e. the motility of the cell) on biochemical parameters. Under the conditions of the model, and assuming all parameters are non-zero, the model supports travelling waves in the spontaneous and side branching cases except when the nucleation rate is too small. These results suggest that membrane speed can be smoothly varied by extracellular signals that lead to downstream adjustment of parameters such as the rate of Arp2/3 activation or the capping rate (for example, by pathways that impinge on Rho proteins). The case of tip branching is less relevant biologically: there are ranges of each parameter value for which travelling wave solutions do not exist.

Finally, I used the observed actin densities to estimate some of the biochemical parameters by comparing the spatial profiles obtained from our model with experimental profiles from Bailly et al. (1999). The best fit was obtained by shifting the data $0.2 \mu\text{m}$ to the left and $25 \#/\mu\text{m}$ down. I speculate that the horizontal shift was needed to compensate for the difficulty of identifying the true position of the membrane experimentally, as the membrane is destroyed in the process of preparing the cell for FDS imaging (Bailly et al., 1999). The vertical shift may

stem from a background of barbed ends that had been capped by endogenous gelsolin prior to the experiment.

In the side branching case, the nucleation rate that provided a close fit to the experimental data ($\eta_2 = 2\mu\text{m}^{-1}\text{s}^{-1}$) was close to the estimate based on experimental evidence. However, the capping rate found by analyzing the decay rate of the experimental data is lower than the usual capping rate of 1s^{-1} quoted in the literature (Pollard et al., 2000; Schafer et al., 1996). (But note at the leading edge the capping rate may be of order 0.1s^{-1} according to Grimm et al. (2003) and Mogilner and Edelstein-Keshet (2002).) The depolymerization rate found by comparing fluorescence data with simulation results is higher than estimates of filament depolymerization by ADF/cofilin found in the literature (Pollard et al., 2000). This discrepancy is not surprising since there are many other factors in a motile cell that sever or otherwise degrade filaments, leading to a faster decay rate than for ADF/cofilin acting alone. The depolymerization rate $\gamma = 0.1\text{s}^{-1}$ gives a mean filament life-time of 10 s which is consistent with experimental observations of filament turnover time in lamellipodia (Theriot and Mitchison, 1991). Shifting the experimental data for filament density from Bailly et al. (1999) $0.4\mu\text{m}$ to the left provided the best fit. While the data is taken from a different cell, the cell is prepared in the same manner as described for the barbed end data, requiring destruction of the cell membrane. I cannot dismiss the fact that this model may fail to capture some essential processes that would account for the discrepancy between model and experimental data. This suggests that further investigation of capping dynamics near the leading edge, perhaps by modifying this model to include a distinct capping zone, is in order.

This model of actin dynamics is already capable of reproducing many of the qualities observed in motile cells, including spatial profiles of barbed ends and filament density and protrusion velocities. However, I have assumed that biochemical rates that control capping and Arp2/3 activation are constant. I have also assumed the cell is already polarized and in motion so this model cannot explain how a cell polarizes and initiates movement. In Chapter 6, I discuss Rho proteins, known regulators of actin dynamics and in Chapter 7, I connect a model of actin dynamics with a model of Rho protein dynamics.

In the next chapter, I extend the model investigated here to include retrograde flow, a bulk rearward flow of the actin meshwork, observed in lamellipodia of motile cells. I wish to determine what effect, if any, retrograde flow has on membrane speed and spatial profiles predicted by this model.

Chapter 5

Effect of retrograde flow on spatial profiles and membrane speed in a 1D model of a lamellipodium

A small rearward flow of the actin meshwork with respect to the leading edge has recently been observed in the lamellipodia of moving keratocytes (Jurado et al., 2005; Ponti et al., 2004; Vallotton et al., 2005). This had been observed previously in slower moving cells such as fibroblasts (Henson et al., 1999; Ponti et al., 2005). In keratocytes, the lamellipodium is separated from the cell body by a band rich in myosin II, a motor protein that binds to actin filaments and moves towards the barbed end of a filament (Svitkina and Borisy, 1999). Since most actin filaments in the lamellipodium are oriented with their barbed ends in the direction of motion (Svitkina and Borisy, 1999), the interaction of myosin II with the actin filaments in the lamellipodium causes a bulk flow of the actin meshwork away from the leading edge. Retrograde flow in keratocytes is smallest in the middle of the lamellipodium (approximately $0.01 \mu\text{m/s}$) increasing to approximately $0.05 \mu\text{m/s}$ at the edges, in cells moving $0.2\text{-}0.3 \mu\text{m/s}$ (Jurado et al., 2005; Vallotton et al., 2005). In the previous chapter, this retrograde flow was not considered.

Reviewers of our manuscript, Dawes et al. (2006), pointed out that Equations 3.2 did not take into account a feature that has been studied experimentally, namely this rearward flow of the cytoskeleton. To respond to this suggestion, I modified the model developed in Chapter 3 and studied the effect of such a flow on the behaviour of this model.

In this chapter, I consider the effect of retrograde flow on membrane speed and spatial profiles of actin filaments and barbed ends. I consider only spontaneous and side branching as tip branching case produces aberrant behaviour (Chapter 4).

5.1 Model incorporating retrograde flow

I make the following additional assumptions to clarify the role of retrograde flow in the model of actin dynamics.

1. In the fixed (lab) frame of reference, retrograde flow is constant with rate v_r and spatially homogeneous.
2. Barbed ends and filaments experience a retrograde flow away from the leading edge.
3. Arp2/3 diffuses in the cell and possibly advects, due to the motion of the leading edge and/or retrograde flow.

Filaments and barbed ends flow away from the leading edge at rate of retrograde flow v_r and barbed ends also move at the speed of polymerization v , which I assume to be constant. The modified model is then:

$$\frac{\partial B}{\partial t} = (v_r - v) \frac{\partial B}{\partial x} + \eta_0 A + \eta_1 AB + \eta_2 AF - \kappa B, \quad (5.1)$$

$$\frac{\partial A}{\partial t} = D_R \frac{\partial^2 A}{\partial x^2} - \eta_0 A - \eta_1 AB - \eta_2 AF + v_{bulk} \frac{\partial A}{\partial x}, \quad (5.2)$$

$$\frac{\partial F}{\partial t} = v_r \frac{\partial F}{\partial x} + Bv - F\gamma, \quad (5.3)$$

where

$$v_{bulk} = \alpha_1 v_r - \alpha_2 x'_{edge}.$$

I consider three limiting forms for the bulk advection, v_{bulk} , of Arp2/3 in which v_{bulk} is

- (i) precisely equal to forward membrane protrusion ($\alpha_1 = 0, \alpha_2 = 1$),
 - (ii) determined only by retrograde flow ($\alpha_1 = 1, \alpha_2 = 0$)
- and (iii) a superposition of the two ($\alpha_1 = 1, \alpha_2 = 1$).

Of these options, (iii) would be most realistic.

I take the boundary conditions as before (Equations (3.3)) and modify the force-velocity relation describing the speed of the membrane to take into account retrograde flow:

$$\frac{dx_{edge}}{dt} = (v - v_r) \exp\left(-\frac{\phi\delta}{k_B T B(x_{edge})}\right) = (v - v_r) \exp(-w/B(x_{edge})) \quad (5.4)$$

where $w = \phi\delta/k_B T$ is assumed to be constant.

5.1.1 Analysis of modified model

I again consider spontaneous branching ($\eta_0 \neq 0, \eta_1 = \eta_2 = 0$) and transform the model to moving coordinates.

$$-c \frac{db}{dz} = (v_r - v) \frac{db}{dz} + \eta_0 a - \kappa b, \quad (5.5)$$

$$-c \frac{da}{dz} = D_R \frac{d^2 a}{dz^2} - \eta_0 a + v_{bulk} \frac{da}{dz}, \quad (5.6)$$

$$-c \frac{df}{dz} = v_r \frac{df}{dz} + vb - \gamma f, \quad (5.7)$$

with boundary conditions $b(-\infty) = 0, r(-\infty) = 0, f(0) = 0, r(0) = A_0$.

Using the same technique as in Chapter 3, I find

$$a(z) = A_0 e^{\lambda_+ z}, \quad (5.8)$$

$$b(z) = \frac{\eta_0 A_0}{(v - v_r - c)\lambda_+ + \kappa} e^{\lambda_+ z}, \quad (5.9)$$

$$f(z) = \frac{\eta_0 A_0 v}{((v - v_r - c)\lambda_+ + \kappa)((v_r + c)\lambda_+ - \gamma)} \left(e^{\gamma z / (v_r + c)} - e^{\lambda_+ z} \right), \quad (5.10)$$

where

$$\lambda_{\pm} = \begin{cases} \pm \sqrt{\frac{\eta_0}{D_R}}, & (i) \\ \frac{-(v_r + c) \pm \sqrt{(v_r + c)^2 + 4D_R \eta_0}}{2D_R}, & (ii) \\ \frac{-v_r \pm \sqrt{v_r^2 + 4D_R \eta_0}}{2D_R}, & (iii) \end{cases} \quad (5.11)$$

for the three cases, (i) $\alpha_1 = 0, \alpha_2 = 1$, (ii) $\alpha_1 = 1, \alpha_2 = 0$ and (iii) $\alpha_1 = 1, \alpha_2 = 1$. As before, $\lambda_+ > 0, \lambda_- < 0$, and λ_{\pm} are always real valued.

Using equations (5.4) and (5.9), I obtain an implicit equation for the speed c ,

$$c = (v - v_r) \exp\left(-\frac{w}{b(0)}\right) = (v - v_r) \exp\left(-\frac{w(\lambda_+(v - v_r - c) + \kappa)}{\eta_0 A_0}\right). \quad (5.12)$$

5.2 Retrograde flow and Arp2/3 transport mechanism have little effect on the spatial profile of barbed ends, Arp2/3 and filament density

The measured velocity of retrograde flow in the lamellipodium of keratocytes ranges from 0.01 $\mu\text{m/s}$ to 0.05 $\mu\text{m/s}$ (Jurado et al., 2005; Vallotton et al., 2005). For simulation purposes, and since the domain of interest is in the middle of the lamellipodium, away from any edges, I use $v_r = 0.01 \mu\text{m/s}$. Figure 5.1 is a plot of the spatial profiles of barbed ends, Arp2/3 and filament

density for three different values of retrograde flow: $v_r = 0, 0.01$ and $0.1 \mu\text{m/s}$. There is very little difference in the spatial profiles: only the filament density shows a small difference for the different values of retrograde flow. A similar result occurs in simulations of the side branching case (Figure 5.2) when I compare the spatial profiles resulting from different retrograde flow rates. In the side branching case, there are slight differences in both the barbed ends and filament density profile due to retrograde flow. However, the differences are minor and retrograde flow again appears to have little effect on the spatial distribution of barbed ends, Arp2/3 or filament density in both the spontaneous and side branching cases. Figure 5.3 shows that membrane speed decreases as the retrograde flow rate increases, as expected.

A comparison between the three types of Arp2/3 transport was also made. The three options are:

- (i) Arp2/3 is transported forward by the action of the membrane protruding ($\alpha_1 = 0, \alpha_2 = 1$),
- (ii) Arp2/3 is trapped in the actin meshwork and is pulled away from the leading edge at the rate of retrograde flow ($\alpha_1 = 1, \alpha_2 = 0$),
- (iii) Arp2/3 experiences both forward transport and backward pulling ($\alpha_1 = 1, \alpha_2 = 1$).

The spatial profiles produced by these three options in both the spontaneous and side branching cases are indistinguishable when plotted, so only option (i) is shown in Figures 5.1 and 5.2. This suggests that diffusion is the primary method of Arp2/3 transport and that backward advection due to retrograde flow has no significant impact on the spatial distribution of Arp2/3, at least in the parameter regime characteristic of keratocytes.

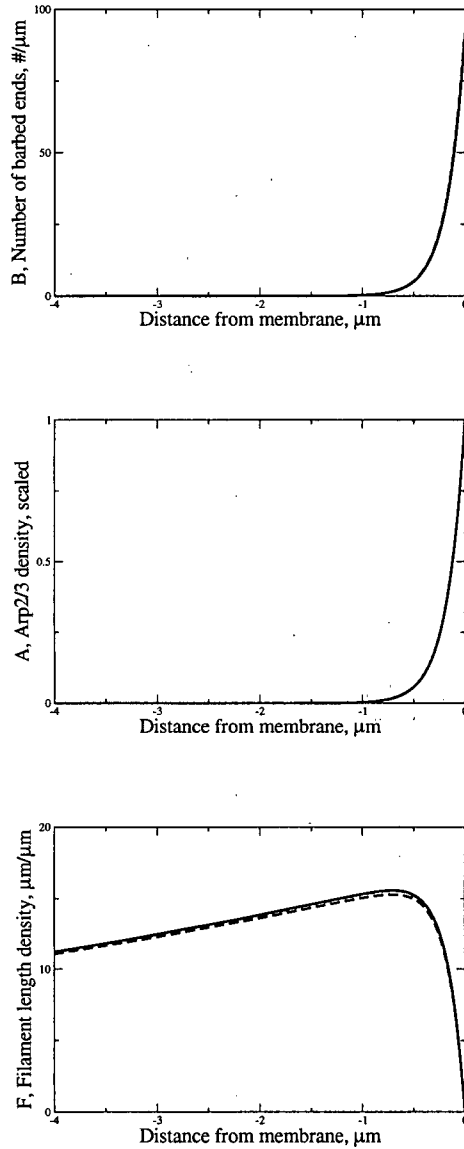


Figure 5.1: Comparison of spatial profiles in the presence of retrograde flow in the spontaneous branching case showing that retrograde flow has no significant impact on spatial profiles. The three possible scenarios of Arp2/3 transport ((i) $\alpha_1 = 0, \alpha_2 = 1$, (ii) $\alpha_1 = 1, \alpha_2 = 0$, (iii) $\alpha_1 = 1, \alpha_2 = 1$, see Section 5.2 for details) produce indistinguishable spatial profiles so only option (i) is plotted here (solid line). The spatial profile of option (i) in the absence of retrograde flow is indistinguishable from the profile that occurs in the presence of retrograde flow. Also shown is the spatial profile when the retrograde flow rate is increased ten-fold to $v_r = 0.1 \mu\text{m/s}$ (dashed line). Top: Profile of barbed ends, middle: Profile of Arp2/3 concentration, bottom: Filament length density profile over the region $-4 \leq z \leq 0$, where z is position in μm relative to the cell membrane. Parameter values used are given in Table 4.1. When considering diffusion and advection of Arp2/3, there is very little difference between the profiles, indicating that diffusion is primarily responsible for the spatial distribution of Arp2/3 which, in turn, determines the spatial profiles of barbed ends and filament density. It is also apparent that retrograde flow (assumed constant) even at ten times the experimentally determined speeds in keratocytes has little effect on the spatial profiles.

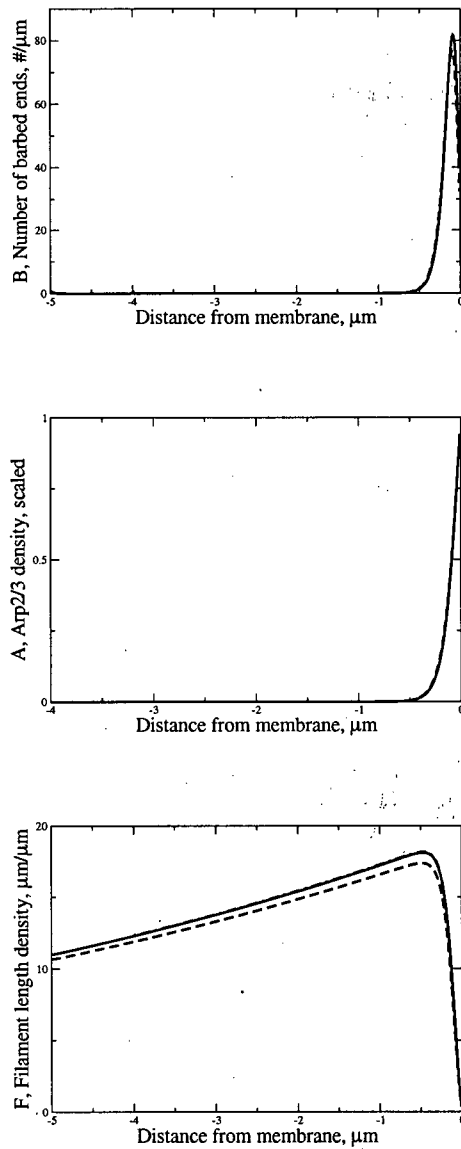


Figure 5.2: As in Figure 5.1 showing that retrograde flow has little effect on spatial profiles in the side branching case. The spatial profile of option (i) in the absence of retrograde flow is not visible as it coincides with the plotted spatial profiles. Also shown is the spatial profile when the retrograde flow rate is increased ten-fold to $v_r = 0.1 \mu\text{m}/\text{s}$ (dashed line). Parameter values used are given in Table 2.1. As in the spontaneous branching case (Figure 5.1), there is little difference in the spatial profiles as a result of retrograde flow.

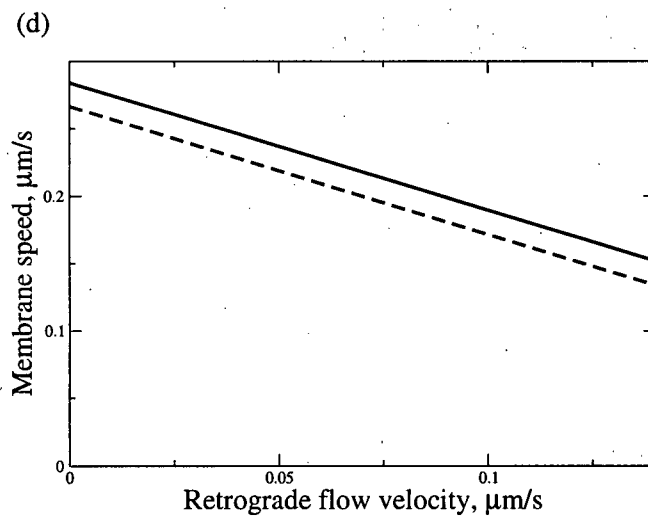


Figure 5.3: Effect of retrograde flow speed on calculated membrane speed for the three possible scenarios for Arp2/3 transport in the spontaneous branching case. All three options (solid line) agree very closely, to within five digits of accuracy, and are indistinguishable from each other. Also shown is the effect of retrograde flow on membrane speed in the side branching case using option (i) (dashed line). This suggests that, not only is this model insensitive to the manner of Arp2/3 transport (provided diffusion is sufficiently fast), but also that this model is not significantly affected by neglecting retrograde flow at the rates observed in keratocyte lamellipodia ($v_r \approx 0.01 \mu\text{m/s}$).

5.3 Discussion

This version of the model attempts to address the effect of retrograde flow on the characteristic actin densities seen in motile cells. Retrograde flow in keratocytes is slow ($\sim 1 - 3 \mu\text{m}/\text{min}$, Jurado et al. (2005); Ponti et al. (2004); Vallotton et al. (2005)), compared to observations of retrograde flow in slow moving cell types, such as neural growth cones ($\sim 2 - 10 \mu\text{m}/\text{min}$, Jurado et al. (2005); Lin et al. (1996)). However, this model does not apply to slow moving cells as I do not take into account inhomogeneous adhesion and contraction forces, nor membrane instabilities due to filopodial extension. Also, this model is concerned with actin dynamics in the middle of a keratocyte lamellipodium, not at the sides where geometry and membrane tension play a more significant role. In the centre forward part of a keratocyte lamellipodium, retrograde flow is small ($0.01 \mu\text{m}/\text{s}$, Jurado et al. (2005); Vallotton et al. (2005)) and even when it is increased ten-fold to $0.1 \mu\text{m}/\text{s}$, retrograde flow has a negligible effect on actin spatial profiles and membrane speed predicted by the model. I also find that diffusion plays the most significant role in determining the spatial profile of Arp2/3.

I made a number of simplifying assumptions when incorporating retrograde flow in this model of actin dynamics. For instance, retrograde flow may not be constant. In slow moving cells, retrograde flow appears to vary periodically (Ponti et al., 2005). Incorporating this periodic variation in retrograde flow does lead to periodic variation in the number of barbed ends at the leading edge but has little effect on the filament density profile. I also didn't consider spatially inhomogeneous retrograde flow where the flow may be faster or slower at the leading edge compared to farther back in the lamellipodium, although this has not been observed experimentally. Provided the retrograde flow has no large discontinuities, spatially inhomogeneous retrograde flow would sharpen or widen the distribution of barbed ends near the leading edge and consequently the filament distribution. This effect can be duplicated by varying biochemical parameters such as the rate of capping or Arp2/3 diffusion.

Based on these results, I conclude that retrograde flow does not significantly impact this model of actin dynamics and I do not incorporate retrograde flow into future versions of this model used to investigate regulation of actin dynamics by upstream effectors (Chapters 7 and 9).

Chapter 6

Rho proteins and cell motility

In Chapters 3-5, I investigated actin dynamics in a 1D model of a lamellipodium. Using reasonable assumptions about branching dynamics in lamellipodia and assuming the biochemical rates that govern branching and capping are constant everywhere in the cell, the side branching model produced spatial profiles of barbed ends and actin filaments that are consistent with experimental data. The model predicted reasonable cell speeds based on the number of barbed ends exerting force on the membrane. It also appears that retrograde flow at speeds typical of keratocytes has little effect on actin dynamics. However, actual biochemical rates that govern nucleation, capping and other processes are not constant but are regulated by upstream signalling molecules. I also assumed the cell was already polarized and moving in a specific direction. Here I start to address how polarization and directed movement could be initiated in a motile cell. Important regulators of the actin dynamics are a family of proteins called the Rho proteins. Some of the downstream effects of these proteins are shown in Figure 6.1. The Rho proteins act as molecular switches by converting between an active and inactive state. When a cell is exposed to an external signal, active Rho proteins form spatial gradients, influencing the activation of other Rho proteins through crosstalk and spatially regulating actin polymerization by influencing biochemical rates.

This chapter reviews a model of Rho protein dynamics developed in Jilkinė (2005) and Marée et al. (2006). I present these details since Rho proteins are significant regulators of actin dynamics and provide important background for my 1D model that incorporates the activity of upstream signalling molecules and their effect on actin dynamics, explored further in Chapters 7 and 9.

6.1 Biological background

6.1.1 Small G proteins

Small G proteins are GTPases, members of the G protein family, which bind to the nucleotide guanine and associate with the inner surface of the plasma membrane. Small G proteins consist

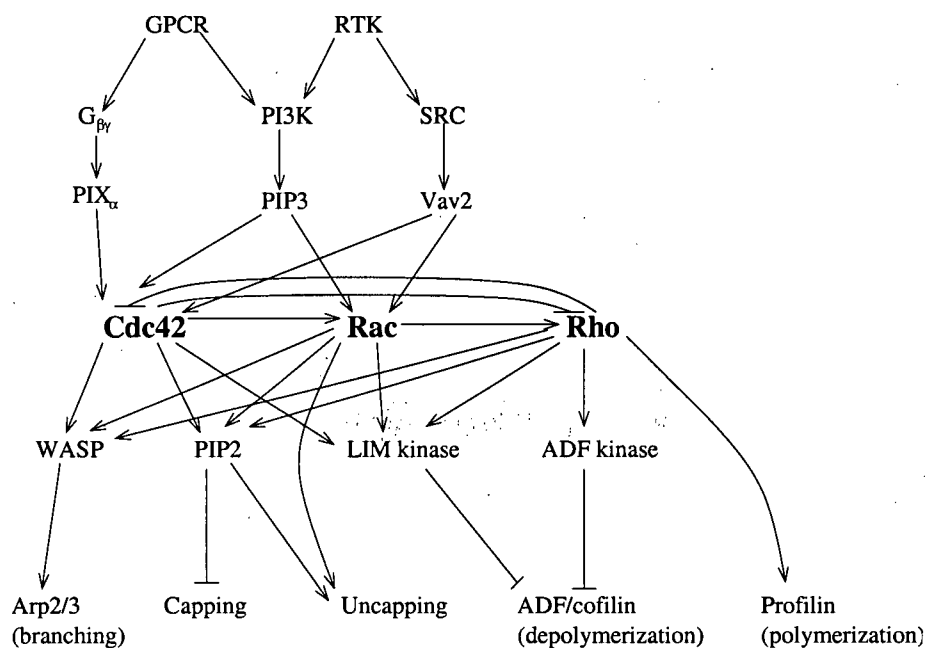


Figure 6.1: General signalling cascade of the Rho-proteins Rho, Rac and Cdc42 showing some upstream activators as well as downstream effects. GPCR=G protein coupled receptor, RTK=receptor tyrosine kinase, $G_{\beta\gamma}=\beta\gamma$ subunit of G protein, PI3K=PI-3 kinase, SRC=steroid receptor coactivator, PIX_{α} =Cdc42 GEF, PIP_3 =phosphoinositide, Vav2=Cd42/Rac GEF.

of only one subunit and have a molecular weight of 20-40 kDa (Takai et al., 2001), distinguishing them from heterotrimeric G proteins which consist of three subunits. All G proteins, including small G proteins, act as molecular switches by cycling between a GTP (guanosine triphosphate, guanosine bound to three phosphates) bound state and a GDP (guanosine diphosphate, the nucleoside guanosine bound to two phosphates) state (see Figure 6.2). GTP-bound small G proteins are considered active since they can interact with downstream effectors while GDP-bound small G proteins are inactive. In the models proposed in this thesis, I assume small G proteins are always in their active form, unless otherwise indicated. Members of the small G protein family have been divided into five subfamilies: Ras family, Rho family, Rab and Sar1/Arf family and the Ran family. I focus on the Rho family of small G proteins.

6.1.2 Rho protein subfamily of small G proteins

Rho (Ras Homologous) proteins were first isolated in 1985 (Madaule and Axel, 1985). The Rho proteins control the growth and organization of the actin cytoskeleton (Mackay and Hall, 1998; Ridley, 2001c), and are crucial for cell motility (Chung et al., 2000; Ridley, 2001a; Wedlich-Soldner et al., 2003), neuronal development (Kuhn et al., 2000; Yamaguchi et al., 2001), and

membrane trafficking (Ridley, 2001b). I focus on the best studied members of the Rho subfamily, Cdc42H, Rac1 and RhoA (referred to hereafter as Cdc42, Rac and Rho). These Rho proteins are expressed by many different cell types such as fibroblasts, neutrophils and neurons.

6.1.3 Polarization and total concentration of the Rho proteins

Cdc42, Rac and Rho contain a hydrophobic region, requiring them to associate with the plasma membrane, unless associated with GDI, a protein that regulates their state (see Section 6.1.4). Since GDI preferentially binds GDP-bound Rho proteins (Fukumoto et al., 1990), GDP-bound Rho proteins are found in the cytoplasm and the membrane while GTP-bound forms are only found on the membrane. In a resting cell, the Rho proteins are evenly distributed. When a cell is stimulated by a spatially graded signal, some members of the Rho protein family polarize by reorganizing into spatially distinct domains with Cdc42 and Rac high at the leading edge and Rho elevated at the rear (Kraynov et al., 2000; Nalbant et al., 2004; Srinivasan et al., 2003; Xu et al., 2003). There are no direct measurements of the concentration of Rho proteins in motile cells. However, experiments with fibroblasts estimated the total weight of Rho proteins in fibroblasts (Michaelson et al., 2001). Using the molecular weight of the Rho proteins and approximating cells as spheres of diameter 10 μm , the baseline concentration of Rho proteins in both the active and inactive form is estimated as $\text{Cdc42}_{\text{total}}=2.4 \mu\text{M}$, $\text{Rac}_{\text{total}}=7.5 \mu\text{M}$, $\text{Rho}_{\text{total}}=3.1 \mu\text{M}$ (see Marée et al. (2006)).

6.1.4 GAPs, GEFs and GDIs regulate Rho protein activation

Cycling between an active and inactive state allows the Rho proteins to act as biological switches. In the absence of regulatory agents, GDP/GTP exchange and GTP hydrolysis are very slow. However, there are three classes of protein that accelerate and regulate the switching of the Rho proteins between the active and inactive state, shown schematically in Figure 6.2.

Rho proteins are activated by GEFs (guanine-nucleotide exchange factors). These proteins associate with a GDP-bound Rho protein, causing GDP to be released. The GEF is then exchanged for GTP and the Rho protein is activated (Schmidt and Hall, 2002; Zheng, 2001). Rho proteins are inactivated by GAPs (GTPase activating protein), proteins that bind to GTP-bound Rho proteins and accelerate GTP hydrolysis (Moon and Zheng, 2003). GDIs, guanine dissociation inhibitors, preferentially associate with GDP-bound Rho proteins (Miura et al., 1993). GDIs prevent GDP from dissociating, keeping the Rho protein in the inactive state.

GDI's also shield the hydrophobic region of the Rho protein, allowing the GDI-Rho protein complex to remain in the cytoplasm.

While GAPs, GEFs and GDI's are not explicitly incorporated into the model discussed here, their activity is reflected in the biochemical rates governing the activation and inactivation of the Rho proteins.

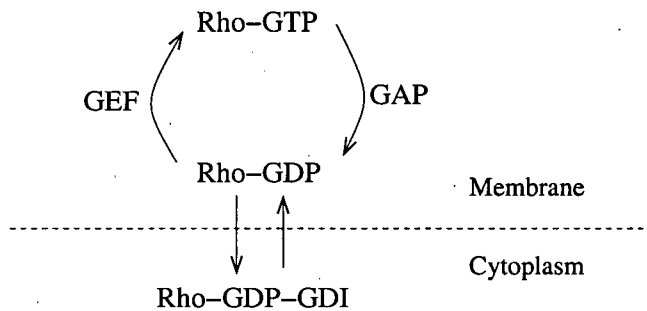


Figure 6.2: Schematic diagram of Rho protein localization and activation cycle, mediated by GEFs, GAPs and GDI's.

6.1.5 Role of Rho proteins in cell motility

Since their discovery, it has been demonstrated that Rho proteins play a crucial role in cell motility by spatially regulating actin polymerization dynamics (Raftopoulou and Hall, 2004). In stimulated cells, Rho proteins are activated by upstream signals such as phosphoinositides, membrane-bound lipids that are discussed further in Chapter 8. Rho proteins influence each other through crosstalk (discussed further in Section 6.1.6) and establish distinct spatial domains with active Cdc42 and Rac high at the leading edge and active Rho elevated at the rear. Under the influence of the Rho proteins, the cytoskeleton is remodelled, changing from a rounded resting cell to a tear drop or crescent shaped cell with a long, flat lamellipodium protruding in the direction of motion.

Each Rho protein has a distinct effect on actin polymerization, discussed below. Experiments designed to investigate the effects of Cdc42, Rac and Rho on motile cells focus on two main cell types, excitable and non-excitable cells. As discussed in Chapter 1, excitable cells, such as neurons and neuron-like cells, extend an actin rich process called a growth cone during development (which will eventually adhere and form an axon) while the cell body remains stationary. Non-excitable cells such as fibroblasts, epithelial cells, keratocytes and neutrophils, extend a lamellipodium at the leading edge while myosin-based contractions at the rear detach

the cell from the substrate, allowing the entire cell to translocate in response to a stimulus. Despite the differences between excitable and non-excitable cells, growth cones and lamellipodia share many structural similarities and regulate actin polymerization using Rho proteins in a similar manner. The next chapter (Chapter 7) explores Rho protein regulation of actin dynamics in more detail. A general signalling cascade involving the Rho proteins is shown in Figure 6.1.

Role of Cdc42

Cdc42, the first Rho protein to be activated in a stimulated cell, is required for proper gradient sensing and stimulates *de novo* actin polymerization by increasing the rate of branching by Arp2/3. Active Cdc42 forms a gradient in motile cells, with high levels at the leading edge, decreasing into the cell (Nalbant et al., 2004; Srinivasan et al., 2003). Cdc42 interacts with WASp or N-WASp, membrane associated proteins, to increase the activation of Arp2/3, causing filament branching and new barbed end formation at the leading edge (Cicchetti et al., 2002; Ridley, 2001c; Schmitz et al., 2000). Cells microinjected with constitutively active Cdc42 form filopodia at the site of injection and initiate movement with the Cdc42-enriched area of the cell forming the leading edge (Bird et al., 2003; Kozma et al., 1995). Cells expressing inactive Cdc42 (Cdc42-GDP) can initiate movement in response to a stimulus but are unable to detect a gradient and move in random directions (Jones et al., 1998). In the models developed in Chapters 7 and 8, I incorporate Cdc42 activation of Arp2/3 and investigate the role Cdc42 plays in gradient sensing and polarization.

Role of Rac

Rac is required for sustained cell movement and, like Cdc42, is important for gradient sensing (Ridley, 2001a). Direct observations indicate that Rac, again like Cdc42, is elevated at the front of migrating cells, decreasing toward the rear (Kraynov et al., 2000; Ridley, 2001a; Wittmann and Waterman-Storer, 2001). Rac is required for the extension of lamellipodia (Burrige, 1999; Matozaki et al., 2000; Nobes and Hall, 1995; Ridley, 2001c; Takai et al., 2001). Rac enhances actin polymerization in motile cells by decreasing the rate of barbed end capping near the leading edge. In Chapter 7, I modify the capping rate in the 1D model of actin dynamics to depend on the concentration of Rac and in Chapter 8, I investigate the role of Rac in sustained cell movement.

Role of Rho

Rho is required for cell adhesion (Burrige, 1999; Mackay and Hall, 1998; Matozaki et al., 2000; Nobes and Hall, 1995; Ridley, 2001c; Takai et al., 2001) and myosin-mediated cell body contraction (Burrige, 1999; Ridley, 2001b). Active Rho has also been visualized in motile cells, where it forms a reciprocal gradient to Cdc42 and Rac with high concentration at the rear and low concentration at the leading edge Raftopoulou and Hall (2004); Wong et al. (2006). This reciprocal gradient is not unexpected since the downstream effects of Rho are antagonistic to those of Cdc42 and Rac and Rho-mediated activities such as cell body contraction occur primarily at the rear of the cell. I do not directly incorporate the effect of Rho on actin dynamics here, but please see Marée et al. (2006) for a model that includes Rho-mediated contraction of a motile cell.

6.1.6 Crosstalk between the Rho proteins

The Rho proteins Cdc42, Rac and Rho not only influence actin polymerization dynamics, they also interact with each other, regulating their activation state. It is thought that this crosstalk is responsible for the establishment and maintenance of Rho protein gradients in motile cells, ensuring that downstream targets of the Rho proteins are activated in appropriate areas of the cell (eg. Arp2/3 activation at the leading edge and cell body contraction at the rear). However, experiments investigating Rho protein crosstalk produce different, and often contradictory, results. Some proposed pathways for Rho protein crosstalk based on experimental evidence are shown in Figure 6.3.

Some components of Rho protein crosstalk have been clearly established. It has been demonstrated in many cell types that Cdc42 activates Rac and Rac activates Rho (Burrige, 1999; Li et al., 2002; Nobes and Hall, 1995). It is less clear how Rho interacts with Cdc42 and/or Rac to produce the spatial segregation seen in motile cells. As shown in Figure 6.3, some experiments indicate that Rho inhibits Rac and Rac inhibits Rho (Li et al., 2002; Mackay and Hall, 1998; Yamaguchi et al., 2001). Recent experiments suggest the most likely pathway involves mutual inhibition of Cdc42 and Rho (Burrige, 1999; Giniger, 2002). Crosstalk between the Rho proteins has been demonstrated by observing downstream effects or the spatial localization of Rho proteins in mutant cells. The mechanism used by the Rho proteins to activate or inhibit each other remains unknown.

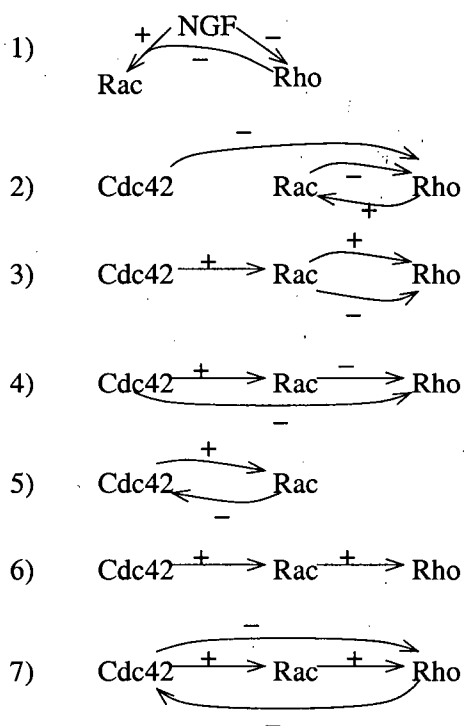


Figure 6.3: Proposed interactions of Rho/Rac/Cdc42 as put forth in 1) Yamaguchi et al. (2001), 2) Li et al. (2002), 3) Mackay and Hall (1998), 4) Burrige (1999), 5) Yasui et al. (2001), 6) Nobes and Hall (1995) and 7) Giniger (2002).

6.1.7 Theoretical models of Rho protein crosstalk

Recent theoretical work has attempted to model Rho protein crosstalk to understand the role of the Rho proteins in motile cells. To date, only two models have been proposed to investigate crosstalk in Rho proteins and both rely on a pathway much like that suggested in Giniger (2002), Figure 6.4, which incorporates mutual inhibition of Cdc42 and Rho as well as the established cascade of Cdc42, Rac and Rho activation.

The first model of Rho protein crosstalk was proposed by Sakumura et al. (2005) to investigate neuronal axon guidance. This model is very similar to that proposed in Giniger (2002) with the addition of autocatalytic activation of Rac. Their model displays two behaviours, oscillatory or steady state, depending on the parameter regime. They believe the extension and retraction of neural growth cones is a result of Rho protein dynamics switching between oscillatory and steady-state behaviours. Monte Carlo simulations of the signalling pathway indicate that neither autocatalytic Rac activation or activation of Rac by Cdc42 is required to produce this switching

behaviour. While this paper provides an interesting analysis of Rho protein crosstalk, there is no connection made to the actin dynamics underlying growth cone extension and retraction.

Another model, also based on the pathway proposed in Giniger (2002), was investigated in our group by Jilkiné (2005) and Marée et al. (2006). This model for Rho protein dynamics is able to produce spatially distinct domains with Cdc42 and Rac elevated at the front and Rho elevated at the rear in response to a spatially graded external stimulus. It was determined that mutual inhibition of Cdc42 and Rho and rapid diffusion of the inactive Rho proteins is required to achieve spatial segregation. I briefly review that model in this chapter, then explore its dynamics when coupled with a model of actin dynamics (Chapter 7) as well as phosphoinositides (upstream effectors of Rho proteins, Chapter 8).

6.2 Observations and questions to address with a theoretical model

Experimental observations have determined that Rho proteins are spatially segregated in motile cells. Here, I review the model developed in Jilkiné (2005) and Marée et al. (2006), based on biologically reasonable assumptions. I report those results here, demonstrating that this model can give rise to the correct spatial localization of Rho proteins observed in motile cells. Please see Jilkiné (2005) and Marée et al. (2006) for a more in depth investigation of the Rho protein model, addressing additional observations and questions.

6.3 Spatial model of Rho protein dynamics

This model is based on Rho protein interactions proposed in Giniger (2002), shown in Figure 6.4, and in more detail in Figure 6.5. It includes the established cascade of Cdc42 activating Rac and Rac activating Rho as well as mutual inhibition of Cdc42 and Rho. It is assumed the Rho proteins affect the activity of the GEFs to enhance or inhibit the activation rate in this crosstalk model. This model keeps track of both the active and inactive forms of Cdc42, Rac and Rho.

6.3.1 Model variables

Experimental measurements of Rho proteins cannot separately quantify the concentration in the cytosol versus the cytoplasm. For this reason, I define an "effective" concentration for these

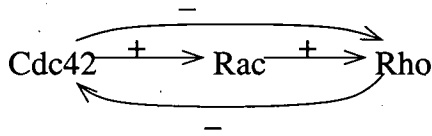


Figure 6.4: Proposed Rho protein crosstalk as presented in Giniger (2002).

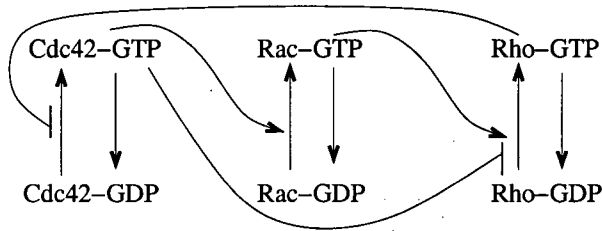


Figure 6.5: Schematic of Rho protein interactions modelled with Equations 6.2. \dashv indicates inhibition while \rightarrow indicates activation.

variables in vertical slice of the cell. I assume a constant thickness (as shown in Figure 6.6) and ignore the bulge of the nuclear region. The variables G and G_i are then given in μM for the appropriate number of molecules per unit volume in such a slice.

- C Concentration of active Cdc42, μM
- C_i Concentration of inactive Cdc42, μM
- R Concentration of active Rac, μM
- R_i Concentration of inactive Rac, μM
- ρ Concentration of active Rho, μM
- ρ_i Concentration of inactive Rho, μM
- x Spatial coordinate
- t Time coordinate

6.3.2 Model assumptions

The following assumptions were made in constructing this model:

1. Cdc42 enhances the activation of Rac and Rac enhances the activation of Rho.
2. Mutual inhibition of Rho and Cdc42 is achieved by inhibiting the activation rate.
3. Rho proteins are not made or degraded but only converted between active and inactive states.

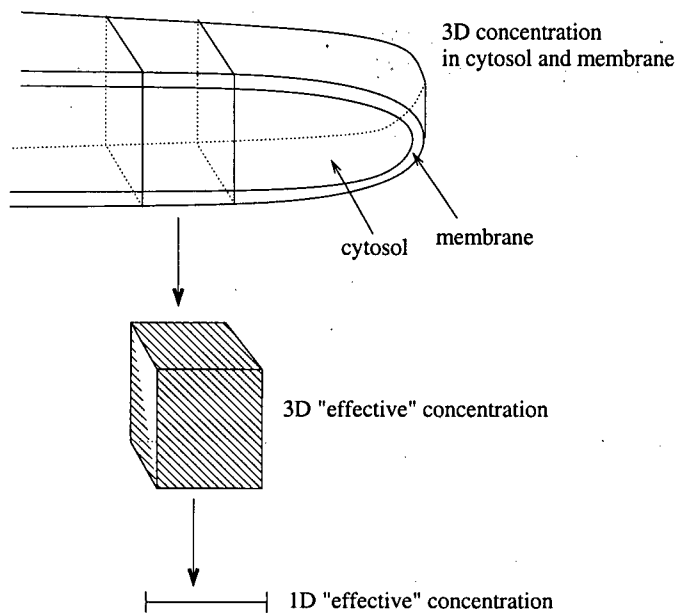


Figure 6.6: "Effective" Rho protein concentration combines concentrations in both membrane and cytoplasm.

4. Active Rho proteins are found only on the membrane, where they diffuse at a relatively slow rate (see Assumption 5).
5. Inactive Rho proteins are found both on the membrane and in the cytoplasm and diffuse at a higher rate than the active membrane-bound forms.
6. Rho proteins affect activation dynamics at a rate that increases proportionally to their increase in concentration from a baseline value.

6.3.3 Model equations

General Rho protein equation in the absence of crosstalk

In this model, a general Rho protein, G , is activated from the inactive form, G_i , at a baseline rate, I_G . Activation is assumed to depend linearly on G_i/G_{tot} which is the ratio of the inactive form to the total concentration of the Rho protein, G_{tot} , which is assumed to be constant (see Assumption 3). In experiments it is possible to measure the relative but not absolute levels of inactive and active forms of the Rho proteins (although the total amounts are known from other sources). For this reason, I use the scaled form, G_i/G_{tot} , in this model. The conversion from the active to the inactive form is assumed to occur at a rate proportional to the active form, with rate d_G . According to Assumptions 5 and 4, the active form diffuses at the rate D_m while

the inactive form diffuses at a different rate D_{mc} where $D_m < D_{mc}$. Since Cdc42, Rac and Rho have approximately the same molecular weight, it is assumed that D_m is the diffusion rate for all active forms and D_{mc} is the diffusion rate for all inactive forms.

As discussed in Chapter 3 regarding Arp2/3, cytoplasmic proteins advect at the rate v_{bulk} which can range from zero (where the proteins are immobilized due to binding to the actin meshwork or other stationary cell structures) to the speed of membrane protrusion (where the proteins are pulled forward with the cytoplasm as the membrane moves). As with Arp2/3, I assume that $v_{bulk} = x'_{edge}$ so that inactive Rho proteins, which are found mainly in the cytoplasm, are pulled forward by the motion of the membrane.

The active Rho proteins are found only on the membrane, and experimental evidence suggests they also advect as the cell moves. Experiments that photobleached areas of the membrane or that attached gold beads to the membrane of moving keratocytes found that there is no bulk membrane flow in motile keratocytes and the gold beads maintained an approximately constant distance from the leading edge (Kucik et al., 1990). This suggests that membrane-bound proteins and lipids experience an advective flow at the speed of membrane protrusion, x'_{edge} .

This leads to the following PDE describing the dynamics of a general active and inactive Rho proteins in the absence of crosstalk:

$$\frac{\partial G}{\partial t} = I_G \frac{G_i}{G_{tot}} - d_G G + x'_{edge} \frac{\partial G}{\partial x} + D_m \frac{\partial^2 G}{\partial x^2}, \quad (6.1a)$$

$$\frac{\partial G_i}{\partial t} = -I_G \frac{G_i}{G_{tot}} + d_G G + x'_{edge} \frac{\partial G_i}{\partial x} + D_{mc} \frac{\partial^2 G_i}{\partial x^2}. \quad (6.1b)$$

General Rho protein crosstalk terms

To model crosstalk of the Rho proteins, it is assumed in this model that crosstalk is mediated by GEFs, based on evidence presented in Burrige and Wennerberg (2004). By interacting with the GEFs, a Rho protein G' can enhance or inhibit the activation rate of the Rho protein G .

To model enhanced activation of G , the Rho protein G' increases the rate of G activation proportionally to the concentration of G' with rate α . The activation term in Equation 6.1a then becomes:

$$(I_G + \alpha G') \frac{G_i}{G_{tot}}.$$

To model inhibition of G by G' , I use a saturating sigmoidal function as appeared, for example, in the toggle switch model developed by Gardner et al. (2000). The toggle switch

model relies on a sigmoidal term of the form

$$1 - \frac{G'^n}{\beta_{G'}^n + G'^n} = \frac{\beta_{G'}^n}{\beta_{G'}^n + G'^n}$$

which is highest when $G' = 0$ and decreases as G' increases. In the Rho protein model, this toggle switch is incorporated into the activation term to model G' inhibition of G activation:

$$I_G \frac{G_i}{G_{tot}} \left(\frac{\beta_{G'}^n}{\beta_{G'}^n + G'^n} \right) = \frac{I_G G_i / G_{tot}}{1 + (G' / \beta_{G'})^n}.$$

In Jilkiné (2005); Marée et al. (2006), it was determined that the Hill coefficient n must be greater than 1 to achieve spatially asymmetric profiles, suggesting G' acts cooperatively to inhibit the activation of G .

Cdc42, Rac and Rho equations

Based on the general equations discussed above, the Rho protein equations are:

$$\frac{\partial C}{\partial t} = \frac{I_c C_i / C_{tot}}{(1 + (\rho/a_1)^n)} - d_c C + x'_{edge} \frac{\partial C}{\partial x} + D_m \frac{\partial^2 C}{\partial x^2}, \quad (6.2a)$$

$$\frac{\partial C_i}{\partial t} = -\frac{I_c C_i / C_{tot}}{(1 + (\rho/a_1)^n)} + d_c C + x'_{edge} \frac{\partial C_i}{\partial x} + D_{mc} \frac{\partial^2 C_i}{\partial x^2}, \quad (6.2b)$$

$$\frac{\partial R}{\partial t} = (I_r + \alpha C)(R_i / R_{tot}) - d_r R + x'_{edge} \frac{\partial R}{\partial x} + D_m \frac{\partial^2 R}{\partial x^2}, \quad (6.2c)$$

$$\frac{\partial R_i}{\partial t} = -(I_r + \alpha C)(R_i / R_{tot}) + d_r R + x'_{edge} \frac{\partial R_i}{\partial x} + D_{mc} \frac{\partial^2 R_i}{\partial x^2}, \quad (6.2d)$$

$$\frac{\partial \rho}{\partial t} = \frac{(I_p + \beta R)(\rho_i / P_{tot})}{1 + (C/a_2)^n} - d_p \rho + x'_{edge} \frac{\partial \rho}{\partial x} + D_m \frac{\partial^2 \rho}{\partial x^2}, \quad (6.2e)$$

$$\frac{\partial \rho_i}{\partial t} = -\frac{(I_p + \beta R)(\rho_i / P_{tot})}{1 + (C/a_2)^n} + d_p \rho + x'_{edge} \frac{\partial \rho_i}{\partial x} + D_{mc} \frac{\partial^2 \rho_i}{\partial x^2}, \quad (6.2f)$$

where I_c , I_r , I_p are the baseline activation rates and d_c , d_r , d_p are the baseline inactivation rate of Cdc42, Rac and Rho, respectively. The Cdc42 activation rate, I_c , is varied spatially and temporally to simulate the effect of an external signal. In Chapter 8, I incorporate PIs which directly affect the activation rates of Cdc42 and Rac (I_c and I_r). C_{tot} , R_{tot} , P_{tot} are the total concentrations of Cdc42, Rac and Rho. a_1 and a_2 are the Rho and Cdc42 concentrations that elicit a half-maximal inhibition of Cdc42 and Rho activation, respectively. α determines the rate of Cdc42-enhanced activation of Rac and β determines the rate of Rac-enhanced Rho activation. D_m and D_{mc} are the diffusion rates of the active and inactive forms.

No-flux boundary conditions are imposed in both the active and inactive forms to prevent

the Rho proteins from diffusing past the membrane:

$$\left. \frac{\partial G}{\partial x} \right|_{x=x_{edge}, x_{edge}-L} = 0$$

where x_{edge} is the membrane position and L is the length of the cell. Parameter values used to simulate the Rho protein equations are discussed in the next Section and compiled in Table 6.1.

6.4 Parameter values

The parameter values used to simulate Equations (6.2), taken from Marée et al. (2006) and Jilkiné (2005), and are compiled in Table 6.1. The diffusion rate of Rho proteins in the membrane and cytoplasm, were based on estimates of diffusion coefficients of G proteins (members of the superfamily that contains small G proteins) that were reported to be $0.1 \mu\text{m}^2/\text{s}$ on the membrane and $10\text{-}50 \mu\text{m}^2/\text{s}$ in the cytoplasm (Postma and Van Haastert, 2001; Postma et al., 2004). For these simulations, it is assumed the Rho proteins have similar diffusion coefficients. Experimental data of the decay of Rac (Sako et al., 2000) and Rho (Zhang and Zheng, 1998) was used to determine the decay rate of active Rho proteins, giving approximately $d_G = 1 \text{ s}^{-1}$. These decay rates, along with the steady state concentrations of each Rho protein discussed in Section 6.1.3 were used to determine approximate activation rates. It is estimated that the basal activation rates for Cdc42, Rac and Rho are approximately $I_c = 3.4$, $I_R = 0.5$ and $I_\rho = 3.3 \mu\text{M}\text{s}^{-1}$. The half maximal concentrations of the Rho proteins used in the toggle switch inhibition terms (a_1 and a_2) were assumed to be in the same range as their steady state concentrations. The Hill coefficient n was chosen sufficiently large to ensure that the ODE version of the equations (in the absence of diffusion) leads to the coexistence of two stable steady states.

6.5 Simulations

This model (Equations 6.2) and variants of it, were explored in Jilkiné (2005). That work investigated polarization of a Cdc42, Rac and Rho module in a resting 1D domain (not a moving cell). The domains considered were 1D cell transects, as shown in Figure 1.8 as well as the perimeter of the cell (a 1D domain with periodic boundary conditions). In preparation for combining this model of Rho proteins with a model of actin dynamics explored in Chapters 3-5, I investigated this model numerically using my own C code, on a 1D domain representing a transect of a lamellipodium, as shown in Figure 1.8. I assumed the cell was at rest, making

Parameter	meaning	value	source
C_b	typical level of active Cdc42	1 μM	[1], [2]
R_b	typical level of active Rac	3 μM	[1], [2]
ρ_b	typical level of active Rho	1.25 μM	[1], [2]
C_{tot}	total level of Cdc42	2.4 μM	[1], [2], [3]
R_{tot}	total level of Rac	7.5 μM	[1], [2], [3]
P_{tot}	total level of Rho	3.1 μM	[1], [2], [3]
I_C	Cdc42 activation rate	3.4 $\mu\text{M s}^{-1}$	[1], [2]
I_R	Rac activation rate	0.5 $\mu\text{M s}^{-1}$	[1], [2]
I_p	Rho activation rate	3.3 $\mu\text{M s}^{-1}$	[1], [2]
a_1	Rho level for half-max inhibition of Cdc42	1.25 μM	[1], [2]
a_2	Cdc42 level for half-max inhibition of Rho	1 μM	[1], [2]
n	Hill coefficient of Cdc42-Rho mutual inhibition response	3	[1], [2]
α	Cdc42-dependent Rac activation rate	4.5 s^{-1}	[1], [2]
β	Rac-dependent Rho activation rate	0.3 s^{-1}	[1], [2]
d_C, d_R, d_p	decay rates of activated Rho-proteins	1 s^{-1}	[4], [5]
D_m	diffusion coefficient of active Rho-proteins	0.1 $\mu\text{m}^2 \text{s}^{-1}$	[6], [7]
D_{mc}	diffusion coefficient of inactive Rho-proteins	10 $\mu\text{m}^2 \text{s}^{-1}$	[6], [7]

Table 6.1: Parameter estimates relevant to the Rho-proteins and their interactions. Cited sources: [1]: Jilkiné (2005), [2]: Marée et al. (2006), [3]: Michaelson et al. (2001), [4]: Sako et al. (2000), [5]: Zhang and Zheng (1998), [6]: Postma and Van Haastert (2001), [7]: Postma et al. (2004).

$x'_{edge} = 0$. Equations (6.2) were simulated on a 10 μm grid with a step size of $\Delta x = 0.01$ μm . The time step was chosen according to the fastest diffusion rate to ensure numerical stability. Diffusion terms were discretized using centered differencing and time derivatives were discretized using Forward Euler. Initial conditions, unless otherwise indicated, of the active Rho proteins were set to their steady state concentrations ($G = G_b$ where G is Cdc42, Rac or Rho) and the inactive forms were set to the total level minus the concentration of the active forms ($G_i = G_{tot} - G$). The simulations were halted at 200 s, after a steady state distribution had been established. By ensuring that my independent simulations gave the same results as in Jilkiné (2005); Marée et al. (2006), I could verify that this aspect of my code was working properly before connecting the Rho protein module to actin dynamics (Chapter 7) or a model of phosphoinositides (Chapter 8).

6.6 Results

6.6.1 Small G proteins establish stable spatial domains in response to a spatially graded input to Cdc42

To determine the response of this model to an external graded stimulus, a gradient was imposed in the activation rate of Cdc42, I_c . The stimulus was applied for one second, during which the activation rate I_c increased linearly from zero at the left boundary of the domain to its usual value at the right boundary, given in Table 6.1. At all other times, I_c had a constant value everywhere on the domain. As shown in Figure 6.7, Cdc42, Rac and Rho establish stable asymmetric spatial profiles in response to a graded initial distribution of active Cdc42. These asymmetric spatial domains are consistent with experimental observations, with Cdc42 and Rac high at the front and Rho high at the rear, consistent with the results in Jilkiné (2005); Marée et al. (2006).

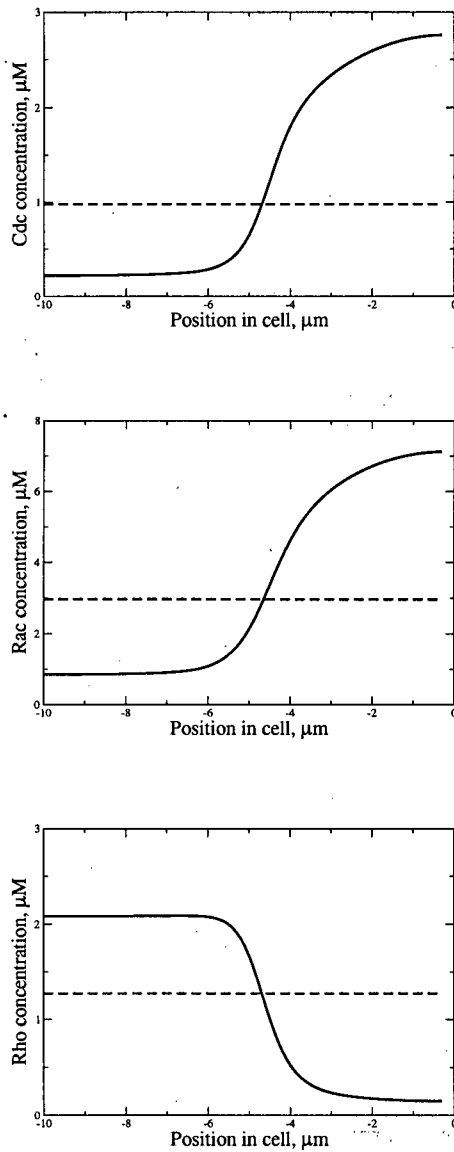


Figure 6.7: Active Cdc42 (top), Rac (middle) and Rho (bottom) establish stable asymmetric spatial profiles in response to a graded transient gradient in the activation rate of Cdc42, consistent with experimental observations. The spatial profiles are shown before (dotted line) and after (solid line) application of the stimulus.

6.6.2 Small G proteins establish stable spatial domains in response to a random input to Cdc42

To determine the response of this model to a random stimulus, the activation rate of Cdc42, I_c , was assigned a random value at each grid point with values ranging from zero to twice the usual activation rate. The random stimulus was applied for one second, after which the activation rate of Cdc42 was returned to its usual value everywhere on the domain. Figure 6.8 shows the spatial profile of Cdc42, Rac and Rho before, during and after the application of the stimulus. As shown, a random stimulus leads to spatially asymmetric domains but there is no defined front or back along the length of the cell. This demonstrates that this model can establish stable asymmetric spatial domains in response to a random stimulus but the spatial profiles can have more than one area with high concentrations of Cdc42 and Rac. These multiple domains of high Cdc42 are not observed in motile cells, suggesting that the Rho proteins are regulated by other upstream factors that prevent these multiple domains from forming.

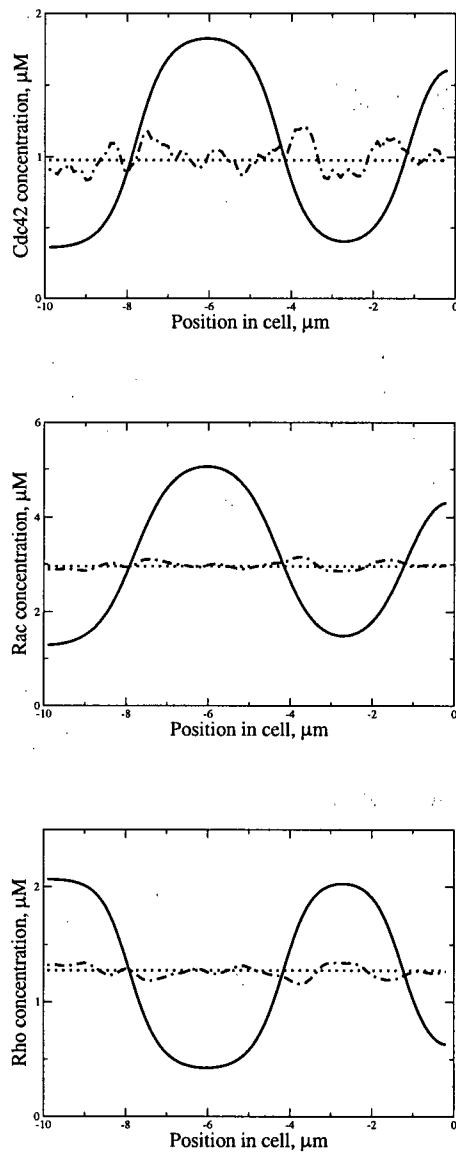


Figure 6.8: Active Cdc42, Rac and Rho establish stable spatial profiles with multiple domains with high Cdc42 and Rac in response to a random activation of Cdc42. As in Figure 6.7 but showing changes in response to a transient random change in the activation rate of Cdc42. The spatial profiles are shown before (dotted line), during (dot-dash line) and after (solid line) application of the stimulus.

6.6.3 Rho proteins establish domains on both sides of the cell in response to two stimuli

It has been shown in immobilized cells that two stimuli placed on opposite sides of the cell will produce two domains with high Cdc42 and Rac at both the front and the back, with high Rho in the middle (Janetopoulos et al., 2004). I simulate this experiment by increasing the activation of Cdc42 at the front and back of the domain and decreasing it in the middle. The activation rates of Rac and Rho are unchanged. The stimulus is applied for one second after which the activation rate is returned to its baseline value everywhere on the domain. As shown in Figure 6.9, this model establishes separate stable domains of Cdc42 and Rac at both the front and back of the model cell with Rho high in the middle of the cell, consistent with the experimental observations.

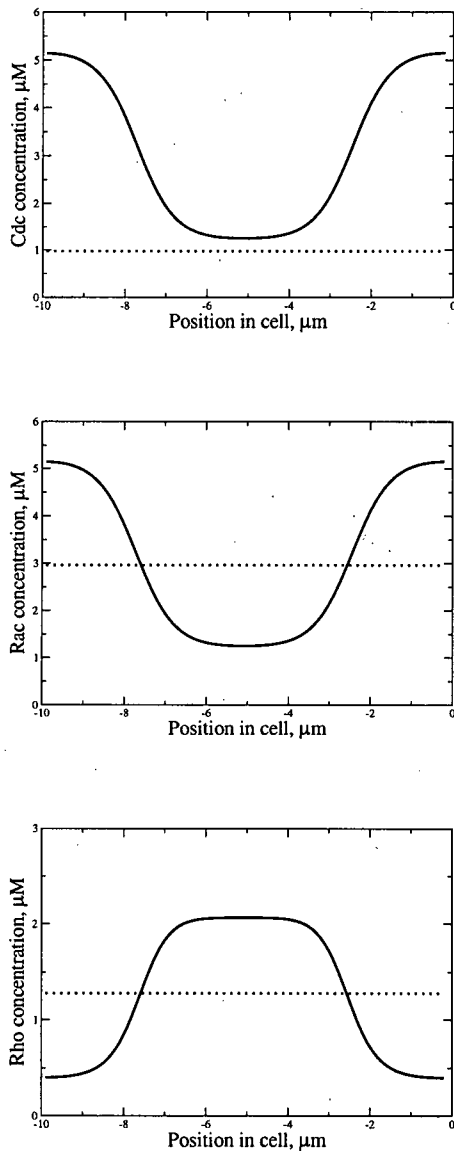


Figure 6.9: As in Figure 6.7 but showing spatial profiles in response to a transient stimulus that decreases Cdc42 activation in the middle of the domain, simulating two chemoattractant sources placed on opposite sides of the cell. The Rho proteins are able to establish stable profiles with active Cdc42 and Rac elevated at the front and back of the cell and active Rho elevated in middle. The spatial profiles are shown before (dotted line) and after (solid line) application of the random stimulus.

6.7 Discussion

There is some controversy about how the Rho proteins influence each other and it is not yet entirely clear what mechanisms the Rho proteins may be using to affect each other's activation. However, a model based on reasonable biological assumptions of Rho protein regulation leads to spatial profiles that are consistent with experimental observations. In particular, mutual inhibition of Cdc42 and Rho is required to establish distinct spatial domains that are characteristic of motile cells. When subjected to a graded stimulus, corresponding to a gradient of chemoattractant, the Rho proteins respond by establishing stable, spatially asymmetric domains with Cdc42 and Rac elevated at the front and Rho elevated at the rear, consistent with experimental observations. The Rho proteins also establish stable asymmetric domains in response to a random stimulus. In that case, the cell can establish more than one domain where Cdc42 and Rac are high and Rho is low. This suggests that Rho proteins alone will not always properly polarize a cell but this is corrected in Chapter 8 when I add phosphoinositide regulation of Rho protein activation.

By simulating this preexisting model for Cdc42, Rac and Rho, I am able to link it to my model of actin dynamics (Chapter 7) as well as to further upstream signalling events (Chapter 8). In the next chapter, I explore how this model of Rho proteins can influence actin dynamics in a 1D model of a motile cell.

Chapter 7

Regulation of actin polymerization by Rho proteins in a 1D model cell

In the previous chapter, I reviewed a model of Rho protein crosstalk that responds to a graded stimulus by establishing stable asymmetric spatial profiles. In this chapter, I discuss which aspects of actin dynamics are regulated by Rho proteins and incorporate that information into a variant of the actin model investigated in Chapters 3-5. By combining the models for Rho proteins and actin dynamics, I am able to explore how spatial segregation of the Rho proteins in response to an external signal can lead to enhanced actin polymerization at the leading edge of a cell and initiation of directed motion.

7.1 Regulation of actin polymerization by Rho proteins

Rho proteins in their active form impinge on cytoskeletal processes. Figure 7.1 summarizes the result of experimental data suggesting specific pathways through which the Rho proteins affect actin dynamics.

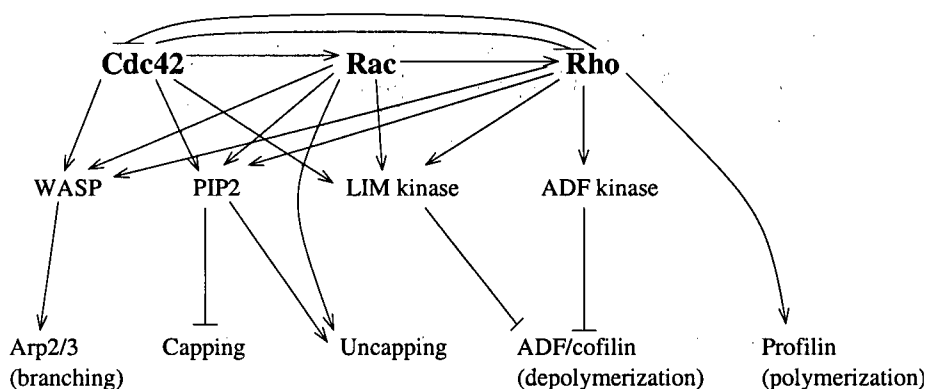


Figure 7.1: Schematic diagram of Rho protein signalling to the actin cytoskeleton. \dashv indicates inhibition while \rightarrow represents enhanced activation. Not all these interactions are direct and may occur through other downstream effectors or signalling molecules.

7.1.1 Cdc42 enhances nucleation by Arp2/3

Cdc42 greatly enhances the activation rate of Arp2/3, increasing the branching rate. As discussed in Chapter 2, the protein complex Arp2/3 creates new barbed ends at the leading edge of motile cells by nucleating new branches off existing filaments. Arp2/3 is activated by membrane-associated members of WASp/SCAR family such as WASp or N-WASp. In the presence of active Cdc42, WASp activation of Arp2/3 is increased two-fold (Cicchetti et al., 2002; Ridley, 2001a; Schmitz et al., 2000). Rac and Rho enhance nucleation by Arp2/3 by enhancing activation of WASP (Cicchetti et al., 2002; Ridley, 2001a), but to a lesser extent than Cdc42. In this model, I replace the constant membrane source of Arp2/3, shown in Equations (3.2) with source terms everywhere on the domain that rely on the local concentration of Cdc42 and Rac (see upcoming Equations (7.1)).

7.1.2 Rac inhibits capping of barbed ends

Rac plays an important role in keeping barbed ends free for polymerization by inhibiting the activity of capping proteins. Capping proteins and gelsolin bind tightly to filament tips, preventing further polymerization activity. In resting cells, most barbed ends are capped and in motile cells, capping is used to regulate the number of polymerizing barbed ends. Too many polymerizing barbed ends at the leading edge of a motile cell will quickly deplete the pool of available monomers while too few will not generate sufficient force for membrane protrusion. The effect of Rac on capping is indirect, as active Rac enhances accumulation of the phosphoinositide PIP_2 (discussed further in Chapter 8). PIP_2 disrupts binding of capping protein to filament tips, and dissociates capping protein from filament tips (Cicchetti et al., 2002; Ridley, 2001a). Since I do not keep track of capped filaments, I only model the inhibition of capping in the presence of active Rac (this chapter) or PIP_2 (Chapter 9) in the models presented here.

7.2 Observations and questions to address with a model

Using Equations (3.2), I demonstrated in Chapter 4 that a model of actin dynamics establishes distinct spatial profiles in motile cells with most free barbed ends and active Arp2/3 located very close to the leading edge while the filament density increases more slowly away from the leading edge, gradually decaying toward the rear of the lamellipodium. Experimental evidence discussed in Chapter 6 indicated that Cdc42 and Rac are elevated at the front of motile cells while Rho

is elevated in the rear. In this chapter, I integrate a variant of the actin model developed in Chapter 3 with the Rho protein model reviewed in Chapter 6 to address the following questions:

1. Can a cell initiate directed movement in response to a graded stimulus in the Rho proteins?
2. Are the resulting profiles of barbed ends, Arp2/3 and filament density in agreement with experimental observations?

7.3 Integrated model of Rho proteins and actin dynamics

7.3.1 Additional assumptions

Based on the above discussion, Rho proteins are incorporated into the model of actin dynamics to explore actin dynamics in response to a stimulus to Cdc42. In addition to the modelling assumptions listed in Chapter 3 for the actin model and Chapter 6 for the Rho protein model, the following assumptions were made when combining the actin and Rho protein modules:

1. Arp2/3 nucleates new barbed ends only through side branching.
2. Side branching is modelled as a saturating process depending on both filament density and active Arp2/3, preventing unlimited creation of new barbed ends.
3. Activation of Arp2/3 depends on the concentration of Cdc42 and Rac.
4. Capping is inhibited by Rac.
5. Active and inactive forms of the Rho proteins are pulled forward in the bulk flow created by protrusion of the leading edge.

Since the actin model assumes all barbed ends are oriented toward the leading edge, a threshold term is added to prevent activation of Arp2/3 in a resting cell when Cdc42 and Rac are at or below their baseline concentrations. Otherwise, even a small amount of active Arp2/3 would lead to new barbed end creation, resulting in a slow but non-zero membrane speed.

7.3.2 Model equations

As before, the model variables are:

$B(x, t)$	Density of actively growing barbed ends, $\#/\mu\text{m}$
$F(x, t)$	Filament length density, $\mu\text{m}/\mu\text{m}$
$A(x, t)$	Arp2/3 concentration, μM
$C(x, t)$	Concentration of active Cdc42, μM
$C_i(x, t)$	Concentration of inactive Cdc42, μM
$R(x, t)$	Concentration of active Rac, μM
$R_i(x, t)$	Concentration of inactive Rac, μM
$\rho(x, t)$	Concentration of active Rho, μM
$\rho_i(x, t)$	Concentration of inactive Rho, μM

The equations for actin dynamics are used here are a combination of Equations (3.2) and those proposed in Marée et al. (2006).

Side branching by Arp2/3

Based on the results of Chapter 4, I consider new tip formation to occur only through side branching. I modify the nucleation term to depend sigmoidally on both the concentration of Arp2/3 and the amount of F-actin, according to Assumption 2:

$$\bar{\eta}(A, F) = \frac{\eta AF}{K_m + A + lF},$$

where η is the side branching rate of Arp2/3, K_m is the saturation constant for side branching and l is a conversion factor that relates the units of F to the units of A . The spatial profiles produced using this branching term are qualitatively similar to those produced using Equations (3.2). This branching term prevents unlimited barbed end creation when Arp2/3 concentration or filament density is very high. The conversion factor l , derived in Appendix B, is the concentration of Arp2/3 that binds to $1 \mu\text{m}/\mu\text{m}$ of F-actin.

Inhibition of capping by Rac

As discussed above and stated in Assumption 4, the capping rate is decreased in areas with high concentrations of Rac. I use the following equation to describe the capping rate as a function

of Rac concentration:

$$\kappa(R) = k_{max} - k_R \frac{R}{R_b + R}.$$

In the absence of Rac, capping occurs at the rate k_{max} and decreases to $k_{max} - k_R$ as Rac increases. The capping rate is always positive so $k_R \ll k_{max}$.

Cdc42 and Rac activation of Arp2/3

Instead of a constant source of Arp2/3 at the membrane, as in Equation (3.3), Arp2/3 is now activated everywhere in the cell and depends on the local concentration of Cdc42 and Rac. In order to prevent activation of Arp2/3 when Cdc42 and Rac are at their baseline concentrations, I include a sigmoidal term that is very small when the concentration of Cdc42 and Rac is low. The Hill coefficient in the sigmoidal function is chosen to be large to act as a switch: when the concentration of Cdc42 or Rac exceeds C_{half} or R_{half} , the activation of Arp2/3 proceeds at its maximum rate. This ensures that low concentrations of Cdc42 and Rac do not lead to Arp2/3 activation but a sufficiently large increase in their concentrations (as determined by the parameters C_{half} and R_{half}), will lead to Arp2/3 activation. The activation of Arp2/3 is determined as follows:

$$\text{Arp2/3 activation} = \mu_c C \frac{C^{n_c}}{C_{half}^{n_c} + C^{n_c}} + \mu_r R \frac{R^{n_r}}{R_{half}^{n_r} + R^{n_r}},$$

where $\mu_{c,r}$ are the activation rates of Arp2/3 by Cdc42 and Rac and $n_{c,r}$ are the Hill coefficients in the sigmoidal switching term.

Modified actin equations

Based on the above modifications, the equations for the actin dynamics are:

$$\frac{\partial B}{\partial t} = \bar{\eta}(A, F) - \kappa(R)B - v \frac{\partial B}{\partial x}, \quad (7.1)$$

$$\begin{aligned} \frac{\partial A}{\partial t} &= \mu_c C \frac{C^{n_c}}{C_{half}^{n_c} + C^{n_c}} + \mu_r R \frac{R^{n_r}}{R_{half}^{n_r} + R^{n_r}} - \bar{\eta}(A, F) - d_a A \\ &\quad + D_A \frac{\partial^2 A}{\partial x^2} - x'_{edge} \frac{\partial A}{\partial x}, \end{aligned} \quad (7.2)$$

$$\frac{\partial F}{\partial t} = Bv - F\gamma. \quad (7.3)$$

The boundary condition for barbed ends is given by Equation (3.3) and I impose no-flux

boundary conditions on Arp2/3:

$$\left. \frac{\partial A}{\partial x} \right|_{x=x_{edge}, x_{edge}-L} = 0$$

where, as before, x_{edge} is the membrane position and L is the length of the lamellipodium.

Rho protein equations

Equations (6.2) are used for the Rho proteins:

$$\frac{\partial C}{\partial t} = \frac{I_c C_i / C_{tot}}{2(1 + (\rho/a_1)^n)} - d_c C - x'_{edge} \frac{\partial C}{\partial x} + D_m \frac{\partial^2 C}{\partial x^2}, \quad (7.4)$$

$$\frac{\partial R}{\partial t} = (I_r + \alpha C)(R_i / R_{tot}) - d_r R - x'_{edge} \frac{\partial R}{\partial x} + D_m \frac{\partial^2 R}{\partial x^2}, \quad (7.5)$$

$$\frac{\partial \rho}{\partial t} = \frac{(I_p + \beta R)(\rho_i / P_{tot})}{1 + (C/a_2)^n} - d_p \rho - x'_{edge} \frac{\partial \rho}{\partial x} + D_m \frac{\partial^2 \rho}{\partial x^2}. \quad (7.6)$$

The equations for the inactive forms C_i , R_i and ρ_i are the same as the active forms with reversed signs on the activation and inactivation terms and with faster diffusion, as discussed in Chapter 6.

7.4 Parameters

Most parameters used in simulating Equations (7.1) and (7.4) are given in Tables 4.1 and 6.1. Additional parameters are taken from Marée et al. (2006) and are compiled in Table 7.1. To properly relate the concentration of Arp2/3 and the Rho proteins to the number of barbed ends and the filament density, two conversion factors are derived in Marée et al. (2006), which determine the equivalent "concentration" of barbed ends and filament density based on the typical density of barbed ends and filaments and the number of monomers in a specified length of filament.

7.5 Simulations

I extended my C code, used in Chapters 4 and 6 to simulate Equations (7.1) and (6.2). As described in Chapter 4, the actin equations (Equations (7.1)) are transformed to moving coordinates with variable membrane speed ($\tau = t$, $z = x - x'_{edge} t$). The equations are still PDEs in space and time but the membrane is stationary and located at the origin. The Rho protein equations (7.4) are also transformed into moving coordinates. As before, second derivatives in both sets of equations are discretized using centered differencing while first derivatives are discretized

Parameter	meaning	value	source
μ_C, μ_R	Cdc42 and Rac-dependent Arp2/3 activation	0.16 s^{-1}	[1]
d_A	activated Arp2/3 decay rate	0.1 s^{-1}	[1]
D_A	diffusion coefficient of Arp2/3	$1 \mu\text{m}^2 \text{ s}^{-1}$	[2]
η	Arp2/3 nucleation rate	$60 \mu\text{M nm s}^{-1}$	[2]
K_m	saturation constant for Arp2/3 nucleation	$2 \mu\text{M}$	[1]
l	scale factor converting units of F to concentration	$0.255 \mu\text{M}$	[1]
k	scale factor converting concentration to units of B	$106 \mu\text{m}^{-2} \mu\text{M}^{-1}$	[1]
v	actin filament growth rate (free polymerization)	$0.5 \mu\text{m s}^{-1}$	[3], [4]
d_F	actin filament turnover rate	0.03 s^{-1}	[5], [6]
κ_{max}	barbed end capping rate	2.8 s^{-1}	[4], [7]
κ_R	max reduction of capping by Rac	2.1 s^{-1}	[1]
K_R	Rac level for half-max reduction of capping	$3 \mu\text{M}$	[1]
C_{half}	Active Cdc level for half-max enhancement of Arp2/3 activation	$1.5 \mu\text{M}$	[1]
R_{half}	Active Rac level for half-max enhancement of Arp2/3 activation	$4.5 \mu\text{M}$	[1]
n_c, n_r	Hill coefficient of Cdc42/Rac enhancement of Arp2/3 activation	5	[1]

Table 7.1: Parameter estimates relevant to actin dynamics when coupled with a model of Rho proteins. Cited sources: [1]: Marée et al. (2006), [2]: estimated in text, [3]: Sanger et al. (1996), [4]: Pollard et al. (2000), [5]: Mogilner and Edelstein-Keshet (2002), [6]: Pollard and Borisov (2003), [7]: Schafer et al. (1996).

using Forward Euler. The equations are simulated on a $10 \mu\text{m}$ grid with a step size of $0.01 \mu\text{m}$. The time step is chosen according to the fastest diffusion rate to ensure numerical stability. For initial conditions, Rho proteins are set to their baseline concentrations. The steady state values of barbed ends, Arp2/3 and filament density are determined by running the simulations in the absence of a stimulus for 200 s, ensuring they had reached a steady state distribution. The distribution of barbed ends and filament density is homogeneous almost everywhere on the domain, except at the left boundary where it decreases to zero to satisfy the boundary condition $B(-\infty) = 0$. At steady state, Arp2/3 has a constant concentration everywhere on the domain. The steady state distributions are shown in Figure 9.5. These steady state distributions are used as the initial conditions for the variables B , A and F . Simulations are run for 200 s, allowing all variables to reach steady state.

Here I investigate the model in a 1D domain corresponding to the transect of a lamellipod, as shown in Figure 1.8. However, a model of Rho protein and actin dynamics was investigated in a 2D model cell in Marée et al. (2006). In that paper, the equations were implemented in a 2D domain and membrane movement was determined using a Cellular Potts model (Ouchi et al.,

2003). Marée et al. (2006) explore cell polarization, initiation and maintenance of movement as well as turning behaviour when the stimulus location is changed. In this chapter, I explore cell polarization in the 1D domain and initiation and persistence of movement in response to a stimulus. I simulate the effect of a chemoattractant gradient by imposing a gradient in the activation rate of Cdc42, I_c .

7.6 Results

7.6.1 1D cell model can initiate and maintain directed movement in response to a graded stimulus

To determine the response of the Rho proteins and actin dynamics to a transient graded stimulus, a gradient in the Cdc42 activation rate, I_c , was imposed. In Figures 7.2 and 7.3, the gradient in I_c increased linearly from zero at the left boundary to its usual value at the right boundary. The gradient was applied for one second, 20 seconds after the start of the simulations. At all other times, I_c had its usual value everywhere on the domain. The Rho proteins establish spatial profiles shown in Figure 6.7 while barbed ends, Arp2/3 and filament density establish spatial profiles shown in Figure 7.2.

As discussed in Section 6.6.1, the spatial profiles of the Rho proteins are consistent with experimental observations. Comparing the barbed end, Arp2/3 and filament density profiles in Figure 7.2 with the experimental profiles discussed in Chapter 4, the spatial profiles here are also consistent with experimental observations. This indicates that a stimulus applied only to the activation rate of Cdc42 is capable of causing the spatial segregation of the Rho proteins, leading to enhanced actin polymerization only at the front of the cell. Figure 7.3 (top plot) shows the change in membrane speed in response to a stimulus. The membrane speed increases from $0 \mu\text{m/s}$ (resting cell) to a steady state speed of approximately $0.3 \mu\text{m/s}$. Figure 7.3 (bottom plot) shows the initial increase and steady state barbed end profile in response to a stimulus. This plot is in lab coordinates and indicates the position of the leading edge and the barbed end profile at various time points. The actin profiles that result from this spatial regulation by the Rho proteins gives rise to stable spatial profiles and protrusion velocities that are consistent with experimental data, addressing Questions 1 and 2. The cell maintains these spatial profiles and persistent motion, even when the stimulus is removed.

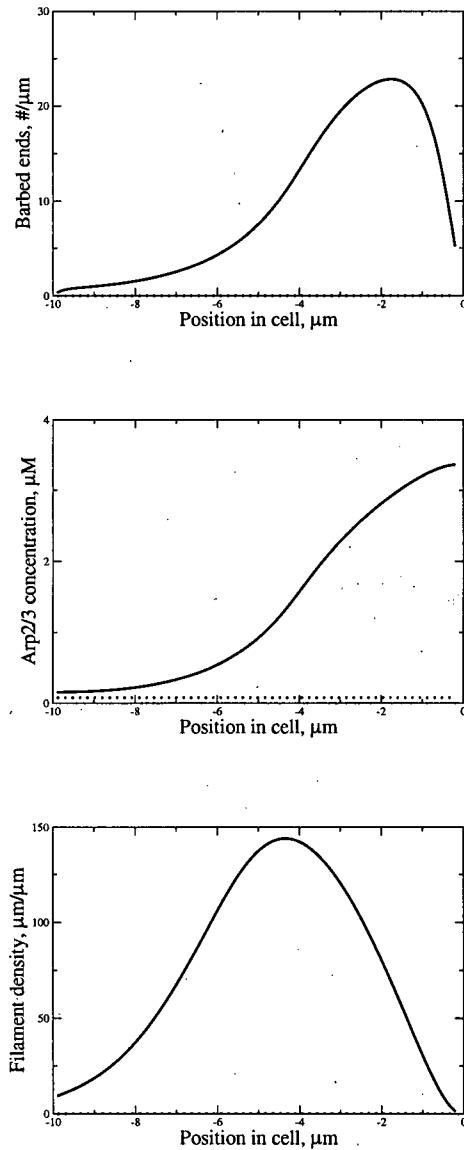


Figure 7.2: Barbed ends (top), Arp2/3 (middle) and filament density (bottom) are elevated near the leading edge ($x = 0$) in response to a graded transient gradient in the activation rate of Cdc42, I_c . Filament density increases more slowly, matching experimental observations. The corresponding Cdc42, Rac and Rho profiles are shown in Figure 6.7. The spatial profiles are shown before (dotted line) and after (solid line) application of the stimulus.

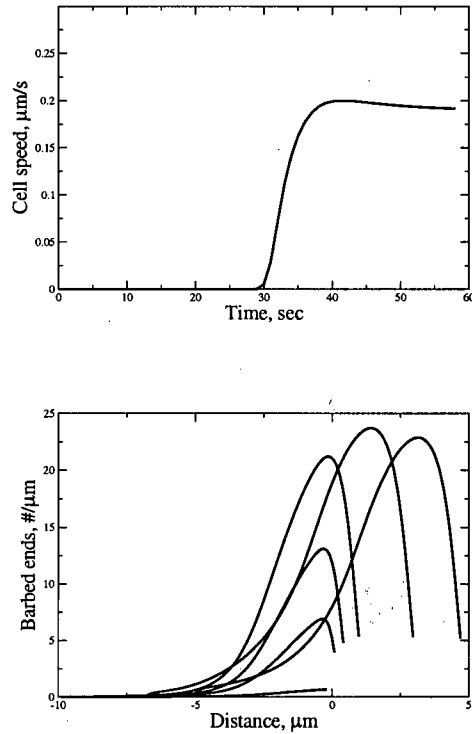


Figure 7.3: Membrane speed (top) and change in barbed end profile (bottom) in response to a gradient in the Cdc42 activation rate, I_c . The gradient in I_c was applied for one second, 20 seconds after the start of the simulation. After a delay of approximately 10 seconds, the cell initiates directed movement and the number of barbed ends increases to a steady state distribution. To show the initial rise of barbed ends, the spatial profiles are plotted every 5 seconds, then every 10 seconds as the cell reaches steady state.

7.6.2 Random stimuli cause the 1D cell model to initiate and maintain directed movement

In Section 6.6.2, it was demonstrated that a random stimulus in the Cdc42 activation rate leads to asymmetric localization of the Rho proteins with more than one domain with high Cdc42 and Rac. When I impose a random stimulus in I_c (Figure 7.4), the profile of barbed ends, Arp2/3 and filament density (right column) reflect the spatial profile of the Rho proteins (right column). For this particular stimulus, the cell speed is slow as the concentration of Cdc42 and Rac is low on the right boundary leading to a low number of barbed ends pushing on the membrane. Barbed ends do not persist outside areas with high active Rac since they are quickly capped. Thus barbed ends nucleated away from the leading edge in areas with high Cdc42 and Rac will not grow forward to the membrane and exert force. Other random stimuli produce different spatial patterns of multiple domains with high Cdc42 and Rac at the right boundary. This allows the cell to move at a relatively high speed due to the number of barbed ends at the leading edge. The internal domains with high Cdc42 and Rac persist even when the cell is moving rapidly. The spatial profiles shown here are not consistent with experimental observations and suggest there are other factors governing Rho protein activation and actin dynamics that are not taken into account here that would prevent these spatial profiles from occurring.

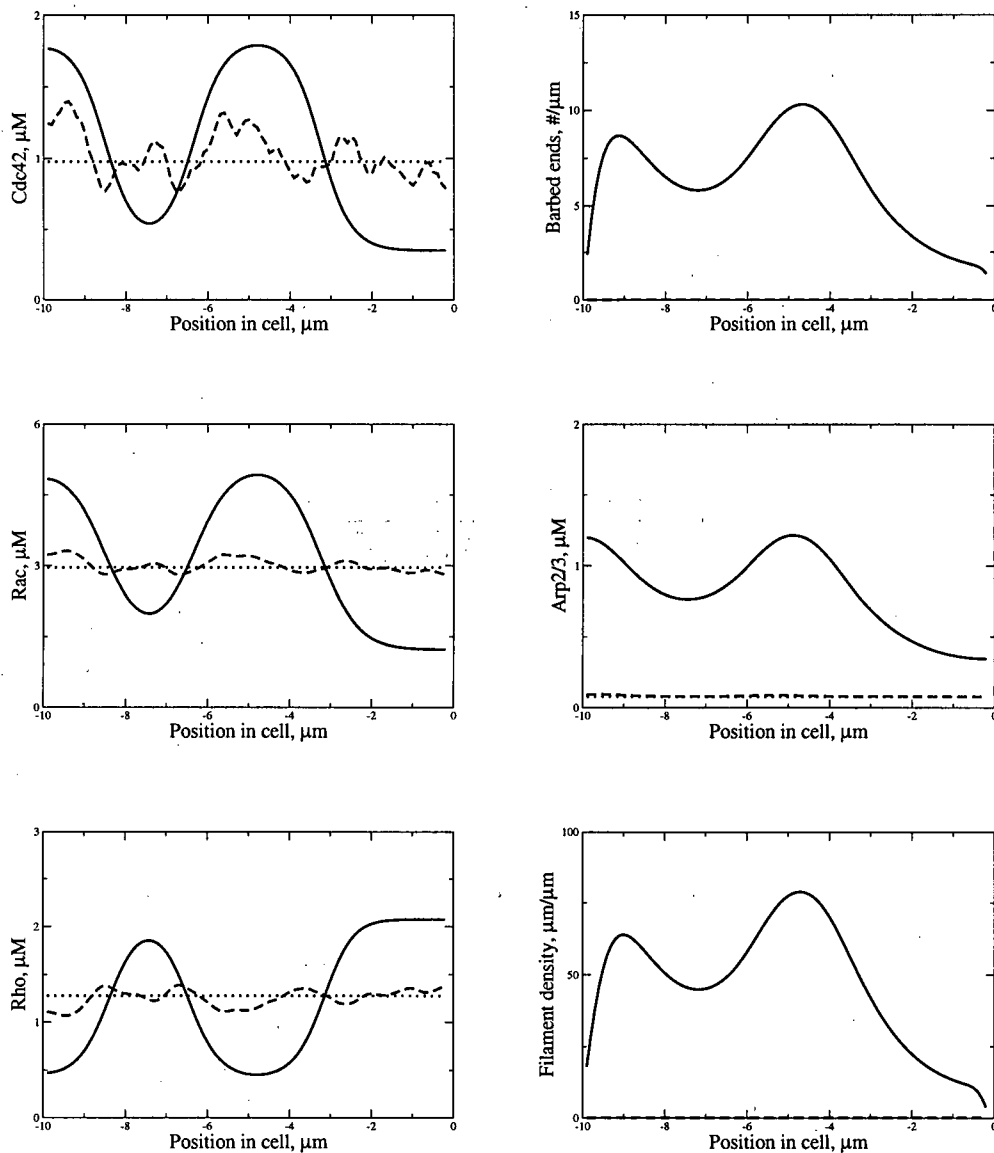


Figure 7.4: Barbed ends are generated in areas with high Cdc42 and Rac in response to a random stimulus in the activation rate of Cdc42, but are capped before they can reach the membrane. The cell initiates slow directed movement due to the low number of barbed ends at the leading edge. Left column: Cdc42 (top), Rac (middle) and Rho (bottom). Right column: Barbed ends (top), Arp2/3 (middle) and filament density (bottom). The spatial profiles are shown before (dotted line), during (dot-dash line) and after (solid line) application of the stimulus.

7.7 Discussion

In Chapter 3, a model of actin dynamics in the lamellipod of a motile cell was proposed and investigated. Chapter 6 reviewed a model of crosstalk between Rho proteins that led to spatial profiles similar to those believed to occur in motile cells. In this chapter, I combined these two modules based on known interactions between Rho proteins and actin dynamics. When this expanded model is exposed to a graded stimulus, the cell initiates movement at a reasonable speed. The stable spatial profiles of Rho proteins and actin components are in agreement with experimental observations, suggesting this model is capable of capturing some features of actin regulation in motile cells.

In the model of the Rho proteins, it was assumed that the activation rates are constant and that those rates are modulated only by other Rho proteins. However, a family of membrane-bound lipids, phosphoinositides (PIs), are known to regulate Rho protein activation by interacting directly with GEFs. In the next chapter, I propose a model to simulate interactions between PIs and Rho proteins to understand how interplay between these signalling molecules can reinforce the spatial profiles of both PIs and Rho proteins seen in motile cells. In Chapter 9, I combine all three modules, PIs, Rho proteins and actin dynamics, to gain a better understanding of actin polymerization regulation in motile cells.

Chapter 8

Phosphoinositides regulate Rho protein activation

In Chapters 6 and 7, the role of Rho proteins in regulating actin dynamics in motile cells was investigated. Crosstalk enables the Rho proteins to establish distinct spatial domains in response to a graded stimulus. This spatial segregation of the Rho proteins leads to enhanced actin polymerization at the leading edge, producing characteristic actin density profiles and initiation of directed cell motion. In this chapter, I propose a model of interactions between phosphoinositides (PIs) which are upstream effectors of the Rho proteins. It is known that the PIs are required for proper directed migration and it has been shown that they interact with Rho proteins to establish asymmetric localizations within a cell. Here, I build upon the model for Rho protein dynamics introduced in Chapter 6 and integrate PI dynamics. The model proposed here is currently the only one that couples PIs and Rho proteins using only experimentally established interactions.

8.1 Biological background

8.1.1 Phosphoinositides

Phosphoinositides (PIs) are membrane-bound lipids that are crucial for cell motility as they relay external signals to the inside of the cell. They also regulate activation of the Rho proteins and actin polymerization dynamics. They consist of a fatty acid tail on one end and an inositol head group on the other. The ring formed by the inositol head group can be phosphorylated at three positions, numbered 3, 4 and 5. The phosphorylation state of the PIs determines their activity: PIs with phosphate bound to all three positions regulate certain Rho protein GEFs while PIs with phosphates bound to the 4 and 5 positions are capable of removing capping protein from barbed ends (Martin, 1998). For notation purposes, PIs are written in a form that specifies which position(s) have bound phosphates. A PI with one phosphate bound at the 4 position is written PI(4)P while a PI with all three positions occupied is written PI(3,4,5)P.

All possible PIs are shown in Figure 8.1. PIs account for less than 10% of all membrane lipids (Toker, 2002).

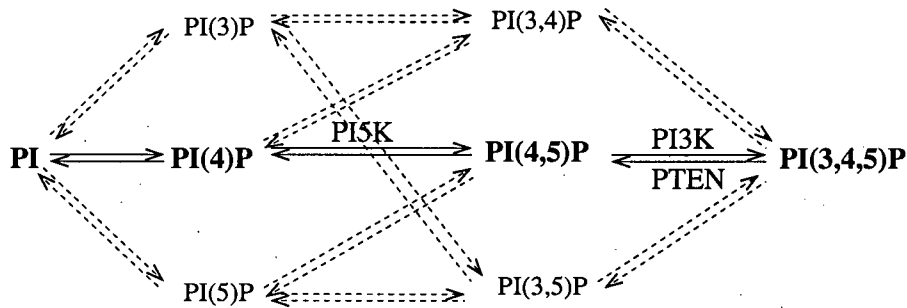


Figure 8.1: Schematic of all possible phosphoinositides (PIs) and interconversion between different forms. The PIs investigated in this thesis are indicated with bold letters.

In an unstimulated cell, PIs are evenly distributed on the membrane. Most of the PIs are in the unphosphorylated inactive state. Approximately 5% of the PIs are found in each of the PI(4)P and PI(4,5)P states while less than 0.25% have a phosphate bound to the 3 position (PI(3)P, PI(3,4)P, PI(3,5)P and PI(3,4,5)P) (Rameh and Cantley, 1999). I focus on the most abundant and best studied forms of the PIs, PI(4)P, PI(4,5)P and PI(3,4,5)P (henceforth referred to as PIP, PIP₂ and PIP₃, respectively) which are indicated in bold letters in Figure 8.1. In a resting cell, the concentration of PIP is 50 μM , PIP₂ is 30 μM and PIP₃ is 0.05 μM (Sternmark, 2000).

8.1.2 Phosphatases and kinases regulate the phosphorylation state of the PIs

Kinases, which add phosphates to a specific position, and phosphatases, which remove phosphates from a specific position, regulate the phosphorylation state of the PIs. While not all kinases and phosphatases have been identified, I focus on two kinases, PI5K and PI3K, and one phosphatase, PTEN, that have been isolated and studied. The activity of PI5K, PI3K and PTEN is shown schematically in Figures 8.1 and 8.2.

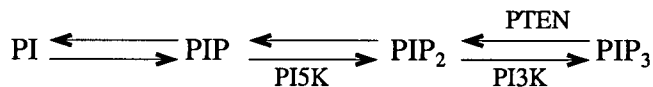


Figure 8.2: Simplified schematic of the PIs, showing lipids, kinases and phosphatase included in the model

PI5K and PI3K are kinases that add phosphates to the 5 and 3 position, respectively. PI5K

is responsible for converting PIP to PIP₂ while PI3K is responsible for converting PIP₂ to PIP₃. PTEN is a phosphatase that removes phosphates from the 3 position, converting PIP₃ back to PIP₂. Figure 8.2 indicates which phosphorylation events these kinases and phosphatase regulate. Unlike their targets, kinases and phosphatases can diffuse in the cytoplasm. In fact, membrane recruitment and spatial reorganization of PI3K and PTEN is one of the first intracellular responses when a cell is exposed to an external signal (Merlot and Firtel, 2003; Weiner et al., 2002).

In unstimulated cells, PTEN is associated with the membrane while PI3K is distributed in the cytoplasm, ensuring that PIP₃ is present only at very low concentrations. When a cell is exposed to an external chemoattractant gradient, PTEN is released from the membrane at the front of the cell, allowing PI3K to associate with the membrane. PTEN remains bound to the sides and the back of the stimulated cell. This spatial redistribution of PI3K and PTEN allows the concentration of PIP₃ to be elevated only at the leading edge (Funamoto et al., 2002; Huang et al., 2003b; Iijima and Devreotes, 2002).

8.1.3 PIs regulate activation of Rho proteins

PIP₃ activates Cdc42 and Rac

Experiments have determined that PIP₃ activates Cdc42 and Rac by activating specific GEFs. Early experiments that blocked the activity of PIP₃ by incubating neutrophils with PI3K inhibitors demonstrated that PIP₃ is required for the activation of Cdc42 and Rac (Hawkins et al., 1995; Srinivasan et al., 2003; Wang et al., 2002; Weiner et al., 2002). Another experiment with lipid vesicles in cell extract established that PIP₃ and Cdc42 (but not Rac) are required for actin assembly (Ma et al., 1998). Using RNA interference, an experimental protocol that downregulates expression of a particular protein, experimentalists were able to determine which proteins are involved in PIP₃-mediated activation of Cdc42 and Rac. PIP₃ activates both Cdc42-specific (PIX_α, Li et al. (2003)) and Rac-specific (P-REX1, Welch et al. (2002)) GEFs. PIP₃ was also found to activate GEFs that can activate both Cdc42 and Rac (Vav2 and Vav3, Aoki et al. (2005)). These experimental results suggest PIP₃ can directly regulate the activation of both Cdc42 and Rac and I incorporate this activation into the model. I use the model to investigate PIP₃ activation of Cdc42 and Rac and suggest which interactions are crucial for proper gradient sensing.

8.1.4 Rho proteins regulate phosphorylation state of the PIs

Rac enhances accumulation of PIP₂ and PIP₃ by activating PI5K and PI3K

Experimental evidence demonstrated that Rac enhances the activity of the two kinases discussed above, PI5K and PI3K. It has been shown in platelets and neutrophils that Rac can directly activate PI5K (Tolias et al., 2000; van Hennik et al., 2003). Observations of the fluorescent distribution of PIP₃ and active Rac in neutrophils demonstrated that Rac and not Cdc42 is required to enhance the activity of PI3K (Srinivasan et al., 2003). Experiments in neuron-like cells suggested that Cdc42 and Rac can interact with the GEFs Vav2/3 to enhance PI3K activity (Aoki et al., 2005) although the exact mechanism is unknown. It has also been demonstrated that active Rac and Cdc42 can bind directly to PI3K *in vitro* but it is not clear if this occurs in whole cells (Bokoch et al., 1996; Tolias et al., 1995; Zheng et al., 1994). These experiments establish that Rac can directly activate PI5K, and while it appears that Rac is also capable of enhancing PI3K activity, the mechanism is unknown. In the model, I assume that Rac enhances the conversion rate of PIP to PIP₂, and of PIP₂ to PIP₃. I explore the effect of Rac activation of PI5K and PI3K on the spatial distribution of the PIs and produce testable hypotheses that can help verify and improve the model proposed here.

Rho activates the phosphatase PTEN

Experiments in epithelial cells and neutrophils have determined that Rho activates Rho kinase, ROCK, which directly binds to and phosphorylates (activates) PTEN (Li et al., 2003, 2005). Observations of the spatial distribution of PTEN, PI3K and Cdc42 indicate that PTEN is excluded from areas with high concentrations of PI3K and Cdc42 (Funamoto et al., 2002; Huang et al., 2003b; Iijima and Devreotes, 2002; Li et al., 2003, 2005). It is not clear what mechanism may lead to this mutual spatial exclusion. To incorporate the effect of Rho on PTEN, I enhance the conversion rate from PIP₃ to PIP₂ in areas where the concentration of Rho is elevated. I use the model to investigate how mutual inhibition of Cdc42 and Rho could lead to spatial exclusion of PTEN from areas with high concentration of PI3K and Cdc42.

8.1.5 Role of phosphoinositides in cell motility

It has been established that PI3K and PTEN are among the first intracellular signalling molecules to establish spatial gradients in response to an external stimulus (Merlot and Firtel, 2003; Weiner et al., 2002). This causes PIP₃ to establish an intracellular gradient with high concentration

at the leading edge. The appearance of PIP₃ at the leading edge leads to enhanced activation of Cdc42 and Rac. Rac then enhances the conversion of the PIs, creating a feedback loop that ensures that high levels of PIP₂, PIP₃, Cdc42 and Rac are maintained at the leading edge.

Motile cells exhibit a number of general behaviours. We use our model to suggest mechanisms that may cause these behaviours to occur and determine which interactions are crucial for proper gradient sensing and initiation of directed movement. The following are some general observations about PI and Rho protein activity in motile cells:

1. Motile cells establish stable asymmetric spatial profiles of PIs and small G proteins in response to a stimulus (Funamoto et al., 2002; Iijima and Devreotes, 2002; Kraynov et al., 2000; Nalbant et al., 2004; Xu et al., 2003).
2. Translocation of PTEN to the rear of a motile cell is not necessary for directed migration (Xu et al., 2003).
3. Constitutively inactive Cdc42 (Cdc42-GDP) prevents proper gradient sensing but the cell can still migrate (Srinivasan et al., 2003).
4. Cdc42 and PTEN spatially exclude each other (Li et al., 2003, 2005).
5. Intracellular gradients of PIs and small G proteins are independent of the stimulus strength (gradient amplification) (Weiner et al., 2002).

In view of these observations, we wish to address the following questions with our model:

1. Can a model of PI and Rho protein interactions based on reasonable biological assumptions establish stable asymmetric spatial profiles that are independent of the signal strength, in response to a gradient in the conversion rate of PIP₂ and PIP₃ (gradient amplification)?
2. Can this model explain why increased PTEN activity at the rear of the cell is not necessary for proper gradient sensing?
3. What mechanism might be responsible for preventing proper gradient sensing in the absence of active Cdc42?
4. What interactions might lead to the mutual spatial exclusion of Cdc42 and PTEN?
5. Which arrows in Figure 8.3 are needed for proper gradient sensing and directed movement?

8.2 Previous modelling efforts

Experimental observations have made it clear that PIs and Rho proteins are crucial for proper gradient sensing. The following models propose various signalling pathways using PIs and Rho proteins to give rise to signal amplification and proper gradient detection.

An early model by Meinhardt (1999) proposed that generation of a local activator and diffusible inhibitor in response to an external signal can give rise to cell polarization. This model leads to stable pattern formation due to a Turing-type mechanism that internally amplifies the external signal. However, this locks the spatial profiles and the cell is insensitive to changes in the external signal and cannot adjust its direction of movement in response to later cues. This problem was addressed by adding a second slow inhibitor that destroys the spatial profiles, allowing the cell to sense a change in the stimulus source and establish a new leading edge in the appropriate direction. This model was improved by Narang et al. (2001), Subramanian and Narang (2004), and Narang (2006), where it was suggested that lipids such as phosphoinositides are the local activators proposed by Meinhardt (1999). They proposed that the local lipid concentration creates a positive feedback loop, causing local lipid accumulation at the front and playing the role of local activator. Global inhibition is provided by substrate depletion, limiting the accumulation of lipids at the front. The second slow inhibition is provided by receptor desensitization. While these models are able to reproduce polarization and signal amplification in response to an external signal, there are currently no justifiable candidate molecules for the local activator and two inhibitors that satisfy the diffusion rates and activation kinetics required by the model.

Another modelling approach first proposed in Levchenko and Iglesias (2002) relies on local excitation/global inhibition (LEGI) modules to simulate adaptation in response to a uniform stimulus and amplification and gradient sensing in response to a spatially graded stimulus, as discussed in Chapter 1. This model was refined in later papers (Krishnan and Iglesias, 2004; Ma et al., 2004) using more biologically justifiable signalling networks. These models rely entirely on the LEGI modules to produce adaptation and amplification and the simulations are very sensitive to changes in parameter values. There are also no biological candidates for the activators or inhibitors required for the LEGI modules.

Postma and Van Haastert (2001) used a simple model of local positive and global negative feedback loops to model the accumulation of signalling molecules at the leading edge. As with

Meinhardt (1999), the spatial profiles become "locked" and the cell is no longer sensitive to changes in the stimulus. Gamba et al. (2005) used a biologically motivated model with simple mass-action kinetics to reproduce polarization and signal amplification. In this model, receptor activation leads to PIP₃ production and the spatial localization and interactions of PIP₂, PIP₃, PI3K and PTEN lead to gradient sensing. This model considers only PIs and does not include Rho proteins or actin dynamics. This model also relies on continuous receptor activation by an external signal - polarization will not persist when the signal is removed.

The model proposed here differs from these previous efforts by taking into account PIs, Rho proteins and, in Chapter 9, actin dynamics. Unlike the other models discussed here, my model is based entirely on interactions that have been experimentally observed or confirmed and does not rely on the existence of unknown effectors. I also consider the concentration of the PIs and Rho proteins everywhere on the domain, not just on the perimeter of the cell. I will show that the spatial profiles produced by this model are not "locked" and remain sensitive to changes in the stimulus source.

8.3 Model of PI and small G protein interactions

Based on the experimental observations discussed above, I propose the following model to simulate the dynamics of the PIs and Rho proteins. A schematic diagram of the interactions is shown in Figure 8.3.

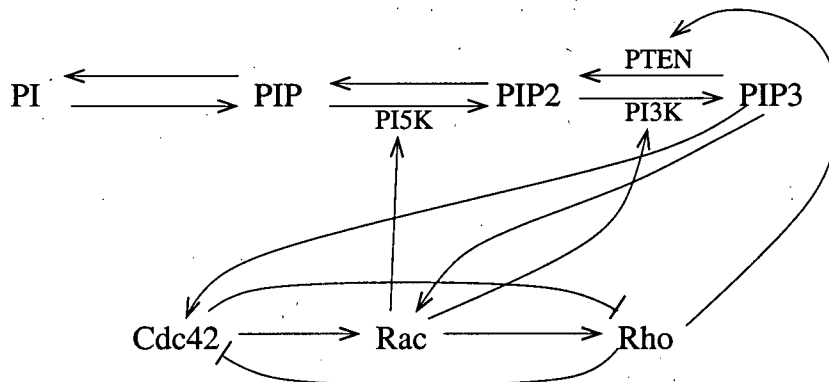


Figure 8.3: Schematic diagram of proposed interactions between the phosphoinositides PI, PIP, PIP₂ and PIP₃ and the small G proteins Cdc42, Rac and Rho based on my compilation of the experimental literature in Section 8.1.

8.3.1 Definitions

I define the following variables and parameters:

- P_1 Concentration of PIP, μM
- P_2 Concentration of PIP₂, μM
- P_3 Concentration of PIP₃, μM
- k_{ij} Conversion rate from PIP_{*i*} to PIP_{*j*}, s^{-1}
- x Spatial coordinate
- t Time coordinate

8.3.2 Model assumptions

In formulating the model, I make the following assumptions, in addition to those listed in Chapter 6:

1. PIs are not made or degraded but only converted between different phosphorylation states.
2. PIs are found only on the membrane, where they diffuse at a slow rate.
3. The dynamics of the PIs can be described using mass-action kinetics.
4. PIs enhance the activation rate of target Rho proteins.
5. The concentration of unphosphorylated PIs is large compared to the concentration of the phosphorylated forms.

I also include previous assumptions about the interactions between the small G proteins, as in Chapter 6.

8.3.3 Description of the model

Quasi steady state approximation of PI5K, PI3K and PTEN

To keep the model as simple as possible I will eliminate these kinases and phosphatases using a quasi-steady state (QSS) assumption. Let ϕ be the active form of a general kinase or phosphatase. In a resting cell in the absence of external signals, I assume that ϕ is activated at the rate I_ϕ and decays at the rate δ . Ignoring diffusion of ϕ , the dynamics of ϕ can be expressed as

$$\frac{d\phi}{dt} = I_\phi - \delta\phi. \quad (8.1)$$

I assume there is an unlimited pool of the inactive form and I take I_ϕ to be constant. At steady state, the concentration of ϕ can be expressed as

$$\phi = \frac{I_\phi}{\delta}.$$

To take into account the activity of a general Rho protein G on the activation of ϕ , I make the following default assumption (which is as simple as possible, given the lack of biological data) that

$$\frac{d\phi}{dt} = \frac{I_\phi}{2} \left(1 + \alpha \frac{G}{G_b} \right) - \delta\phi \quad (8.2)$$

where α is the strength of the effect of G on the activation of ϕ . I take $\alpha = 1$ (dimensionless) so that the effect of G is simply proportional to its fractional elevation (or reduction) relative to its baseline concentration, G_b . In a resting cell, $G = G_b$ and Equation (8.2) reduces to Equations (8.1). While Equation (8.2) is likely to be a saturating reaction, I use this form to avoid introducing additional unknown parameters and as proof of principle. I assume ϕ is in QSS and, using Equation (8.2), I arrive at the concentration for ϕ :

$$\phi \approx \frac{I_\phi}{2\delta} \left(1 + \alpha \frac{G}{G_b} \right).$$

I incorporate this expression into the PI equations as follows. Consider a general PI P_i that is converted to P_j by the kinase ϕ at a rate \hat{k}_{ij} . Assuming mass-action kinetics, the conversion from P_i to P_j can be written as

$$\frac{dP_i}{dt} = -\hat{k}_{ij}\phi P_i + (\text{other terms}).$$

Using the quasi-steady state approximation for ϕ from above, the ODE for P_i becomes:

$$\frac{dP_i}{dt} = -\hat{k}_{ij} \frac{I_\phi}{2\delta} \left(1 + \frac{G}{G_B} \right) P_i.$$

Let $k_{ij} = \frac{\hat{k}_{ij} I_\phi}{\delta}$, then

$$\frac{dP_i}{dt} = -\frac{k_{ij}}{2} \left(1 + \frac{G}{G_B} \right) P_i.$$

The rate constants k_{ij} represent the basal rate of conversion from PIP_i to PIP_j when G is at its basal concentration ($G = G_b$). To simulate the observed spatial asymmetry of PI3K and PTEN in response to a spatially graded external signal, I impose a gradient in the rate constants k_{23} and k_{32} , respectively. I use this expression in the model to simulate the effect of the Rho

proteins on the activity of PI5K, PI3K and PTEN.

I also do not keep track of the concentration of unphosphorylated PIs and instead assume that the conversion to PIP occurs at a constant rate. A schematic of the model using the same notation as Equations (8.3) is shown in Figure 8.4.

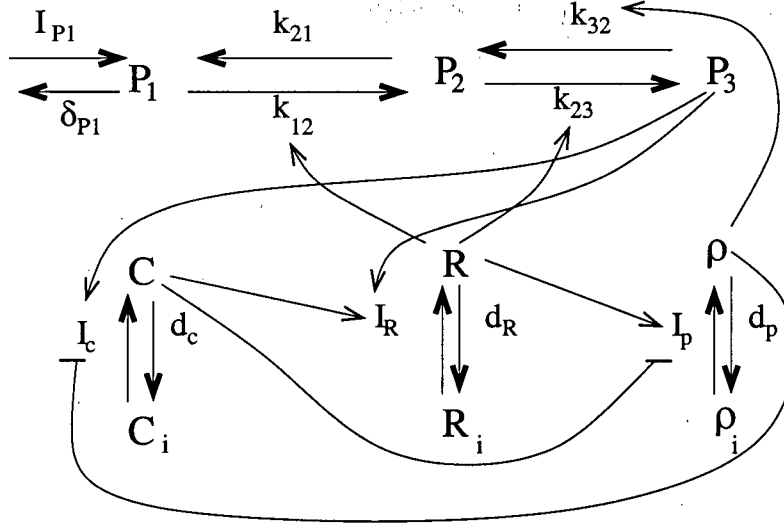


Figure 8.4: Schematic diagram of interactions shown in Figure 8.3 using the notation of Equations (8.3).

The PI equations are:

$$\frac{\partial P_1}{\partial t} = I_{P1} - \delta_{P1}P_1 + k_{21}P_2 - \frac{k_{12}}{2} \left(1 + \frac{R}{R_b}\right) P_1 + D_P \frac{\partial^2 P_1}{\partial x^2}, \quad (8.3a)$$

$$\frac{\partial P_2}{\partial t} = -k_{21}P_2 + \frac{k_{12}}{2} \left(1 + \frac{R}{R_b}\right) P_1 - \frac{k_{23}}{2} \left(1 + \frac{R}{R_b}\right) P_2 \quad (8.3b)$$

$$+ \frac{k_{32}}{2} P_3 \left(1 + \frac{\rho}{\rho_b}\right) + D_P \frac{\partial^2 P_2}{\partial x^2}, \quad (8.3c)$$

$$\frac{\partial P_3}{\partial t} = \frac{k_{23}}{2} \left(1 + \frac{R}{R_b}\right) P_2 - \frac{k_{32}}{2} \left(1 + \frac{\rho}{\rho_b}\right) P_3 \quad (8.3d)$$

$$+ D_P \frac{\partial^2 P_3}{\partial x^2}, \quad (8.3e)$$

where the baseline concentrations R_b and ρ_b are the concentrations of Rac and Rho in a resting cell.

I assume Rac enhances the conversion of P_1 to P_2 (via PI5K) according to the term

$$\frac{k_{12}}{2} \left(1 + \frac{R}{R_b}\right) P_1$$

and the conversion of P_2 to P_3 via PI3K according to the term

$$\frac{k_{23}}{2} \left(1 + \frac{R}{R_b}\right) P_2,$$

as discussed above. Similarly, Rho enhances the conversion of P_3 to P_2 via PTEN according to the term

$$\frac{k_{32}}{2} \left(1 + \frac{\rho}{\rho_b}\right) P_3.$$

Parameter values used to simulate the PI equations are given in Table 8.1.

The Rho protein equations are the same as in Chapter 6 except that P_3 enhances activation of Cdc42 and Rac. The equations for the active Rho proteins are amended to include dependence on PIs using a similar quasi-steady state argument discussed in Section 8.3.3. The Rho protein equations are:

$$\frac{\partial C}{\partial t} = \frac{I_c C_i / C_{tot}}{2(1 + (\rho/a_1)^n)} \left(1 + \frac{P_3}{P_{3b}}\right) - d_c C - x'_{edge} \frac{\partial C}{\partial x} + D_m \frac{\partial^2 C}{\partial x^2}, \quad (8.4a)$$

$$\frac{\partial R}{\partial t} = (I_r + \alpha C)(R_i / R_{tot}) \left(1 + \frac{P_3}{P_{3b}}\right) - d_r R - x'_{edge} \frac{\partial R}{\partial x} + D_m \frac{\partial^2 R}{\partial x^2}, \quad (8.4b)$$

$$\frac{\partial \rho}{\partial t} = \frac{(I_p + \beta R)(\rho_i / P_{tot})}{1 + (C/a_2)^n} - d_p \rho - x'_{edge} \frac{\partial \rho}{\partial x} + D_m \frac{\partial^2 \rho}{\partial x^2}, \quad (8.4c)$$

$$(8.4d)$$

where P_{3b} is the baseline concentration of PIP_3 in a resting cell. The equations for the inactive forms similarly follow Equations (6.2).

Parameter values used to simulate the Rho protein equations are given in Table 6.1.

8.4 Parameter values

There is little quantitative data about PIs in motile cells since most experiments are concerned with the spatial localization of the PIs. However, time course data that tracks the increase in fluorescence indicate that PIs reach their peak concentration approximately 10 seconds after a stimulus is applied (Huang et al., 2003b; Insall and Weiner, 2001). The approximate baseline concentration of PIs in unstimulated cells is $P_{1b} = [PIP]_b \approx 50 \mu\text{M}$, $P_{2b} = [PIP_2]_b \approx 30 \mu\text{M}$ and $P_{3b} = [PIP_3]_b \approx 0.05 \mu\text{M}$ (Sternmark, 2000). The equations for the phosphoinositides in a

resting cell (when all the Rho proteins are at their baseline concentrations, $G = G_b$) are:

$$\frac{\partial P_1}{\partial t} = I_{P1} - \delta_{P1}P_1 + k_{21}P_2 - k_{12}P_1 + D_P \frac{\partial^2 P_1}{\partial x^2}, \quad (8.5a)$$

$$\frac{\partial P_2}{\partial t} = -k_{21}P_2 + k_{12}P_1 - k_{23}P_2 + k_{32}P_3 + D_P \frac{\partial^2 P_2}{\partial x^2}, \quad (8.5b)$$

$$\frac{\partial P_3}{\partial t} = k_{23}P_2 - k_{32}P_3 + D_P \frac{\partial^2 P_3}{\partial x^2}. \quad (8.5c)$$

From these equations it follows that there are relationships between the biochemical parameters and the steady state concentrations of the PIs. Therefore, at baseline, the concentration of the three forms are

$$P_{1b} = \frac{I_{P1}}{\delta_{P1}} = 50\mu\text{M}, \quad (8.6a)$$

$$P_{2b} = \frac{k_{12}}{k_{21}}P_{1b} = \frac{k_{12}I_{P1}}{k_{21}\delta_{P1}} = 30\mu\text{M}, \quad (8.6b)$$

$$P_{3b} = \frac{k_{23}}{k_{32}}P_{2b} = \frac{k_{23}k_{12}I_{P1}}{k_{32}k_{21}\delta_{P1}} = 0.05\mu\text{M}. \quad (8.6c)$$

Using the baseline concentration of the PIs and knowing that the PIs reach their maximum steady state in approximately 10 s in response to a graded stimulus, I use numerical simulations of the PIs in the absence of the Rho proteins to estimate biochemical rates. In the simulations, I vary δ_{P1} , k_{21} and k_{32} and determine the remaining parameters using the steady state PI concentrations from above: $I_{P1} = P_{1b}\delta_{P1}$, $k_{12} = P_{2b}k_{21}/P_{1b}$, $k_{23} = P_{3b}k_{32}/P_{2b}$.

I find the following parameter values give the appropriate time course for the PIs. PIP is formed from the pool of unphosphorylated PI at the rate $I_{p1} = 10.5 \mu\text{M/s}$ and dephosphorylates at the rate $\delta_{P1} = 0.21 \text{ s}^{-1}$. PIP is converted to PIP₂ by PI5K at the rate $k_{12} = 0.084 \text{ s}^{-1}$ and PIP₂ is converted back to PIP at the rate $k_{21} = 0.14 \text{ s}^{-1}$. PIP₂ is converted to PIP₃ by PI3K at the rate $k_{23} = 0.00072 \text{ s}^{-1}$ and PIP₃ is converted back to PIP₂ by PTEN at the rate $k_{32} = 0.43 \text{ s}^{-1}$. Simulations that include both PIs and Rho proteins are not sensitive to PI parameter values as increasing or decreasing these parameters by a power of 10 does not significantly change the simulation results.

I assume all PIs diffuse in the membrane at the same rate (since the lipid tail embedded in the membrane which provides the greatest resistance to movement is the same for all PIs) and it has been determined experimentally that PIP₃ diffuses at the rate $D_p = 5\mu\text{m}^2/\text{s}$ (Postma et al., 2004). The diffusion rate of PIs is much higher than the diffusion rate of membrane-bound Rho proteins ($D_m = 0.1\mu\text{m}^2/2$).

Parameter	meaning	value	source
I_{P1}	PIP ₁ input rate	10.5 $\mu\text{M}/\text{s}$	[1]
δ_{P1}	PIP ₁ decay rate	0.21 s^{-1}	[1]
k_{12}	PIP ₁ to PIP ₂ baseline conversion rate (by PI5K)	0.084 $\mu\text{M}^{-1}\text{s}^{-1}$	[1]
k_{21}	PIP ₂ to PIP ₁ conversion rate	0.14 s^{-1}	[1]
k_{23}	PIP ₂ to PIP ₃ baseline conversion rate (by PI3K)	0.00072 $\mu\text{M}^{-1}\text{s}^{-1}$	[1]
k_{32}	PIP ₃ to PIP ₂ baseline conversion rate (by PTEN)	0.43 $\mu\text{M}^{-1}\text{s}^{-1}$	[1]
D_P	PI diffusion rate	5 $\mu\text{m}^2 \text{s}^{-1}$	[2]
P_{1b}	typical level of PIP ₁	50 μM	[3]
P_{2b}	typical level of PIP ₂	30 μM	[3]
P_{3b}	typical level of PIP ₃	0.05 μM	[3]

Table 8.1: Parameter estimates relevant to phosphoinositide dynamics. Cited sources: [1]: estimated in text, [2]: Postma et al. (2004), [3]: Sternmark (2000).

These parameter values are compiled in Table 8.1.

8.5 Simulations

I simulate the PI and Rho protein equations (Equations (8.3) and (8.4)) on a 1D domain representing a transect of the lamellipodium of a motile cell (see Figure 1.8). Since I am not yet incorporating actin dynamics, the simulations are performed in a stationary cell, making $x'_{edge} = 0$. First derivatives are discretized using Forward Euler and second derivatives are discretized using centered differencing.

To mimic the translocation of PI3K and PTEN in response to an external signal, the conversion of PIP₂ to PIP₃, k_{23} , was reduced at the back of the cell and the rate of PIP₃ to PIP₂ conversion, k_{32} , was reduced at the front of the cell. This gradient was applied for one second, unless otherwise noted.

8.6 Results

8.6.1 PIs and Rho proteins establish stable asymmetric spatial profiles in response to a graded stimulus

The combined model, Equations (8.3) and (6.2), establishes stable spatially asymmetric profiles of the PIs and Rho proteins in response to a transient gradient in the biochemical rate constants k_{23} and k_{32} . Figure 8.5 shows the spatial profiles of the PIs and Rho proteins before and after the application of the stimulus. PIP₂ and PIP₃ concentration are elevated at the front of the cell along with active Cdc42 and Rac while active Rho is elevated at the rear of the cell. These

spatial profiles are in agreement with observed profiles of PIs and Rho proteins in motile cells. The magnitude of the spatial profiles in the PIs and Rho proteins is independent of the steepness of the applied stimulus, also in agreement with experimental observations. The model is very sensitive to an applied stimulus: a 2% gradient in k_{23} and k_{32} from the front to the back of the cell applied for 0.1 seconds resulted in the establishment of the asymmetric spatial profiles. The model is insensitive to large changes in most parameter values. Increasing or decreasing the parameter values regulating the PIs by a factor of 10 does not significantly change the simulation results. The Rho protein model is only sensitive to changes in the Hill coefficient. Lowering this parameter leads to loss of bistability and polarization. These results suggest that the model of PI and Rho protein interactions is capable of producing stable asymmetric spatial profiles with magnitudes independent of the signal strength (Question 1).

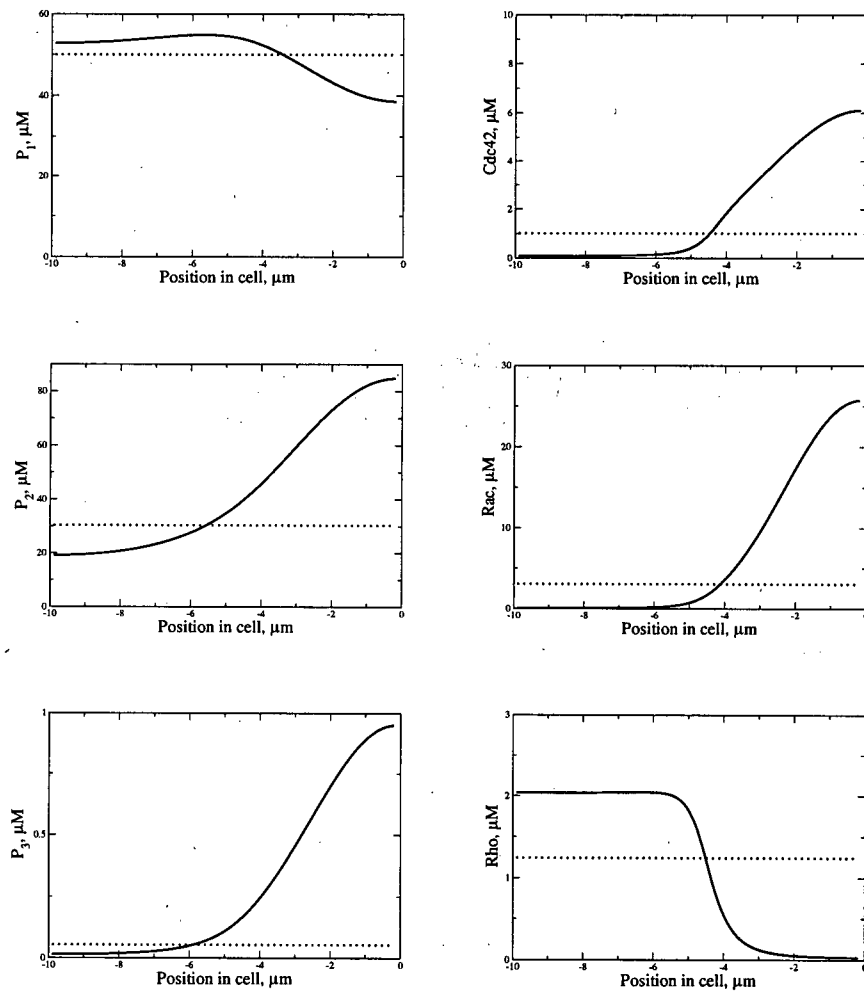


Figure 8.5: PIs and Rho proteins establish stable asymmetric spatial profiles in response to a transient graded stimulus. Left column: Spatial profile of P_1 =[PIP] (top), P_2 =[PIP₂] (middle) and P_3 =[PIP₃] (bottom). Right column: Spatial profile of active Cdc42 (top), Rac (middle) and Rho (bottom). Spatial profiles are shown before (dotted line) and after (solid line) application of a transient graded stimulus in the rates of conversion between P_2 and P_3 . The spatial profiles that result from the transient stimulus agree with experimental observations.

8.6.2 Activation of Cdc42, not Rac, by PIP₃ required for proper asymmetric spatial profiles

Experimental evidence indicates that PIP₃ activates both Cdc42 and Rac by enhancing the activity of specific GEFs (Aoki et al., 2005; Li et al., 2003; Welch et al., 2002). With the model, I can investigate which of these pathways are important to directed movement. As shown in Figure 8.6, when PIP₃ enhances only Cdc42 activation, the model displays proper spatial localization of PIs and Rho proteins. However, when PIP₃ enhances only Rac activation, the model displays the opposite spatial profiles (Figure 8.6). This spatial reversal of the profiles is due to the activation of Rho by Rac. Rac enhances Rho activation at the front of the cell which keeps Cdc42 low. When the stimulus is removed, Rho remains elevated at the front of the cell while active Rac decreases since it is receiving no input from the stimulus or Cdc42. This allows a spatial profile to develop with Rho high at the front of the cell and PIP₂, PIP₃, Cdc42 and Rac elevated at the back. This indicates that spatial localization of the PIs and Rho proteins is possible when PIP₃ enhances activation of Rac and not Cdc42, but the spatial profiles that result will not necessarily cause the cell to move in the direction indicated by the stimulus. This is consistent with experiments demonstrating that cells lacking active Cdc42 are able to move but cannot properly detect the direction of the gradient or the source of the stimulus (Jones et al., 1998), addressing Question 3. This also addresses Question 5, and indicates that the arrow from PIP₃ to Cdc42 is required for proper polarization while the arrow from PIP₃ to Rac is not required.

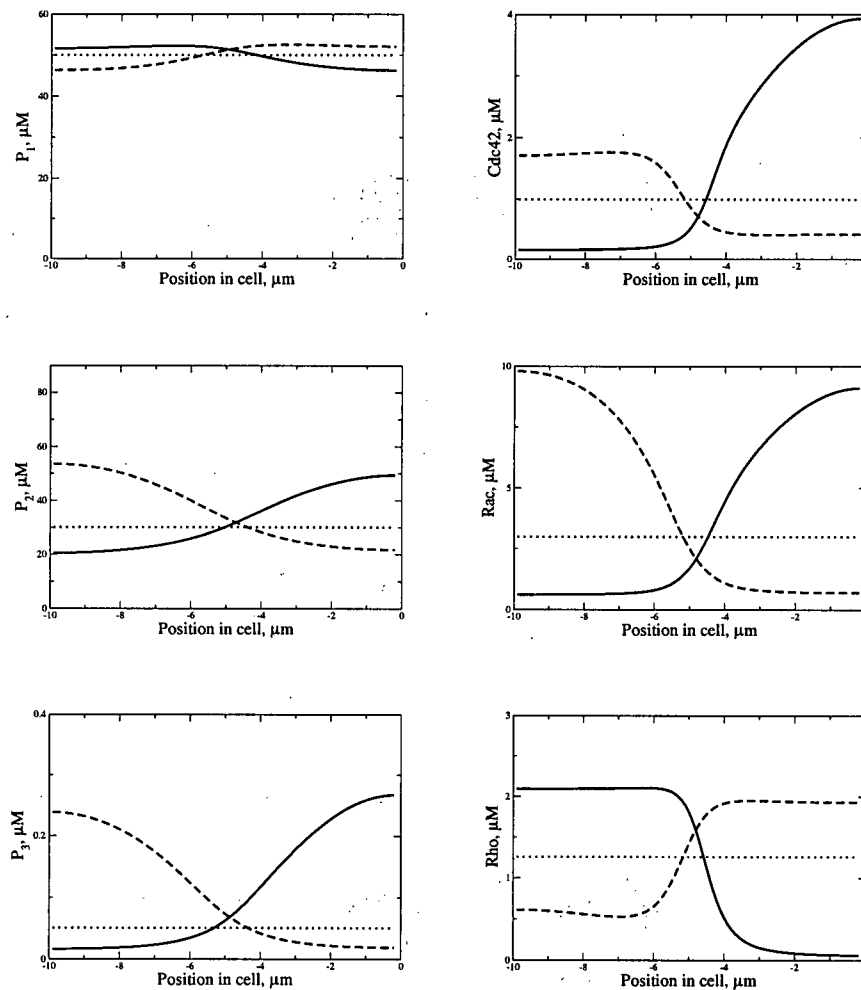


Figure 8.6: Cells lacking active Cdc42 cannot properly detect the direction of a stimulus but are able to initiate movement. Variables shown are the same as in Figure 8.5, showing the asymmetry in the spatial profiles is reversed when PIP_3 enhances activation of Rac and not Cdc42. Profiles are shown before (dotted line) and after application of a transient graded stimulus in the rates of conversion between P_2 and P_3 when PIP_3 enhances activation of only Cdc42 (solid line) or only Rac (dashed line). The spatial profiles that result from the transient stimulus are stable. Note that when PIP_3 enhances activation of Cdc42, the resulting spatial asymmetric profiles are consistent with the full model. This suggests that cells lacking active Cdc42 will not be able to properly detect the direction of a stimulus but still be able to initiate movement. This is consistent with experimental results.

8.6.3 Activation of PI5K or PI3K by Rac leads to asymmetric spatial profiles of PIs and Rho proteins

Experiments have determined that active Rac directly interacts with and activates PI5K, the kinase that phosphorylates PIP to form PIP₂ (Tolias et al., 2000; van Hennik et al., 2003). Other experiments have demonstrated that active Rac is important for PI3K activity although the mechanism of interaction remains unknown (Srinivasan et al., 2003; Welch et al., 2003). From the equations, it is clear that PIs cannot maintain asymmetric distributions without feedback from the Rho proteins, once the stimulus is removed. As shown in Figure 8.7, Rac activation of either kinase, PI5K or PI3K, leads to an asymmetric distribution of PIP₃, although the concentration of PIP₃ at the front has a lower magnitude than when both kinases are activated by Rac. When Rac enhances only PI3K, there is no asymmetric distribution of PIP or PIP₂, only PIP₃, while Rac activation of PI5K leads to asymmetric distributions of all three PIs. The concentration of PIP₃ at the front of the cell is higher when Rac enhances PI3K activity compared to when Rac enhances PI5K activity, suggesting that increasing the conversion rate from PIP₂ to PIP₃ provides greater accumulation of PIP₃ than simply increasing the concentration of the substrate, PIP₂. These simulation results suggest that some feedback from Rac onto the PIs through kinase activity is required for the maintenance of asymmetric profiles in the PIs after the removal of the stimulus, addressing Question 5, and enhancing the rate of PIP₂ to PIP₃ conversion provides the greatest accumulation of PIP₃ at the leading edge.

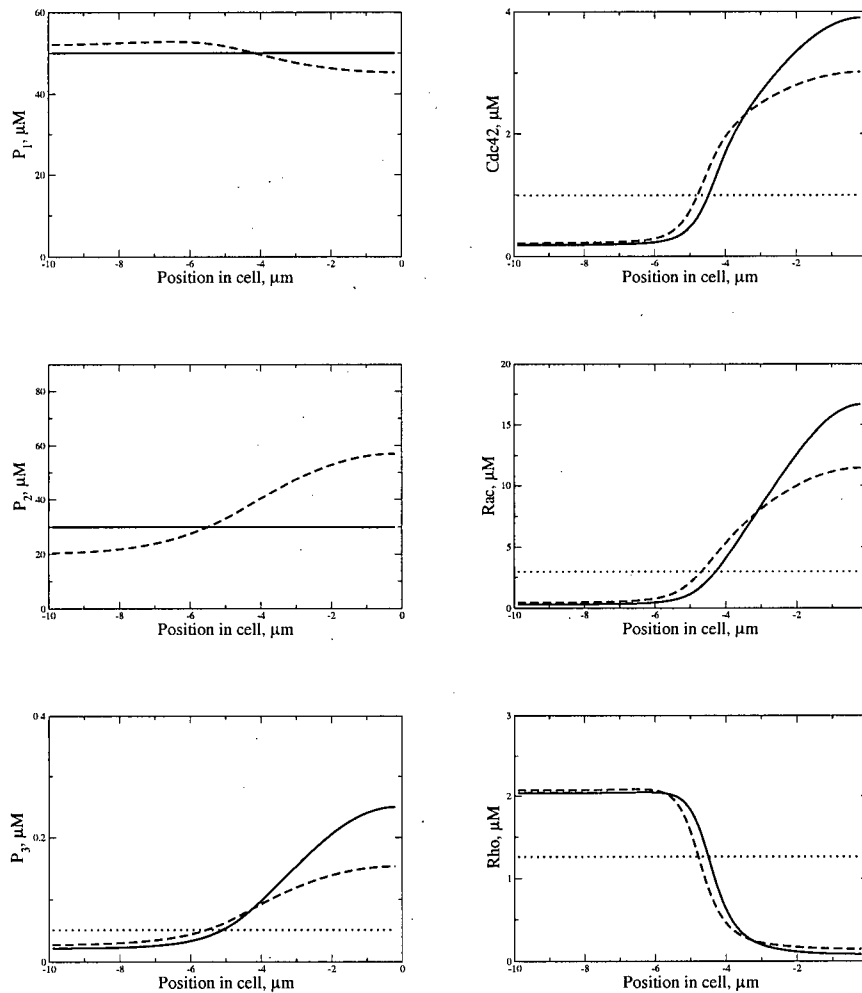


Figure 8.7: Rac-enhanced activity of PI5K or PI3K is required for maintenance of polarity but only Rac-enhanced activity of PI5K is required for persistent directed movement. Gradients in P_1 , P_2 and P_3 concentrations are seen when Rac enhances only PI5K activity (dashed line). When Rac enhances only PI3K activity (solid line), P_3 alone develops a spatially graded profile while P_1 and P_2 do not develop spatially asymmetric profiles. Both (reduced) pathways have little effect on polarization of the Rho proteins. Variables shown are the same as in Figure 8.5.

8.6.4 Asymmetric spatial profiles of PIs and Rho proteins can be reversed in response to a second stimulus

Cells such as neutrophils are able to respond quickly to a change in the position of a chemoattractant source by reorienting and moving in a new direction. Although I am not implementing the model in a more realistic 2D or 3D setting, it is possible to reverse the gradients of the PIs and Rho proteins, to represent such a reorientation, provided the imposed gradient in k_{23} and k_{32} is sufficiently strong and applied for a sufficiently long period of time. For instance, in my model a 100% decrease in k_{23} and k_{32} from front to back must be applied for approximately 15 seconds before the spatial profiles will reverse. If the stimulus is applied for a shorter period of time, the spatial profiles will recover their original distribution. If the stimulus is sufficiently strong, the concentration of PIP₂, PIP₃, Cdc42 and Rac decay from the front and rise in the back with Rho doing the opposite. If the stimulus is removed after PIP₂, PIP₃, Cdc42 and Rac begin to accumulate at the rear of the cell, this reverse asymmetry can be maintained. In this sense, the 1D cell can respond to new (sufficiently strong) stimuli to reverse the direction of motion. In a 2D cell, such reorientation does not require full reversal, and should be easier to achieve.

8.6.5 Cdc42 excludes PTEN by inhibiting activation of Rho

It has been observed in neutrophils that PTEN and active Cdc42 do not spatially colocalize (Li et al., 2003, 2005). As discussed above, I model the activity of PTEN using the term:

$$\frac{k_{32}}{2} \left(1 + \frac{\rho}{\rho_b} \right).$$

In simulations of the full model (Equations (8.3) and (6.2)), PTEN activity is low in areas where active Cdc42 is high (Figure 8.8, top). If Cdc42 does not inhibit Rho, the stable spatial asymmetry of the PIs and small G proteins is lost and PTEN activity is higher than baseline everywhere in the cell (Figure 8.8, bottom). These results suggest that the spatial exclusion of PTEN from areas with active Cdc42 may be due to the inhibition of Rho by Cdc42, providing a possible answer to Question 4. Since Rho has been shown experimentally to activate PTEN (Li et al., 2003, 2005), PTEN activity will be high only in those areas where active Rho is high and Cdc42 low. This result can be tested experimentally by microinjecting resting cells with active Cdc42. If Rho and PTEN are excluded from those areas with high concentrations of Cdc42, this would provide further evidence for mutual inhibition between Cdc42 and Rho and suggest

that Rho spatially regulates PTEN.

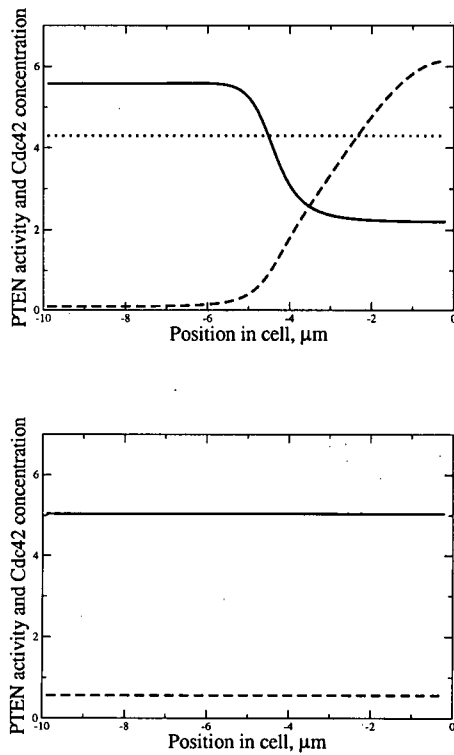


Figure 8.8: Removal of Rho inhibition by Cdc42 does not allow the model to maintain spatially asymmetric distributions of the PIs and Rho proteins and increases the activity of PTEN everywhere in the domain. Top: PTEN activity before (dotted line) and after (solid line) transient application of a graded stimulus. Also shown is the distribution of active Cdc42 after stimulus application (dashed line). Bottom: PTEN activity (solid line) and Cdc42 concentration (dashed line) before and after application of a graded stimulus when Cdc42 does not inhibit Rho activation. This indicates that PTEN activity is suppressed in areas where active Cdc42 is high and elevated in areas where active Cdc42 is low.

8.6.6 PIs and Rho proteins accumulate on one side of the cell in response to two chemoattractant sources

Neutrophils immobilized by latrunculin (which prevents polymerization activity) develop high concentrations of PIP₃, Cdc42 and Rac at both sides of the cell when chemoattractant sources are placed on opposite sides of the cell (Janetopoulos et al., 2004). I can simulate this experiment by modifying the rate constant k_{23} (PIP₂ to PIP₃ conversion) and k_{32} (PIP₃ to PIP₂ conversion) so that k_{23} is maximum at the front and back of the cell and zero in the middle and k_{32} is zero at the front and back and maximum in the middle. In response to this stimulus, the PIs and Rho proteins establish segregated domains with PIP₂, PIP₃, Cdc42 and Rac elevated at the front and Rho elevated at the back. When the stimulus is removed, this spatial segregation is not maintained and the PIs and Rho proteins evolve into the usual bistable distribution with PIP₂, PIP₃, Cdc42 and Rac elevated on one side and Rho elevated on the other (Figure 8.5). A clear front emerges within 20-30 seconds after the stimulus is removed. The side of the cell that becomes the "front" after removal of the stimulus depends sensitively on where the maximum value of k_{32} is placed: if the maximum of k_{32} is placed one grid point off the middle, the side the maximum of k_{32} is closest to will become the front after removal of the stimulus. Figure 8.9 shows the spatial profile of Cdc42 before, during and after the application of two stimuli. Even if it is possible to produce persistent profiles with PIP₂, PIP₃, Cdc42 and Rac elevated at both the front and the back, these distributions would be very unstable. These results suggest that PIs prevent the Rho proteins from establishing multiple domains with high Cdc42 and Rac, as in Figures 6.8 and 7.4, restricting new barbed end creation to the leading edge.

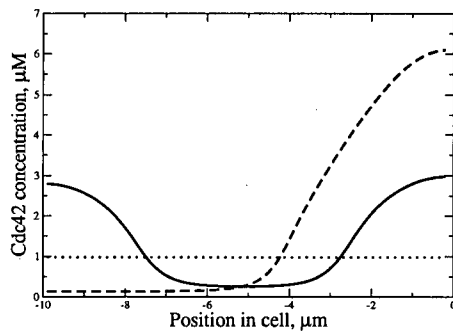


Figure 8.9: Spatial distribution of Cdc42 before (dotted line), during (solid line) and 50 seconds after (dashed line) the application of two stimuli on opposite sides of the cell, as represented by the biochemical rates, k_{23} and k_{32} . While the stimulus is applied, Cdc42 is raised at both the front and back of the cell but once the stimulus is removed, the bimodal distribution cannot be sustained and eventually Cdc42 is elevated only on one side of the cell.

8.6.7 PIs prevent the formation of multiple Cdc42 domains in response to a random stimulus

I showed in Chapter 7 that the Rho protein module when connected to actin dynamics can respond to a random stimulus by establishing multiple stable domains with high Cdc42 and Rac. In the previous section, I showed that a combined model of the PI and Rho protein modules is not capable of maintaining two distinct domains of high Cdc42 and Rac in response to two stimuli. Similarly, the combined PI and Rho protein model cannot establish or maintain more than one domain with high Cdc42 and Rac in response to a random stimulus, as shown in Figure 8.10. This is due to the spatial distribution of the PIs. Since the PIs diffuse faster than the active Rho proteins, the spatial profile of the PIs decays more slowly toward the rear of the cell compared to the Rho protein profile. Since PIP_3 enhances activation of Cdc42 and Rac, this ensures that only one domain of high Cdc42 and Rac is formed in response to a stimulus, random or otherwise. These results suggest that the activity of the PIs helps to establish a "front" and "back" of the cell by integrating spatial information provided by the Rho proteins.

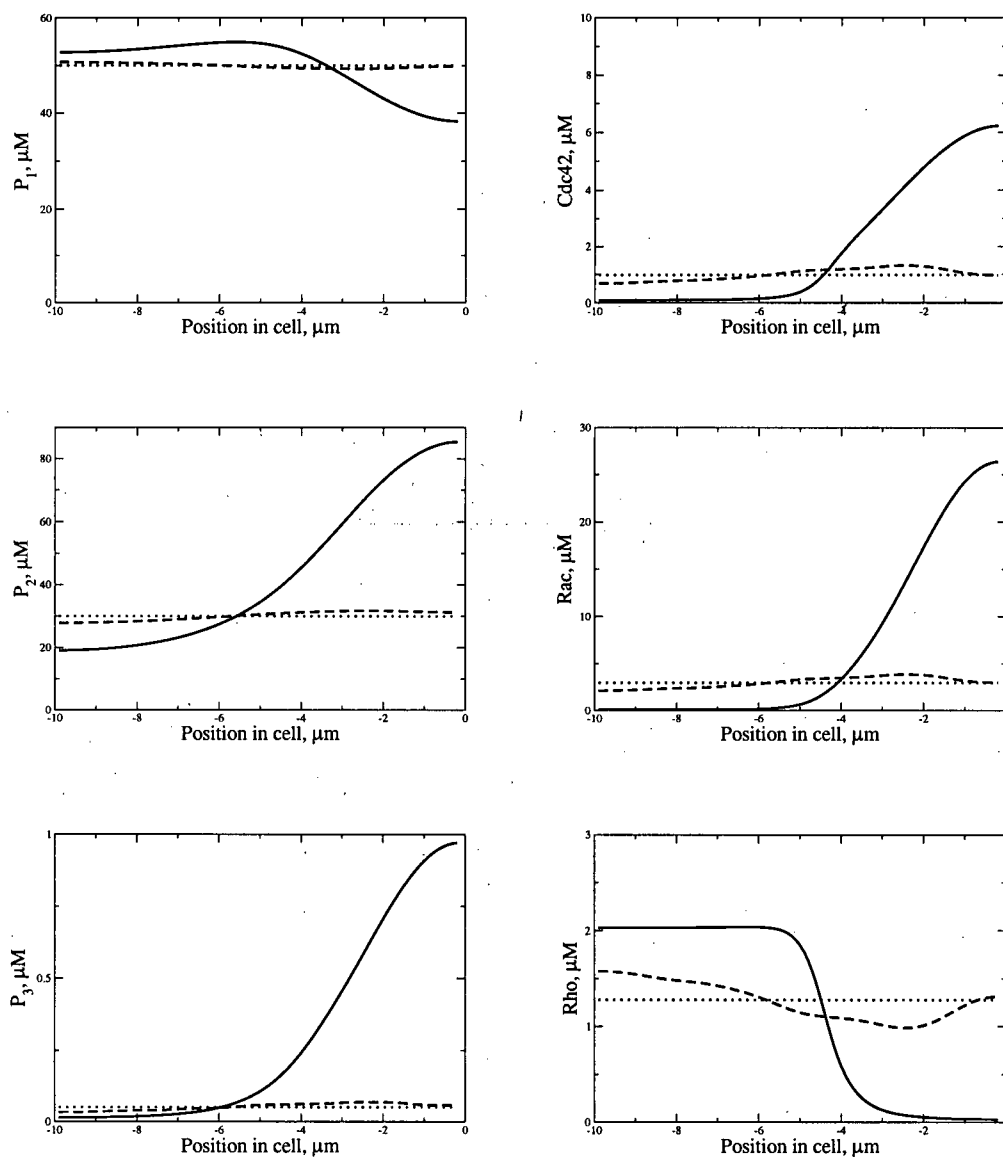


Figure 8.10: PIs prevent establishment of multiple domains of high Cdc42 in response to a random stimulus. Variables shown are the same as in Figure 8.5. Spatial profiles are shown before (dotted line), during (dashed line) and 50 seconds after (solid line) application of the stimulus. Upstream regulation of the Rho proteins by PIs ensures the establishment of a single domain with high Cdc42 at the front of the cell when the cell is exposed to a random stimulus, in contrast to Figures 6.8 and 7.4.

8.6.8 PTEN activation by Rho not necessary to properly sense gradients

In this model, PTEN is elevated in the presence of active Rho but experiments indicate that translocation of PTEN to the rear of the cell is not necessary for directed cell movement and some motile cells do not express PTEN but are still capable of directed movement (Xu et al., 2003). Here I remove Rho activation of PTEN by setting the conversion rate from PIP_3 to PIP_2 , k_{32} , to a constant value everywhere in the cell. As shown in Figure 8.11, the presence of PTEN everywhere in the cell does not prevent PIs and Rho proteins from establishing the appropriate asymmetric spatial profiles in response to a graded stimulus. This suggests that Rho activation of PTEN is not necessary for proper gradient sensing, provided there is some phosphorylation event preventing the unlimited accumulation of PIP_3 (Question 2).

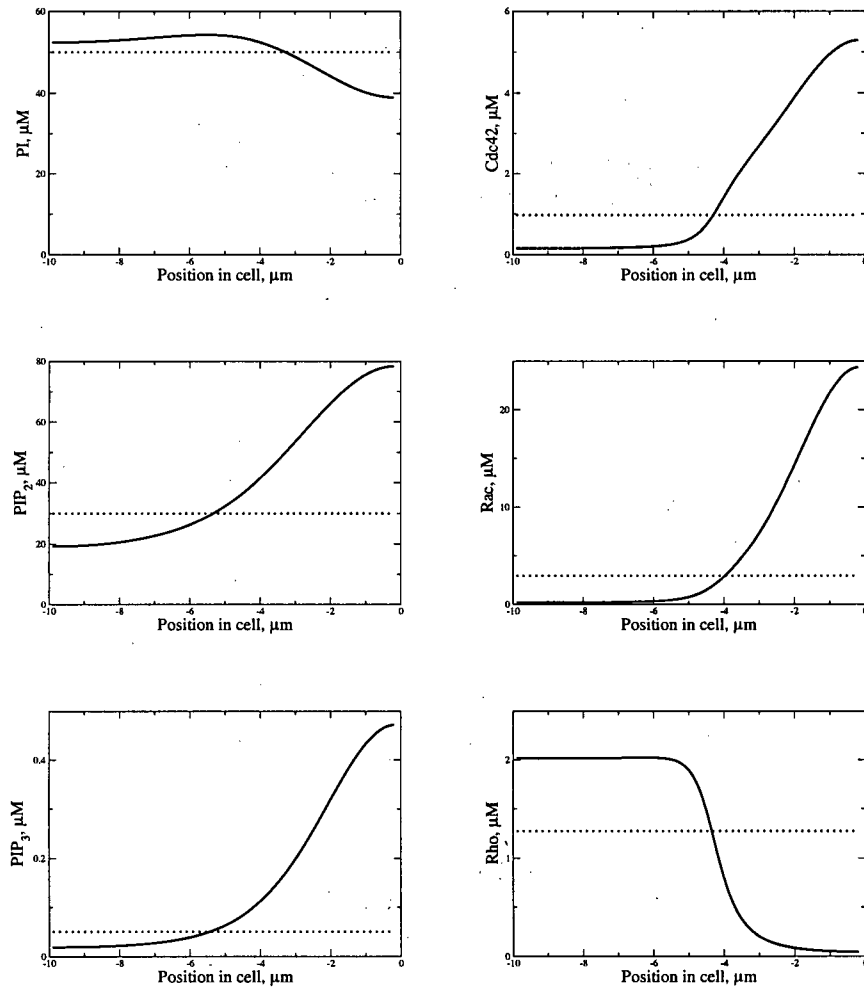


Figure 8.11: PIs and Rho proteins establish and maintain asymmetric spatial gradients when PTEN activity is constant everywhere in the cell. Same variables as plotted in Figure 8.5 showing that Rho activation of PTEN is not required for proper gradient sensing. The spatial profiles of the PIs and Rho proteins when Rho does not enhance the activity of PTEN are stable and consistent with experimental results and previous simulations.

8.7 Summary of results and comparison to previous modelling efforts

As shown by the results in Section 8.6, the model proposed here is capable of capturing many of the same behaviours as previous models, but without assuming unknown interactions or unidentified effectors.

My model is capable of producing stable spatial profiles in response to a graded stimulus (Section 8.6.1). The magnitude of the internal gradients amplifies the gradient of the external stimulus. This is a common feature of all models discussed in Section 8.2. My model is also able to sense a change in the source of the stimulus, provided the signal is sufficiently strong and applied for a sufficiently long time (Section 8.6.4). This is also a feature of the models discussed in Section 8.2, except for those proposed by Meinhardt (1999) and Postma and Van Haastert (2001) where the internal gradients become "locked". Experiments have demonstrated that motile cells remain sensitive to changes in external gradients. This is a feature of motile cells that my model is capable of reproducing.

A number of results deal with specific molecules in the signalling pathway and their role in gradient sensing and directed movement. I showed that PIP₃ activation of Cdc42 (but not Rac, Section 8.6.2) and Rac activation of PI3K or PI5K (Section 8.6.3) is required for proper gradient sensing and maintenance of stable spatial profiles. I investigated the phosphatase PTEN and found that inhibition of Rho by Cdc42 could account for the mutual spatial exclusion of Cdc42 and PTEN (Section 8.6.5) and that PTEN is not required for proper gradient sensing (Section 8.6.8). Since my model takes into account only experimentally determined interactions, I am able to address experimental observations dealing with specific interactions in the signalling pathway. The models discussed in Section 8.2 do not address any of these observations.

I found that two stimuli placed on opposite sides of an immobilized cell can maintain two domains of high Cdc42 and Rac but one side wins after the stimuli are removed (Section 8.6.6). This was first reported experimentally by Janetopoulos et al. (2004) and explored theoretically by Ma et al. (2004). However, the experiments and simulations of the above papers do not address what happens when the stimuli are removed. It would be interesting to observe the cells after the stimuli are removed and compare the results to the predictions of both my model and the model proposed by Ma et al. (2004).

I also investigated the response of the model cell to a random stimulus, with no spatial bias,

which corresponds to exposing a biological cell to a uniform stimulus. As shown in Section 8.6.7, the cell picks a direction and polarizes. The 1D cell in my model is not able to adapt to a uniform stimulus and return to pre-stimulus distributions and concentrations. In several earlier models, Krishnan and Iglesias (2004); Levchenko and Iglesias (2002); Ma et al. (2004), a goal was to model adaptation in response to a uniform stimulus. Using the LEGI modules discussed in Section 8.2, these models display adaptation in response to a uniform stimulus. However, many experiments have shown that cells polarize in random directions and begin moving when exposed to a uniform concentration of chemoattractant (Wedlich-Soldner and Li, 2003). Further experiments are needed to determine if adaptation or random polarization is the dominant response to a uniform stimulus.

8.8 Discussion

This chapter combined the model of Rho proteins discussed in Chapter 6, with a model of phosphoinositides, membrane-associated lipids that also establish asymmetric spatial domains in response to an external stimulus. PIs are known regulators of Rho proteins. PIP_3 has been shown experimentally to interact with and activate Cdc42- and Rac- specific GEFs. This combined model was able to establish and maintain spatially asymmetric profiles in response to a transient stimulus in the conversion rates between PIP_2 and PIP_3 , corresponding to the spatial redistribution of PI3K and PTEN in a stimulated cell. The spatial profiles produced are in agreement with experimentally observed profiles. Feedback between the PIs and Rho proteins is required to establish and maintain these spatial profiles. To simulate the model, I picked parameter values that are consistent with available experimental data (for basal concentrations and approximate time course of redistribution). As this is a proof of principle, rather than a fully accurate quantitative model, consistency with the available data is currently the best that can be achieved as far as parameter estimates. However, the model is insensitive to large variations in the parameter values, suggesting that the model behaviours are not specific to a narrow range of parameters.

I used this model to explore the following features of motile cells. By keeping Cdc42 in an inactive state, the spatial profiles that resulted did not properly reflect the gradient imposed by the stimulus. This is in agreement with experiments indicating that active Cdc42 is required for proper gradient sensing. PIs also appear to smooth out Rho protein profiles as the Rho proteins

are not able to establish and maintain domains with more than one area of high Cdc42 and Rac in response to a random stimulus. This is contrary to the result seen in Chapter 7, when considering only the Rho proteins and actin dynamics.

It was also not possible for Cdc42 to establish two distinct stable domains at the front and back of the cell in response to two stimuli. In the absence of the PIs, Cdc42 can establish two domains that persist after the two stimuli are removed (Chapter 7), but with the addition of the PIs, the two-domain state was unstable, and one of the domains disappeared when the stimuli were removed.

Mutual exclusion of Cdc42 and Rho provides a possible explanation for the recent observations that Cdc42 and PTEN spatially exclude each other. Rho activates PTEN through Rho kinase so areas with high Cdc42 will have low Rho and consequently, low PTEN. The model also supports the experimental observations that a spatial gradient in PTEN is not necessary to maintain spatial asymmetries in the PIs and Rho proteins. The feedback from PIP₃ to Cdc42 and Rac and from Rac to PI5K and PI3K is sufficient to establish and maintain spatial gradients. This model of interactions between PIs and Rho proteins is capable of reproducing many observed behaviours of motile cells. In brief, the PIs act to provide a small internal gradient to the Rho proteins and to select the appropriate spatial pattern of Rho proteins (to avoid the multiple domains shown in Figure 6.6.2).

This chapter explored interactions between two signalling molecules, PIs and Rho proteins, which are both regulators of the actin cytoskeleton. In the next chapter, I combine all three levels of the signalling cascade, PIs, Rho proteins and actin dynamics, to investigate actin regulation in a more complete model of a motile cell.

Chapter 9

Phosphoinositides and Rho proteins cooperate to regulate actin polymerization dynamics in motile cells

In Chapter 3, I developed a model of actin dynamics that included nucleation by Arp2/3, barbed end capping, filament growth and decay. Assuming that biochemical rates that control nucleation, capping, and growth are constant, the model produced spatial profiles of barbed ends and actin filaments that are consistent with experimental observations. In Chapter 7, I connected a model of Rho proteins, effectors that influence certain biochemical rates such as nucleation and capping, to a variant of the actin model. An asymmetric stimulus in Cdc42 resulted in enhanced actin polymerization at the leading edge and initiation of directed motion. The spatial profiles of Rho proteins as well as barbed ends, actin filament density and Arp2/3 were consistent with experimental observations. In Chapter 8, I proposed a model linking Rho proteins with phosphoinositides, lipids that detect external signals and regulate the activation state of Rho proteins. In this chapter, I combine all three of these models to simulate the dynamics of actin, Rho proteins and phosphoinositides in a motile cell. This synthesized model combines three levels of the signalling hierarchy involved in cell motility, from the lipids that detect external signals to the actin dynamics responsible for cytoskeletal remodelling. This model is the first that directly connects PIs and Rho proteins to specific biochemical processes that affect actin dynamics.

9.1 Biological background

Much of the biological background used to develop a model of actin dynamics regulated by PIs and Rho proteins has already been presented. In Chapters 2 and 3, I described how Arp2/3 nucleation, capping, filament growth and decay contribute to the formation of the orthogonal

actin meshwork found in the lamellipodia of motile cells. In Chapter 7, I discussed how the Rho proteins Cdc42, Rac and Rho regulate actin dynamics by modulating the rates of nucleation and capping. In Chapter 8, I presented experimental results indicating that PIs directly regulate Rho protein activation by interacting with GEFs.

In addition to the biological background presented in those chapters, there are further experimental details that will be incorporated into this model.

9.1.1 PIP₂ inhibits capping of barbed ends

The phosphoinositide PIP₂, as discussed in Section 7.1.2, inhibits the association of capping protein with barbed ends of actin filaments (Cicchetti et al., 2002; Ridley, 2001a). In Chapter 7, I assumed that the rate of capping was inhibited by Rac. However, Rac only indirectly regulates the rate of capping, by increasing the concentration of the phosphoinositide PIP₂. In this chapter, I take into account the effect of PIP₂ on the capping rate directly. *In vitro* and *in vivo* experiments demonstrate that PI and PIP₃ have little uncapping activity but PIP₂ uncaps filaments and inhibits the activity of capping protein (DiNubile and Huang, 1997; Schafer et al., 1996). It is not precisely known how PIP₂ inhibits capping but *in vivo* experiments suggest that PIP₂ binds capping protein, preventing it from associating with filament tips. In the model presented here, the rate of capping depends only on the concentration of PIP₂ and not Rac.

9.1.2 PIP₂ enhances activation of Arp2/3

PIP₂, not Cdc42, is required to activate WASp and N-WASp, activators of the Arp2/3 complex (Higgs and Pollard, 2000; Rohatgi et al., 2001). In the presence of both PIP₂ and Cdc42, activation of Arp2/3 is greatly enhanced, (Rohatgi et al., 1999), suggesting that Cdc42 amplifies PIP₂ activation of N-WASp and hence, nucleation by Arp2/3. In Chapter 7, I assumed that Arp2/3 activation was enhanced by Cdc42 and Rac. In this chapter, I use the more accurate assumption that PIP₂ and Cdc42 enhance activation of Arp2/3.

9.1.3 *De novo* actin polymerization is required for maintenance of the PI asymmetry

Blocking actin polymerization in motile cells results in a loss of asymmetry in the PIs, but not in the Rho proteins, suggesting that actin polymerization plays a role in maintaining the PI asymmetry. In one experiment (Srinivasan et al., 2003), cells were treated with latrunculin, a protein

that binds to actin monomers and prevents any polymerization activity despite the availability of free barbed ends. When they exposed the cell to a graded stimulus, the concentration of Rac was elevated at the membrane closest to the stimulus source (the leading edge if the cell were able to move) and this spatial gradient persisted for over 400 seconds. In contrast, PIP₃ was observed to transiently increase at the membrane immediately after stimulus application but the PIP₃ gradient was not maintained. Another experiment exposed moving cells to jasplakinolide, a protein that stabilizes the actin cytoskeleton, causing the pool of actin monomers to be depleted below the critical concentration (Section 2.1.1). Cells exposed to jasplakinolide stopped moving within 1 min and PIP₃ disappeared from the membrane (Wang et al., 2002). Taken together, this suggests that PIP₃ accumulation at the membrane depends on actin polymerization. It is unknown how actin polymerization could influence PIP₃ accumulation and below I speculate how actin polymerization could be linked to PI activity using this model.

9.2 Experimental observations and questions to address

In previous chapters, I explored a number of questions and provided explanations to possibly account for experimental observations. In Chapter 4, I determined that Arp2/3 nucleation occurs most likely through side branching, based on comparisons of spatial profiles of barbed ends and actin filaments with experimental data. In Chapter 7, I demonstrated that a transient stimulus in the rate of Cdc42 activation leads to spatial segregation of the Rho proteins and initiation of directed motion, in agreement with micro-injection experiments. When considering the interaction of PIs and Rho proteins in the absence of actin dynamics in Chapter 8, I showed that active Cdc42 is necessary for proper gradient sensing due to its mutual inhibition of Rho, keeping Rho low at the leading edge. I also showed that mutual inhibition of Cdc42 and Rho may be responsible for the spatial exclusion of PTEN and Cdc42, since PTEN is activated by Rho and Rho is spatially excluded by Cdc42.

However, there are additional questions that can only be addressed by a complete model that incorporates actin dynamics with Rho proteins and PIs. I address the following questions in this chapter:

1. Can a cell polarize, initiate and maintain directed movement in response to intracellular gradients of PI3K and PTEN?
2. Are the spatial profiles of PIs, Rho proteins and actin filaments in response to an external

stimulus consistent with experimental observations?

3. Is it possible to determine what interactions or feedbacks could explain observations that actin polymerization is required to maintain PI asymmetry?

9.3 Model of PIs, Rho proteins and actin dynamics

9.3.1 Model Assumptions

All the assumptions implicit in this model are discussed in Chapters 3 and 7 for the actin model, Chapters 7 and 8 for the Rho protein model and Chapter 8 for the PI model. I make the following changes to the previously proposed models to account for the experimental observations discussed above:

1. The rate of capping is inhibited only by PIP_2 .
2. PIP_2 activates Arp2/3 and this activation is enhanced by Cdc42.

A schematic of the interactions included in the integrated model of actin dynamics, Rho proteins and PIs as suggested by experimental observations is shown in Figure 9.1.

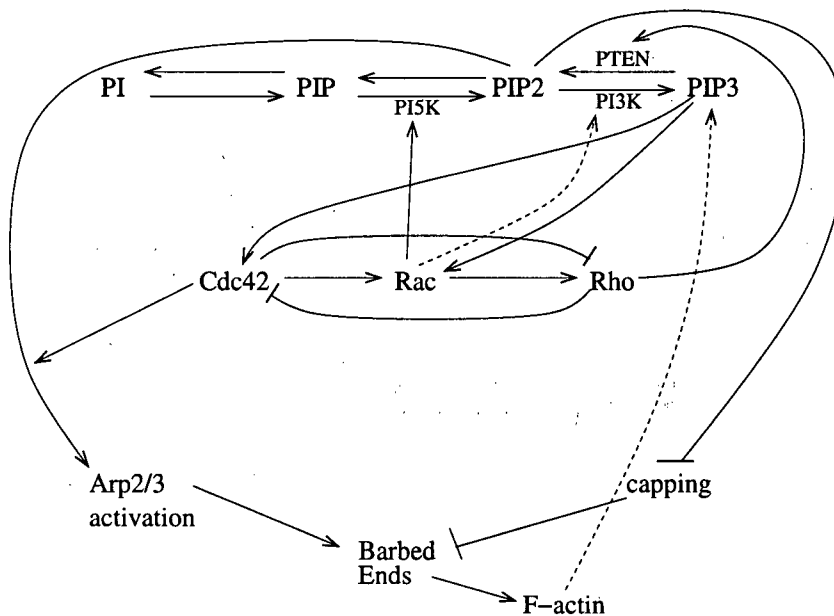


Figure 9.1: Schematic diagram of proposed interactions between the phosphoinositides PI, PIP, PIP_2 and PIP_3 , the Rho proteins Cdc42, Rac and Rho and actin dynamics. Established interactions are shown with a solid line while proposed interactions with an unknown mechanism are shown with a dotted line.

9.3.2 Model equations

I use the same variables as before to denote the various quantities (as set out in Section 3.5 for barbed ends, Arp2/3 and filament density, Section 6.3.1 for the Rho proteins and Section 8.3.1 for the PIs).

The actin equations used here are similar to Equations (7.1) except that I assume PIP₂ is required for Arp2/3 activation (Assumption 2) and that this activation is enhanced by the presence of Cdc42. I also assume that the capping rate is affected by the concentration of PIP₂, not Rac. The equations describing barbed ends, Arp2/3 and actin filament density (B , A , F) are:

$$\frac{\partial B}{\partial t} = k\bar{\eta}(A, F) - \kappa(P_2) - v\frac{\partial B}{\partial x}, \quad (9.1a)$$

$$\begin{aligned} \frac{\partial A}{\partial t} = & \frac{\mu_P}{2} P_2 \frac{P_2^{n_P}}{P_{2half}^{n_P} + P_2^{n_P}} \left(1 + \frac{C}{C_b}\right) \\ & + D_A \frac{\partial^2 A}{\partial x^2} - x'_{edge} \frac{\partial A}{\partial x}, \end{aligned} \quad (9.1b)$$

$$\frac{\partial F}{\partial t} = Bv - F\gamma, \quad (9.1c)$$

where C and P_2 are Cdc42 and PIP₂, μ_P is the rate of PIP₂-mediated Arp2/3 activation and other parameters are as before. P_{2half} is the half-maximal concentration of PIP₂ for Arp2/3 activation (higher than the baseline concentration of PIP₂ to prevent Arp2/3 activation in a resting cell). P_{2b} is the baseline concentration of PIP₂, as discussed in Section 8.4. The capping rate now depends on PIP₂:

$$\kappa = k_{max} - k_R \left(\frac{P_2}{P_{2b} + P_2} \right).$$

The side branching rate is the same as before:

$$\bar{\eta}(A, F) = \frac{\eta A}{K_m + A + lF}.$$

Equations (8.3) are used to describe the PI dynamics while Equations (8.4) describe the Rho proteins.

Parameter values used to simulate these equations are given in Tables 4.1, 6.1 and 8.1. The only new parameters here are μ_P , describing the rate of Arp2/3 activation by PIP₂ and P_{2half} , the concentration of PIP₂ for half-maximal activation of Arp2/3. These parameters were determined by varying their values until numerical results gave the same level of Arp2/3 activation as in Chapter 7. The values used are $\mu_P = 0.011s^{-1}$ and $P_{2half} = 50\mu M$.

Simulations were performed as described in Section 7.5 and 8.5, on a 10 μm domain with a space step of 0.01 μm . To carry out the simulations, all equations were converted to moving coordinates with the membrane located at the origin.

9.4 Results

9.4.1 1D cell model initiates and maintains directed movement in response to spatial gradients of PI3K and PTEN

To simulate the translocation of PI3K and PTEN observed in motile cells exposed to a gradient of chemoattractant, I decreased the rate of PIP₂ to PIP₃ conversion, k_{23} , at the back of the domain and decreased the rate of PIP₃ to PIP₂ conversion, k_{32} , at the front of the cell. The resulting profiles are shown in Figure 9.3. and are all consistent with experimental observations. The magnitude of the spatial profiles is independent of the strength of the stimulus. This is due to the Rho protein crosstalk which establishes stable spatially asymmetric profiles in response to the asymmetric signal transduced by the PIs. The asymmetric gradient of the Rho proteins then maintains the asymmetric profile of the PIs after the stimulus is removed.

Figure 9.2 (left) shows the initiation of motion in response to a stimulus applied at 20 seconds. There is a brief time lag while the spatial asymmetries in the PIs and Rho proteins are established, then Arp2/3 nucleation generates sufficient barbed ends near the leading edge (Figure 9.2 (right)) to push the membrane and initiate motion. The directed motion and spatial profiles are stable and persist after the stimulus is removed. These simulations indicate that our model is capable of producing realistic movement and spatial profiles in response to an internal gradient corresponding to observed PI3K and PTEN gradients in stimulated cells, answering Question 1.

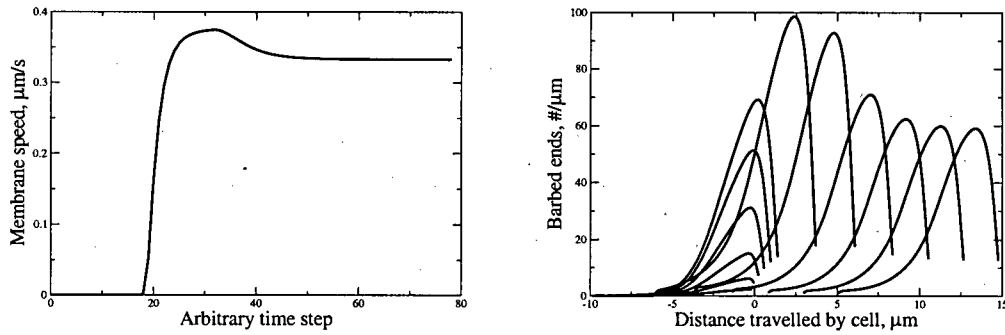


Figure 9.2: Membrane speed (left) and change in barbed end profile (right) over several time intervals, resulting from the application of a transient stimulus to the $\text{PIP}_2 \leftrightarrow \text{PIP}_3$ conversion rates. The time between the plots of the profile barbed ends is variable: 2-4 seconds between profile plots to show the initial rise in barbed ends then 10 seconds between profile plots to show the steady state distribution and motion of the cell.

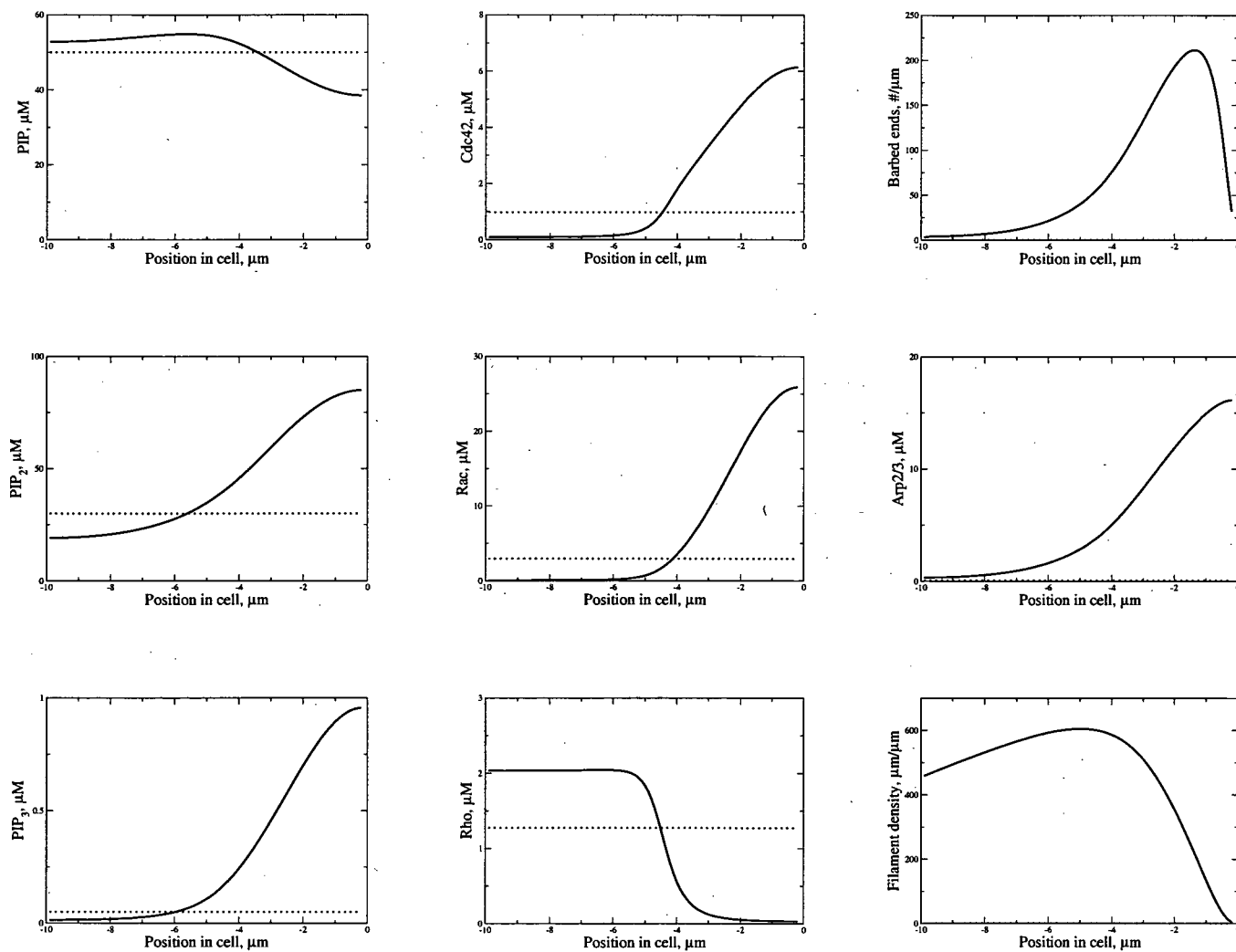


Figure 9.3: Spatial profiles of PIs (left column), Rho proteins (middle column) and barbed ends, Arp2/3 and filament density (right column) in response to a transient stimulus corresponding to intracellular translocation of PI3K and PTEN. The spatial profiles are consistent with experimental observations.

9.4.2 Weak stimulus or short time exposure to stimulus causes delay in initiation of motion

Cells exposed to weak signals (a 1-2% gradient of chemoattractant from the front to back of the cell) are still capable of detecting the gradient and initiating directed motion. Simulations of the model indicate that weak stimuli or stimuli applied for a short period of time result in directed motion after a time delay (Figure 9.4). In Figure 9.4, k_{23} and k_{32} are increased linearly across the length of the cell, from zero to their usual value on opposite sides of the domain. This gradient is applied for differing periods of time (0.1 seconds to the length of the simulation) and the membrane speed is used to determine the onset of directed movement. Stimuli applied for a short period of time (for example 0.1 seconds in Figure 9.4) cause directed motion but after a time delay. Similar results are seen when the gradient in k_{23} and k_{32} is not as steep but the stimulus is applied for the same period of time (not shown).

These simulation results suggest that cells are capable of detecting weak or short lived stimuli but that initiation of motion occurs after a time lag while the spatial asymmetries in the PIs and Rho proteins are established. This result can be experimentally tested by exposing cells to varying concentrations of chemoattractant or quickly decaying chemoattractants and measuring the time it takes for the cells to initiate movement.

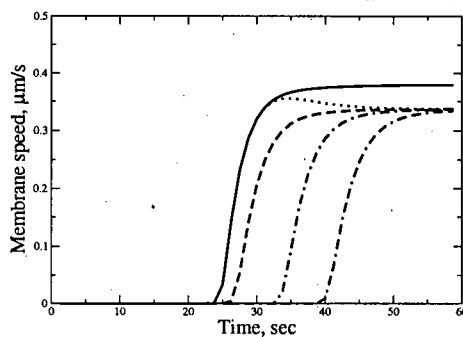


Figure 9.4: Initiation of movement and membrane speed resulting from different stimulus application time lengths. The stimulus was applied at 20 seconds, lasting 0.1 seconds (dot-dash line), 1 second (dashed line) or 10 seconds (dotted line). Also shown is a stimulus that is applied at 20 seconds and remains on for the entire simulation (solid line). Exposure to a brief stimulus results in directed movement with a time delay while stimuli applied for a longer amount of time rapidly initiate movement. Similar results are seen when weak stimuli are applied for a set period of time, resulting in directed motion after a time delay (data not shown).

9.4.3 Polymerization-dependent Rac activation of PI5K and PI3K causes loss of PI asymmetry but not Rho protein asymmetry

Actin polymerization and PI asymmetries

Recent experiments have indicated that actin polymerization is required for maintenance of the PI asymmetry, but not the Rho protein asymmetry in motile cells (Srinivasan et al., 2003; Wang et al., 2002). In Srinivasan et al. (2003), cells are exposed to latrunculin, a protein that sequesters actin monomers and halts polymerization activity. Latrunculin-treated cells lose their cytoskeletal structure since filaments cannot elongate but continue to decay; monomers lost by depolymerization are quickly bound by latrunculin. When a treated cell is exposed to a chemoattractant, Rac, but not PIP₃, is increased at the leading edge in response to a stimulus (although the cell can not initiate movement due to a lack of polymerization). Since barbed ends are not affected by this treatment, this suggests that existing F-actin or polymerization dynamics are necessary for enhancing PIP₃ accumulation at the leading edge.

However, in another experiment, moving cells are exposed to jasplakinolide, a protein that stabilizes actin filaments (Wang et al., 2002). Cells exposed to jasplakinolide have their cytoskeleton "frozen", meaning that monomers are not recycled back into the cytoplasmic monomer pool where they would be made available for polymerization. Polymerization of free barbed ends quickly uses up the available monomers, causing the monomer concentration to fall below the critical concentration. Crawling cells exposed to jasplakinolide stopped moving within 1 min and lost PIP₃ at the membrane. This suggests that it is actin polymerization and not F-actin or free barbed ends that is necessary to maintain PIP₃ accumulation at the leading edge.

Parameter dependence on actin polymerization

To test the hypothesis that actin polymerization is involved in maintaining the PI asymmetry in motile cells, I modified the terms regulating Rac activation of PI5K, k_{12} , and PI3K, k_{23} . As discussed above, it appears that actin polymerization is required for Rac-mediated activation of PI3K to maintain a gradient of PIP₃ in a motile cell. I demonstrated in Chapter 8 that Rac activation of PI5K or PI3K will lead to a spatially asymmetric profile in PIP₃, suggesting that actin polymerization is required for Rac activation of both PI5K and PI3K in this model. I modify the PI equations so that the activity of PI5K and PI3K is enhanced by Rac only when active polymerization is taking place. In the quasi-steady state term that expresses the activity of PI5K and PI3K in terms of the Rac concentration (Section 8.3.3), I include a sigmoidal term

that prevents Rac from enhancing phosphorylation if there are no free barbed ends or actin monomers available for polymerization. The conversion rates k_{12} and k_{23} are now expressed as follows:

$$k_{12} \left(1 + \frac{R}{R_b} \frac{(Bv_t)^{n_b}}{(B_0v)^{n_b} + (Bv_t)^{n_b}} \right),$$

$$k_{23} \left(1 + \frac{R}{R_b} \frac{(Bv_t)^{n_b}}{(B_0v)^{n_b} + (Bv_t)^{n_b}} \right).$$

where v_t is the rate of polymerization and B is the current number of barbed ends in a treated cell. v is the rate of free polymerization in an untreated cell ($v = 0.5\mu\text{m/s}$) and B_0 is the half-maximal number of barbed ends for Rac activation of PI5K and PI3K. I choose B_0 very small ($B_0 = 0.1\mu\text{m}^{-1}$) so that even very little polymerization activity will allow Rac to enhance PI5K and PI3K activity. This sigmoidal term prevents Rac from activating PI5K and PI3K if there are no actively polymerizing filament tips ($B = 0\mu\text{m}^{-1}$) or if monomers are not available for polymerization because they are sequestered or below the critical concentration ($v_t = 0\mu\text{m/s}$). The choice of a sigmoidal function here is arbitrary; I achieve similar model results when I use a Michaelis-Menten or linear term. I use a sigmoidal function to provide switch-like behaviour so that Rac maximally enhances PI5K and PI3K activity even in the presence of very few barbed ends or actin monomers. Future experiments exploring the role of actin polymerization in the maintenance of PI asymmetry may clarify what form of interaction is more appropriate.

After incorporating these new conversion terms into the model, I simulated both the latrunculin and jasplakinolide experiments by modifying the current rate of polymerization. For latrunculin treated cells, I assumed $v_t = 0$ while for jasplakinolide treated cells, I used $v_t = \exp(-Kt)$ to simulate the gradual loss of actin monomers from continued polymerization. As shown in Figure 9.5 (simulations of latrunculin treated cells), a slight asymmetry is possible during the application of the stimulus but the asymmetry in the PIs is not maintained. In contrast, an asymmetry in the Rho proteins is established and maintained. The cell is not able to initiate motion since the PIP_2 concentration is not sufficiently high to activate Arp2/3. Similar results are achieved in simulations of jasplakinolide treated cells (not shown).

It is not clear how actin polymerization may be responsible for the activation of PI5K and PI3K as suggested here. Perhaps the ATP-actin cap on the newly polymerized portion of a filament provides a substrate needed by Rac to interact with PI5K and PI3K. Perhaps phosphates released during ATP-actin hydrolysis are used by Rac to activate PI5K and PI3K.

Treating motile cells with capping proteins to prevent actin polymerization without depleting or sequestering the monomer supply would provide experimental verification of the mechanism suggested here. If a gradient of PIP_3 is not established in response to a stimulus in a cell treated with capping protein, that would provide further evidence that activation of PI5K and PI3K depends somehow on actin polymerization.

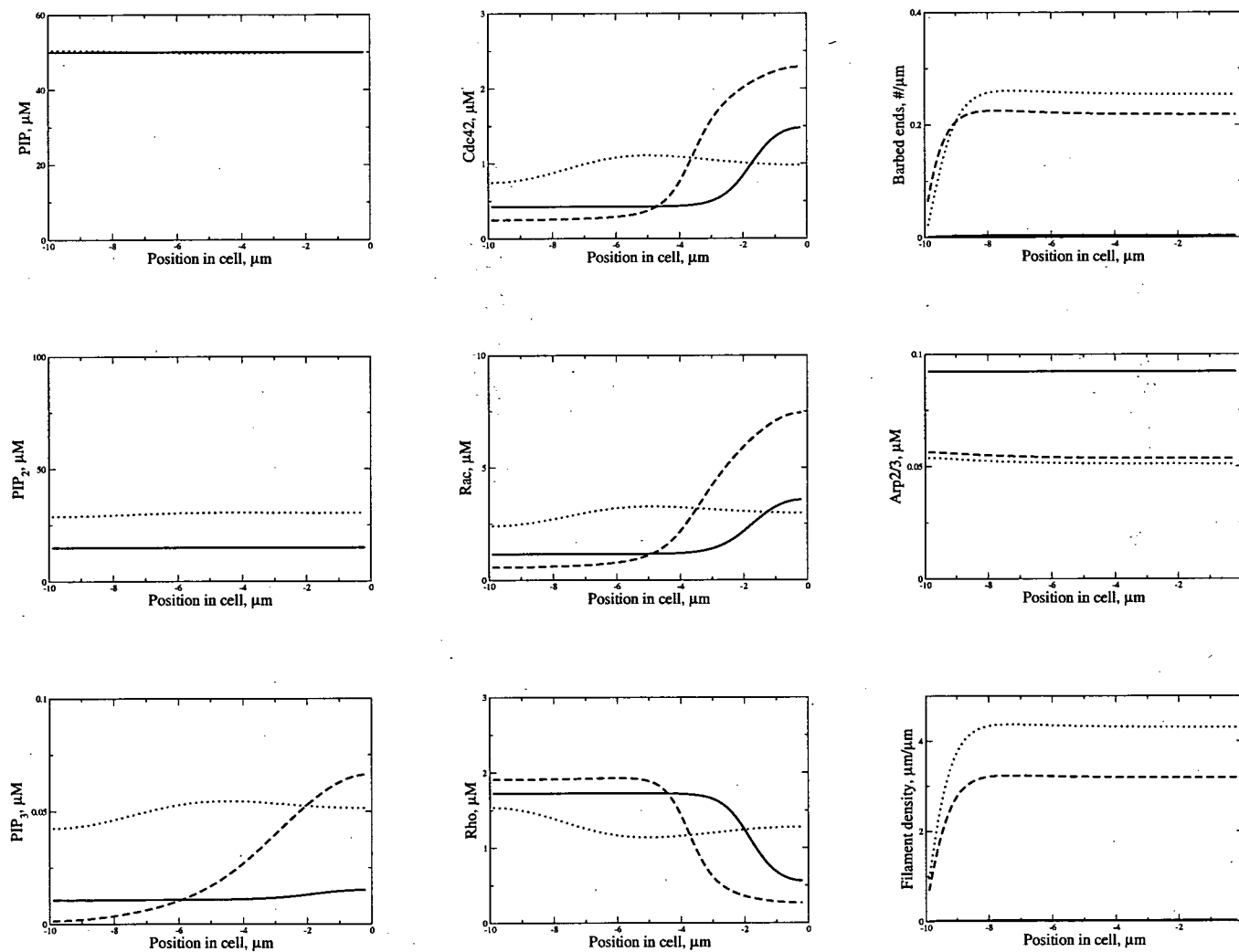


Figure 9.5: Spatial asymmetries in PIs and directed motion are not maintained in latrunculin treated cells if PI5K and PI3K activation relies on actin polymerization (see Section 9.4.3). Variables shown are the same as in Figure 9.3. Also shown is the spatial profile during stimulus application (dashed line). Rho proteins are able to establish and maintain a spatial asymmetry in response to a stimulus, which is consistent with experimental observations.

9.5 Discussion

The goal of this thesis has been to develop a multi-layered model that simulates the signalling cascade that occurs when an external signal induces a spatial gradient in PI3K and PTEN. In a motile cell, PI3K and PTEN cause a spatial gradient in phosphoinositides, membrane bound lipids that are required for detection of external signals. The phosphoinositides generate a spatial asymmetry in the Rho proteins by activating specific GEFs. To simulate the effect of the PIs on Rho protein activation, I assume the local concentration of PIP_3 modifies the activation rate of Cdc42 (I_c) and Rac (I_r). Crosstalk between the Rho proteins amplifies the asymmetry projected by the PIs and establishes stable spatial domains that are independent of the strength of the external signal. The Rho protein module continues to reach down to affect the actin cytoskeleton but also reaches back up the signalling cascade to further reinforce and maintain the spatial asymmetry initiated by the external signal through PI3K and PTEN. The Rho proteins, and to a lesser extent the PIs, direct actin polymerization by influencing biochemical rates. This causes the actin cytoskeleton to reorganize, producing new barbed ends close to the leading edge through Arp2/3 nucleation and inhibition of capping, while polymerization activity is suppressed in other parts of the cell. Through an as yet unknown mechanism, actin polymerization appears to feed back onto the top layer of the cascade, promoting the PI asymmetry at the cell membrane. These asymmetries in signalling molecules and actin dynamics allow a motile cell to polarize and maintain a distinct "front" and "back". Without this polarization, a cell would not be able to correctly interpret a gradient of chemoattractant and would, at best, initiate motion in a random direction. This would have disastrous consequences, as, for instance, neural development would be impaired and neutrophils could not effectively chase down and engulf invading bacteria.

In the next chapter, I summarize the results presented in this thesis, discuss implication for our understanding of cell motility and suggest ways this work can be expanded and improved.

Chapter 10

Results and discussion

In my thesis, I have studied each component of three signalling modules individually, characterized the modules themselves, and then assembled an integrated model linking these modules together. My assumptions are based on experimentally established interactions.

10.1 Model of actin dynamics

In Chapter 3, I proposed a model for actin dynamics that kept track of barbed ends, Arp2/3 and filament density, where I assumed Arp2/3 is activated only at the leading edge. Under the simplifying assumption that Arp2/3 spontaneously nucleates new barbed ends, it was possible to find an analytic solution to describe the spatial profile of barbed ends, Arp2/3 and filament density. By assuming that actin filaments cause edge protrusion by a thermal ratchet mechanism, it was possible to determine an implicit expression for the membrane speed. The spatial profiles and membrane speed predicted using biologically reasonable parameter values were consistent with experimental results. In Chapter 4, I extended the actin model to cases that are not easily solved analytically. Simulations allowed me to explore the behaviour of the model under different conditions and revealed how the membrane speed depends on biochemical rates. Side branching provided the best fit to experimental data, in agreement with recent theoretical and experimental investigations. I expanded the model in Chapter 5 to include retrograde flow, a small rearward flow of the actin meshwork observed in lamellipodia of motile cells. At the rates typical of fast moving cells, retrograde flow has little effect on the spatial profiles or membrane speed, as predicted by the model.

10.2 Model of Rho proteins and actin dynamics

In the actin model explored in Chapters 3-5, I assumed that rate constants governing biochemical processes are constant. Rho proteins regulate actin dynamics by adjusting biochemical rates. In Chapter 6, I reviewed a model of Rho protein crosstalk proposed in Jilkine (2005) and Marée

et al. (2006) which established stable spatial domains in response to a graded stimulus. I then linked this Rho protein module to a model of actin dynamics in Chapter 7, based on known effects of the Rho proteins. The stable spatial asymmetry in the Rho proteins led to spatial regulation of actin dynamics, causing an increase in the number of barbed ends near the leading edge. These barbed ends exert force on the membrane and the cell initiates movement. The spatial profiles and membrane speeds produced by this intermediate model are consistent with experimental observations.

10.3 Model of PIs and Rho proteins

Rho proteins form the middle layer of the signalling cascade and are regulated by phosphoinositides. Phosphoinositides are the first intracellular signalling molecule to establish a spatial gradient in response to an external signal and, in doing so, start the entire signalling cascade that eventually leads to directed movement. PIs communicate the external gradient to the Rho proteins by altering their activation dynamics, explored in Chapter 8. I found that while the PIs are unable to maintain a gradient in the absence of the Rho proteins, feedback from the Rho proteins to the PIs ensures that a stable spatial asymmetry is maintained, even when the stimulus is withdrawn. PIs smooth out the response of the Rho proteins, preventing Rho proteins from establishing more than one domain of high concentration in response to a random stimulus. This model suggests that Cdc42 is required for proper gradient sensing by establishing spatial profiles that lead to the formation of a leading edge in the appropriate area of the cell.

10.4 Model of PIs, Rho proteins and actin dynamics

Chapter 9 integrated all three modules of the signalling cascade: PIs, Rho proteins and actin dynamics. Experimentally determined interactions between all three modules were used to create a single interconnected system. I found that this system could initiate and maintain directed motion and stable spatial profiles in response to a transient gradient. Simulations produced spatial profiles and membrane speeds consistent with observations of live cells. Experimental observations suggest that Rho protein feedback to the PIs depends on actin polymerization. When I incorporated this into the model, I found that I could explain how a decrease in filament growth could decrease Rac-mediated kinase activity. This suggests that actin polymerization may be actively involved in maintaining and reinforcing the spatial asymmetries of PIs in a

motile cell.

10.5 Discussion of general questions posed in Chapter 2

These results allow me to address the questions posed in Chapter 2.

1. How do we begin to understand these pathways that signal to actin?

As shown in Figure 1.5, there are many signalling cascades that are activated in response to an external signal. I believe that considering modules of these large signalling cascades in isolation and then connecting a small number of them together in a biologically reasonable way is an important step in understanding these large signalling pathways.

In particular, I have shown that crosstalk in the Rho protein module is the key to maintaining spatially asymmetric spatial profiles of Rho proteins and PIs, which restricts new barbed end formation and actin polymerization to the leading edge. The PI module cannot maintain spatially asymmetric profiles in the absence of feedback from the Rho proteins, but PIP₃-mediated activation of Cdc42 is required for proper gradient sensing. Feedback within and between PIs, Rho proteins and actin dynamics gives rise to directed motion and the spatial profiles seen in motile cells.

2. Is it possible to identify modules that are involved in cell motility?

From all the interacting modules in these large signalling cascades, I focussed on several modules that I felt were crucial for directed cell movement, based on experimental evidence. While I omit a large number of signalling molecules, the model presented here, consisting of three interacting modules of PIs, Rho proteins and actin dynamics (relying only on experimentally verified interactions and observations), is able to produce polarization and movement that is consistent with experimental evidence (Chapter 9). This suggests these specific modules are crucial for cell motility and play a central role in actin regulation.

3. How do these modules behave and how are they linked?

The answer to this question formed the main focus of my thesis. In Chapters 3 and 4, I found that side branching by Arp2/3 produced the spatial profiles most closely in

agreement with experimental data. In Chapter 8, I found that Rho proteins and PIs are capable of establishing asymmetric spatial profiles in response to a graded stimulus. In Chapter 9, I connected all three of these modules using experimentally determined interactions. The PIs, whose spatial asymmetry is maintained through interactions with the Rho proteins, spatially regulate actin polymerization by enhancing Arp2/3 nucleation and inhibiting capping. While it is not clear how the interaction may occur, I also suggest how actin polymerization could be related to the maintenance of the Rac-mediated PIP₃ asymmetry. While all three of these modules produce distinct behaviours in isolation, connecting them into one unified interacting system reinforces the spatial profiles and ensures persistent movement even when the stimulus is removed.

4. How do biochemical rates and spatial distribution of signalling molecules affect the speed of a cell and the spatial distribution of actin filaments?

Biochemical rates have a profound effect on cell speed and the spatial distribution of actin filaments, as shown in Chapters 4, 7 and 9. Spatial regulation of Arp2/3 nucleation and capping by upstream effectors such as PIP₂ ensures that freely polymerizing barbed ends are restricted to the front of the cell. This allows a motile cell to promote actin polymerization at the leading edge, causing the characteristic spatial profiles and speed. Without a spatially graded profile of PIP₂, barbed ends would be found everywhere in the cell, depleting the pool of monomers and producing membrane protrusions in inappropriate areas of the cell. Thus, both the magnitude as well as the spatial regulation of biochemical rates are important for producing biologically reasonable spatial profiles and cell speeds that are typical of fast moving cells such as keratocytes.

5. Which signalling cascades or direct or indirect feedback loops or interactions could lead to spatially stable actin profiles?

To answer this question, I look to the results presented in several chapters. In Chapters 3 and 4, a simple model of actin polymerization was able to produce spatially stable actin profiles in the form of travelling wave solutions. This investigation was expanded in Chapter 7 to include Rho proteins. Rho protein crosstalk allowed the Rho proteins to maintain stable asymmetric profiles even when the stimulus is removed. These asymmetric profiles ensured that actin polymerization was enhanced only at the leading edge, leading to

persistent movement. In Chapter 9, PIs were added to the model of Rho protein and actin dynamics. PIs are required to transduce the initial asymmetric signal to the Rho proteins, causing the Rho proteins to establish asymmetric spatial profiles. The Rho proteins then feedback onto the PIs and actin dynamics, leading to persistent spatial profiles.

6. Which interactions within and between modules are crucial for cell motility?

Based on the results presented in Chapter 8, it is clear that PIP_3 activation of Cdc42 (but not Rac) is required to establish asymmetric Rho protein gradients that are oriented in the proper direction and that Rac activation of PI5K or PI3K is required to maintain an asymmetric distribution of PIP_3 . Within the Rho protein module itself, mutual inhibition of Cdc42 and Rho is required to maintain persistent spatial gradients of the Rho proteins and, through signalling to the PIs, persistent spatial gradients of PIs and actin filaments (Chapter 9). Finally, PIP_2 localized actin dynamics to the leading edge by enhancing Arp2/3 activation and inhibiting capping. Based on the models presented here, I conclude that these are the crucial interactions to produce directed movement.

An updated schematic showing the interactions discussed here is shown in Figure 10.1. The numbers associated with each arrow refer to citations listed in the caption, indicating experimental papers where the particular interaction is observed and discussed. Please see the relevant chapters for further details about these interactions.

10.6 Experimentally testable predictions

The models presented here provide explanations for a variety of experimental observations, such as defects in gradient detection in cells lacking Cdc42 and proper directed motion in cells lacking PTEN. Based on the model results, I propose the following experimentally testable predictions to either validate the model and provide further insight into signalling cascades that regulate actin polymerization in motile cells or uncover behaviours of the model that are not consistent with real cells.

In Chapter 8, I explored interactions between PIs and Rho proteins. In particular, I showed that mutual inhibition of Cdc42 and Rho could account for observations showing that Cdc42 and PTEN spatially exclude each other. Rho activates PTEN through Rho kinase (ROCK) so that spatial exclusion of Rho by Cdc42 will also lead to the spatial exclusion of PTEN. Based

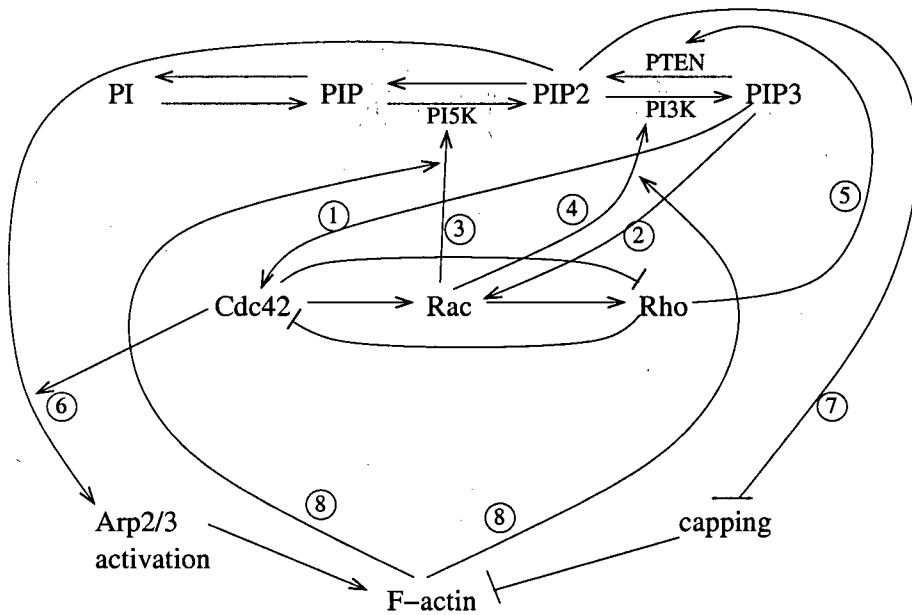


Figure 10.1: Updated schematic of interactions between PIs, Rho proteins and actin dynamics, showing all interactions considered in this thesis. The following are citations associated with each arrow. (1): Aoki et al. (2005); Li et al. (2003); Ma et al. (1998). (2): Aoki et al. (2005); Welch et al. (2002). (3): Toliyas et al. (2000); van Hennik et al. (2003), (4): Aoki et al. (2005); Weiner et al. (2002); Welch et al. (2003). (5): Li et al. (2005). (6): Higgs and Pollard (2000); Rohatgi et al. (1999, 2001). (7): DiNubile and Huang (1997); Schafer et al. (1996). (8): Srinivasan et al. (2003); Wang et al. (2002).

on the model, an experiment where active Cdc42 is microinjected into a resting cell should lead to spatial exclusion of both Rho and PTEN. This would provide evidence for mutual inhibition of Cdc42 and Rho in Rho protein crosstalk (not mutual inhibition of Rac and Rho) and the role of Rho in spatially regulating PTEN activity.

Chapter 9 combined all three modules in an interconnected model to simulate polarization and initiation of directed movement. In Section 9.4.2, I showed that a stimulus causes the cell to polarize, leading to directed motion after a time delay. This time delay increases as the stimulus becomes weaker or shorter lived. An experiment that measures the time taken for a cell to initiate movement in response to different gradients of chemoattractant, or gradients of chemoattractant that decay after a short period of time, would confirm the simulation results. This experiment would also provide a time course for initiation of motion in response to a stimulus that can be compared with the time course predicted by the model.

In Section 9.4.3, I proposed a mechanism that would prevent Rac-mediated activation of PI5K and PI3K in the absence of *de novo* actin polymerization. Simulation results of this

model were consistent with experimental observations and suggest that actin polymerization is required for maintenance of PI spatial asymmetries. Previous experiments modified the concentration of actin monomers available for polymerization, either by sequestering with latrunculin or by preventing filament depolymerization with jasplakinolide. To test the role of barbed end polymerization in PI5K and PI3K activation, I suggest introducing capping protein into motile cells, either by permeabilization or by microinjection. This experiment would not alter the concentration of available monomers but would prevent polymerization by making barbed ends unavailable. My model predicts that a PIP_3 asymmetry could not be maintained in a treated cell exposed to a gradient of chemoattractant.

10.7 Main results

During my exploration of actin polymerization, PI and Rho protein dynamics by assimilating the available experimental literature and simulating the models proposed here, I gained some insights into how directed cell movement is regulated.

It has been demonstrated that PIP_3 influences both Cdc42 and Rac activation but it was not clear if both Cdc42 and Rac must be activated for proper gradient sensing. Using my model, I discovered that only PIP_3 activation of Cdc42 is required to properly establish asymmetric spatial profiles of Rho proteins and PIs. If PIP_3 activates only Rac, the cell is able to polarize but cannot properly detect the gradient.

To maintain the spatially asymmetric profiles, mutual inhibition of Cdc42 and Rho is required. This Rho protein crosstalk is the key to maintaining asymmetric distributions of PIs and Rho proteins after a stimulus is removed, ensuring persistent cell movement by restricting actin polymerization to the leading edge. According to the models presented here, Rho protein crosstalk is also responsible for gradient amplification, discussed in Chapter 1. The magnitude of the Rho protein profiles is independent of the stimulus strength, allowing the cell to respond in a uniform way to different signals. Feedback from Rac to the kinases PI5K and PI3K is necessary to maintain an asymmetry in the PIs, and PIP_2 activation of Arp2/3 and inhibition of capping proteins restricts new barbed end creation and actin polymerization to the leading edge.

Rho protein crosstalk is required for persistent motion, but the interplay between PIs, Rho proteins and actin dynamics is essential for the establishment of polarity and the stable spatial

profiles that are characteristic of motile cells.

10.8 Model limitations

The models developed here represent a beginning in the study of cell motility and regulation of actin polymerization by PIs and Rho proteins. In order to study the PI, Rho protein and actin modules, I imposed a number of limitations on the models proposed in this thesis. Despite these limitations, I believe these models provide a foundation for future theoretical explorations.

The models here are simplifications of the actual processes that occur in live cells. Since many details about biochemical processes are not known, I modelled these processes using linear kinetics. While this is the simplest possible approach and restricts the number of parameters that need to be estimated, it is likely that interactions in cells follow more complicated kinetics, such as Michaelis-Menten or other saturating kinetics.

The models presented in this thesis deal with a limited number of interacting molecules. Not all molecular components are taken into account, such as those shown in Figure 1.5, meaning that some possibly important interactions have been overlooked.

I also did not consider stochastic effects of individual molecules. For many molecules, such as Rho proteins, the concentration is sufficiently high that a continuum model may be appropriate. However, PIs are not highly abundant, particularly PIP_3 , and active Arp2/3 is found at a very low concentration in resting cells and immediately after stimulation. For these molecules, stochastic effects may be important and a stochastic model may be more appropriate for modelling their activity.

I implemented all these models in 1D, which assumes the actin meshwork in lamellipodia are homogeneous and ignores edge effects where membrane geometry and adhesion may play a more important role. I also assumed all filaments are oriented toward the leading edge, imposing a directionality on the model cell. I am unable to model the initial organization of the actin meshwork in lamellipodia from randomly oriented filaments into an orthogonal mesh. I cannot take into account spatial inhomogeneities in molecular distributions, such as the clustering of PIs into lipid rafts (Meiri, 2005).

10.9 Future work

By investigating the components of the signalling cascade involved in cell motility individually before assembling them into one complex model, I gain a better understanding of what each of the layer in the cascade can accomplish on their own and how feedback from other parts of the cascade can suppress or reinforce certain behaviours. This model lays the foundation for greater understanding of the regulation of actin polymerization in motile cells. Future work can refine this model by explicitly incorporating molecules that regulate the phosphorylation state of the PIs or the activation state of the Rho proteins. The actin model could be expanded to keep track of capped filaments, making it possible to determine an average filament length and incorporating the uncapping activity of PIP_2 .

In the actin model, it was assumed that all filaments are oriented toward the leading edge. By simulating this model in 2D or 3D, it would be possible to consider the effect of filament orientation on protrusion speed and lamellipodium formation. Part of this has already been done: in Marée et al. (2006), a model of actin dynamics and Rho proteins similar to the one presented in Chapter 7 was simulated in a 2D cell. This model used a Cellular Potts model (Graner and Glazier, 1992; Ouchi et al., 2003) to integrate the shape changes and motility of a keratocyte-like cell in 2D. As shown in Figure 10.2, simulations of this model cause a stimulated cell (bottom) to change shape from a rounded resting cell to a crescent shaped cell that moves at a biologically reasonable speed (inset plot). A resting cell (top) remains in a rounded shape and does not initiate movement in any direction. Based on my work here, a future step will be to include PIs in this model as upstream regulators of the Rho proteins.

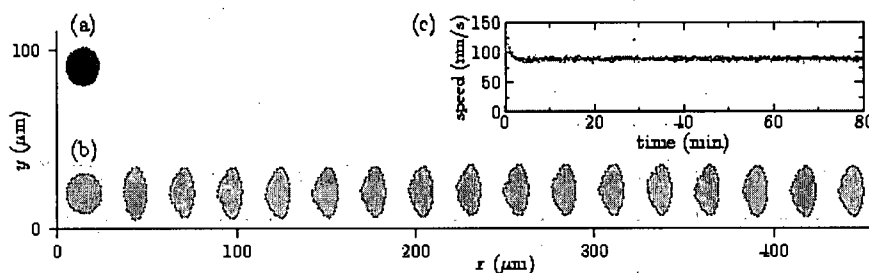


Figure 10.2: Simulations of Rho protein and actin dynamics in a 2D model cell, reprinted with permission from Marée et al. (2006). An unstimulated cell (top) remains stationary while a cell exposed to a stimulus (bottom) changes from a rounded resting cell to a crescent shaped motile cell. The model cell moves at biologically reasonable speeds (inset) and spontaneously takes on a shape similar to a keratocyte.

The models developed here present a starting point for future investigations into cell motility. By considering the components of the signalling cascade separately and together, I have gained a better understanding of actin polymerization regulation in motile cells and insights into some of the characteristics of motile cells.

Bibliography

VC Abraham, V Krishnamurthi, DL Taylor, and F Lanni. The actin-based nanomachine at the leading edge of migrating cells. *Biophysical Journal*, 77(3):1721–1732, SEP 1999.

JC Adams. Cell-matrix contact structures. *Cellular and Molecular Life Sciences*, 58(3):371–392, MAR 2001.

KJ Amann and TD Pollard. Direct real-time observation of actin filament branching mediated by Arp2/3 complex using total internal reflection fluorescence microscopy. *Proceedings Of The National Academy Of Sciences Of The United States Of America*, 98(26):15009–15013, DEC 2001.

K Aoki, T Nakamura, K Fujikawa, and M Matsuda. Local phosphatidylinositol 3,4,5-trisphosphate accumulation recruits Vav2 and Vav3 to activate Rac1/Cdc42 and initiate neurite outgrowth in nerve growth factor-stimulated PC12 cells. *Molecular Biology Of The Cell*, 16(5):2207–2217, MAY 2005.

A Arcaro. The small GTP-binding protein Rac promotes the dissociation of gelsolin from actin filaments in neutrophils. *Journal Of Biological Chemistry*, 273(2):805–813, JAN 1998.

M Bailly, F Macaluso, M Cammer, A Chan, JE Segall, and JS Condeelis. Relationship between Arp2/3 complex and the barbed ends of actin filaments at the leading edge of carcinoma cells after epidermal growth factor stimulation. *Journal of Cell Biology*, 145(2):331–345, APR 1999.

M Bailly, I Ichetovkin, W Grant, N Zebda, LM Machesky, JE Segall, and J Condeelis. The F-actin side binding activity of the Arp2/3 complex is essential for actin nucleation and lamellipod extension. *Current Biology*, 11(8):620–625, APR 2001.

JR Bamberg. Proteins of the ADF/cofilin family: Essential regulators of actin dynamics. *Annual Review of Cell and Developmental Biology*, 15:185–230, 1999.

- MM Bird, G Lopez-Lluch, AJ Ridley, and AW Segal. Effects of microinjected small GTPases on the actin cytoskeleton of human neutrophils. *Journal Of Anatomy*, 203(4):379–389, OCT 2003.
- GM Bokoch, CJ Vlahos, Y Wang, UG Knaus, and AE TraynorKaplan. Rac GTPase interacts specifically with phosphatidylinositol 3-kinase. *Biochemical Journal*, 315(Part 3):775–779, MAY 1996.
- E Bonder, D Fishkind, and M Mooseker. Direct measurement of critical concentrations and assembly rate constants at the two ends of an actin filament. *Cell*, 34(2):491–501, SEP 1983.
- D Bottino, A Mogilner, T Roberts, M Stewart, and G Oster. How nematode sperm crawl. *Journal Of Cell Science*, 115(2):367–384, JAN 2002.
- DC Bottino and LJ Fauci. A computational model of ameboid deformation and locomotion. *European Biophysics Journal With Biophysics Letters*, 27(5):532–539, 1998.
- K Burridge. Signal transduction - crosstalk between Rac and Rho. *Science*, 283(5410):2028–2029, MAR 1999.
- K Burridge and K Wennerberg. Rho and Rac take center stage. *Cell*, 116(2):167–179, JAN 2004.
- LA Cameron, TM Svitkina, and D Vignjevic. Dendritic organization of actin comet tails. *Current Biology*, 11(2):130–135, 2001.
- AE Carlsson. Growth of branched actin networks against obstacles. *Biophysical Journal*, 81(4):1907–1923, OCT 2001.
- AE Carlsson, MA Wear, and JA Cooper. End versus side branching by Arp2/3 complex. *Biophysical Journal*, 86(2):1074–1081, FEB 2004.
- CY Chung, S Lee, C Briscoe, C Ellsworth, and RA Firtel. Role of Rac in controlling the actin cytoskeleton and chemotaxis in motile cells. *Proceedings Of The National Academy Of Sciences Of The United States Of America*, 97(10):5225–5230, MAY 2000.
- G Cicchetti, PG Allen, and M Glogauer. Chemotactic signaling pathways in neutrophils: From receptor to actin assembly. *Critical Reviews in Oral Biology and Medicine*, 13(3):220–228, 2002.

JS Da Silva, M Medina, C Zuliani, A Di Nardo, W Witke, and CG Dotti. RhoA/ROCK regulation of neuriteogenesis via profilin IIa-mediated control of actin stability. *Journal Of Cell Biology*, 162(7):1267–1279, SEP 2003.

AT Dawes, GB Ermentrout, EN Cytrynbaum, and L Edelstein-Keshet. Actin filament branching and protrusion velocity in a simple 1D model of a motile cell. *Journal of Theoretical Biology*, In Press, 2006.

RB Dickinson and DL Purich. Clamped-filament elongation model for actin-based motors. *Biophysical Journal*, 82(2):605–617, FEB 2002.

RB Dickinson, L Caro, and DL Purich. Force generation by cytoskeletal filament end-tracking proteins. *Biophysical Journal*, 87(4):2838–2854, OCT 2004.

MJ DiNubile and S Huang. High concentrations of phosphatidylinositol-4,5-bisphosphate may promote actin filament growth by three potential mechanisms: Inhibiting capping by neutrophil lysates, severing actin filaments and removing capping protein-beta(2) from barbed ends. *Biochimica et Biophysica Acta-Molecular Cell Research*, 1358(3):261–278, OCT 1997.

CG Dos Remedios, D Chhabra, M Kekic, IV Dedova, M Tsubakihara, DA Berry, and NJ Nosworthy. Actin binding proteins: Regulation of cytoskeletal microfilaments. *Physiological Reviews*, 83(2):433–473, APR 2003.

L Edelstein-Keshet. *Mathematical Models in Biology*. Random House, 1988.

L Edelstein-Keshet and GB Ermentrout. Models for spatial polymerization dynamics of rod-like polymers. *Journal Of Mathematical Biology*, 40(1):64–96, JAN 2000.

EH Egelman. The structure of f-actin. *Journal Of Muscle Research And Cell Motility*, 6(2):129–151, 1985.

H Falet, KM Hoffmeister, R Neujahr, JE Italiano, TP Stossel, FS Southwick, and JH Hartwig. Importance of free actin filament barbed ends for Arp2/3 complex function in platelets and fibroblasts. *Proceedings Of The National Academy Of Sciences Of The United States Of America*, 99(26):16782–16787, DEC 2002.

J Feinberg, O Kwiatek, C Astier, S Diennet, J Mery, F Heitz, Y Benyamin, and C Roustan. Capping and dynamic relation between domains 1 and 2 of gelsolin. *Journal Of Peptide Science*, 4(2):116–127, APR 1998.

PR Fisher, R Merkl, and G Gerisch. Quantitative-analysis of cell motility and chemotaxis in Dictyostelium-discoideum by using an image-processing system and a novel chemotaxis chamber providing stationary chemical gradients. *Journal Of Cell Biology*, 108(3):973–984, MAR 1989.

I Fujiwara, S Suetsugu, S Uemura, T Takenawa, and S Ishiwata. Visualization and force measurement of branching by Arp2/3 complex and N-WASP in actin filament. *Biochemical And Biophysical Research Communications*, 293(5):1550–1555, MAY 2002.

Y Fukumoto, K Kaibuchi, Y Hori, H Fujioka, S Araki, T Ueda, A Kikuchi, and Y Takai. Molecular-cloning and characterization of a novel type of regulatory protein (GDI) for the Rho proteins, Ras P21-like small GTP-binding proteins. *Oncogene*, 5(9):1321–1328, SEP 1990.

S Funamoto, R Meili, S Lee, L Parry, and RA Firtel. Spatial and temporal regulation of 3-phosphoinositides by PI 3-kinase and PTEN mediates chemotaxis. *Cell*, 109(5):611–623, MAY 2002.

A Gamba, A de Candia, S Di Talia, A Coniglio, F Bussolino, and G Serini. Diffusion-limited phase separation in eukaryotic chemotaxis. *Proceedings Of The National Academy Of Sciences Of The United States Of America*, 102(47):16927–16932, NOV 2005.

TS Gardner, CR Cantor, and JJ Collins. Construction of a genetic toggle switch in Escherichia coli. *Nature*, 403(6767):339–342, JAN 2000.

E Giniger. How do Rho family GTPases direct axon growth and guidance? a proposal relating signaling pathways to growth cone mechanics. *Differentiation*, 70(8):385–396, OCT 2002.

ME Gracheva and HG Othmer. A continuum model of motility in ameboid cells. *Bulletin Of Mathematical Biology*, 66(1):167–193, JAN 2004.

F Graner and JA Glazier. Simulation of biological cell sorting using a 2-dimensional extended potts-model. *Physical Review Letters*, 69(13):2013–2016, SEP 1992.

- HP Grimm, AB Verkhovsky, A Mogilner, and JJ Meister. Analysis of actin dynamics at the leading edge of crawling cells: implications for the shape of keratocyte lamellipodia. *European Biophysics Journal With Biophysics Letters*, 32(6):563–577, OCT 2003.
- RA Gungabissoon and JR Bamburg. Regulation of growth cone actin dynamics by ADF/cofilin. *Journal of Histochemistry and Cytochemistry*, 51(4):411–420, APR 2003.
- L Harrison. *Kinetic theory of living pattern*. Cambridge University Press, 1993.
- PT Hawkins, A Eguinoa, RG Qiu, D Stokoe, FT Cooke, R Walters, S Wennstrom, L Claessonwelsch, T Evans, M Symons, and L Stephens. PDGF stimulates an increase in GTP-Rac via activation of phosphoinositide 3-kinase. *Current Biology*, 5(4):393–403, APR 1995.
- JH Henson, TM Svitkina, AR Burns, HE Hughes, KJ MacPartland, R Nazarian, and GG Borisy. Two components of actin-based retrograde flow in sea urchin coelomocytes. *Molecular Biology Of The Cell*, 10(12):4075–4090, DEC 1999.
- HN Higgs and TD Pollard. Activation by Cdc42 and PIP2 of wiskott-aldrich syndrome protein (WASP) stimulates actin nucleation by Arp2/3 complex. *Journal Of Cell Biology*, 150(6):1311–1320, SEP 2000.
- C Huang, Z Rajfur, C Borchers, MD Schaller, and K Jacobson. Jnk phosphorylates paxillin and regulates cell migration. *Nature*, 424(6945):219–223, JUL 2003a.
- YE Huang, M Iijima, CA Parent, S Funamoto, RA Firtel, and P Devreotes. Receptor-mediated regulation of PI3Ks confines PI(3,4,5)P-3 to the leading edge of chemotaxing cells. *Molecular Biology Of The Cell*, 14(5):1913–1922, MAY 2003b.
- M Iijima and P Devreotes. Tumor suppressor PTEN mediates sensing of chemoattractant gradients. *Cell*, 5(109):599–610, MAY 2002.
- M Iijima, YE Huang, and P Devreotes. Temporal and spatial regulation of chemotaxis. *Developmental Cell*, 3(4):469–478, OCT 2002.
- RH Insall and OD Weiner. PIP3, PIP2, and cell movement - Similar messages, different meanings? *Developmental Cell*, 1(6):743–747, DEC 2001.
- A Jacinto and L Wolpert. Filopodia. *Current Biology*, 11(16):R634–R634, AUG 2001.

C Janetopoulos, L Ma, PN Devreotes, and PA Iglesias. Chemoattractant-induced phosphatidylinositol 3,4,5-trisphosphate accumulation is spatially amplified and adapts, independent of the actin cytoskeleton. *Proceedings Of The National Academy Of Sciences Of The United States Of America*, 101(24):8951–8956, JUN 2004.

A Jilkin. Mathematical study of Rho GTPases in motile cells. Master's thesis, University of British Columbia, 2005.

GE Jones, WE Allen, and AJ Ridley. The Rho GTPases in macrophage motility and chemotaxis. *Cell Adhesion And Communication*, 6(2–3):237–245, 1998.

C Jurado, JR Haserick, and J Lee. Slipping or gripping? Fluorescent speckle microscopy in fish keratocytes reveals two different mechanisms for generating a retrograde flow of actin. *Molecular Biology Of The Cell*, 16(2):507–518, FEB 2005.

K Kalil and EW Dent. Touch and go: guidance cues signal to the growth cone cytoskeleton. *Current Opinion In Neurobiology*, 15(5):521–526, OCT 2005.

M Kanehisa, S Goto, M Hattori, KF Aoki-Kinoshita, M Itoh, S Kawashima, T Katayama, M Araki, , and M Hirakawa. From genomics to chemical genomics: new developments in KEGG. *Nucleic Acids Research*, 34:D354–D357, 2006.

R Kozma, S Ahmed, A Best, and L Lim. The Ras-related protein Cdc42HS and bradykinin promote formation of peripheral actin microspikes and filopodia in Swiss 3T3 fibroblasts. *Molecular And Cellular Biology*, 15(4):1942–1952, APR 1995.

VS Kraynov, C Chamberlain, GM Bokoch, MA Schwartz, S Slabaugh, and KM Hahn. Localized Rac activation dynamics visualized in living cells. *Science*, 290(5490):333–337, OCT 2000.

J Krishnan and PA Iglesias. A modeling framework describing the enzyme regulation of membrane lipids underlying gradient perception in Dictyostelium cells. *Journal Of Theoretical Biology*, 229(1):85–99, JUL 2004.

DF Kucik, EL Elson, and MP Sheetz. Cell migration does not produce membrane flow. *Journal Of Cell Biology*, 111(4):1617–1622, OCT 1990.

TB Kuhn, PJ Meberg, MD Brown, BW Bernstein, LS Minamide, JR Jensen, K Okada, EA Soda, and JR Bamburg. Regulating actin dynamics in neuronal growth genes by ADF/cofilin and Rho family GTPases. *Journal Of Neurobiology*, 44(2):126–144, AUG 2000.

VM Laurent, S Kasas, A Yersin, TE Schaffer, S Catsicas, G Dietler, AB Verkhovsky, and JJ Meister. Gradient of rigidity in the lamellipodia of migrating cells revealed by atomic force microscopy. *Biophysical Journal*, 89(1):667–675, JUL 2005.

A Levchenko and PA Iglesias. Models of eukaryotic gradient sensing: Application to chemotaxis of amoebae and neutrophils. *Biophysical Journal*, 82(1):50–63, JAN 2002.

Z Li, CD Aizenman, and HT Cline. Regulation of Rho GTPases by crosstalk and neuronal activity in vivo. *Neuron*, 33(5):741–750, FEB 2002.

Z Li, M Hannigan, ZC Mo, B Liu, W Lu, Y Wu, AV Smrcka, GQ Wu, L Li, MY Liu, CK Huang, and DQ Wu. Directional sensing requires G beta gamma-mediated PAK1 and PIX alpha-dependent activation of Cdc42. *Cell*, 114(2):215–227, JUL 2003.

Z Li, XM Dong, ZL Wang, WZ Liu, N Deng, Y Ding, LY Tang, T Hla, R Zeng, L Li, and DQ Wu. Regulation of PTEN by Rho small GTPases. *Nature Cell Biology*, 7(4):399–U42, APR 2005.

CH Lin, EM Espreafico, MS Mooseker, and P Forscher. Myosin drives retrograde F-actin flow in neuronal growth cones. *Neuron*, 16(4):769–782, APR 1996.

M Lorenz, V DesMarais, F Macaluso, RH Singer, and J Condeelis. Measurement of barbed ends, actin polymerization, and motility in live carcinoma cells after growth factor stimulation. *Cell Motility And The Cytoskeleton*, 57(4):207–217, APR 2004.

L Ma, LC Cantley, PA Janmey, and MW Kirschner. Corequirement of specific phosphoinositides and small GTP binding protein Cdc42 in inducing actin assembly in *Xenopus* egg extracts. *Journal Of Cell Biology*, 140(5):1125–1136, MAR 1998.

L Ma, C Janetopoulos, L Yang, PN Devreotes, and PA Iglesias. Two complementary, local excitation, global inhibition mechanisms acting in parallel can explain the chemoattractant-induced regulation of PI(3,4,5)P-3 response in *Dictyostelium* cells. *Biophysical Journal*, 87(6):3764–3774, DEC 2004.

DJG Mackay and A Hall. Rho GTPases. *Journal Of Biological Chemistry*, 273(33):20685–20688, AUG 1998.

P Madaule and R Axel. A novel Ras-related gene family. *Cell*, 41(1):31–40, 1985.

IV Maly and GG Borisy. Self-organization of a propulsive actin network as an evolutionary process. *Proceedings of the National Academy of Sciences of the United States of America*, 98(20):11324–11329, SEP 2001.

AFM Marée, A Jilkiné, A Dawes, VA Grieneisen, and L Edelstein-Keshet. Polarisation and movement of keratocytes: a multiscale modelling approach. *Bulletin of Mathematical Biology*, In Press, 2006.

TFJ Martin. Phosphoinositide lipids as signaling molecules: Common themes for signal transduction, cytoskeletal regulation, and membrane trafficking. *Annual Review Of Cell And Developmental Biology*, 14:231–264, 1998.

T Matozaki, H Nakanishi, and Y Takai. Small G-protein networks - their crosstalk and signal cascades. *Cellular Signalling*, 12(8):515–524, AUG 2000.

H Meinhardt. Orientation of chemotactic cells and growth cones: models and mechanisms. *Journal Of Cell Science*, 112(17):2867–2874, SEP 1999.

KF Meiri. Lipid rafts and regulation of the cytoskeleton during t cell activation. *Philosophical Transactions of the Royal Society B-Biological Sciences*, 360(1461):1663–1672, SEP 2005.

MR Mejillano, S Kojima, DA Applewhite, FB Gertler, TM Svitkina, and GG Borisy. Lamellipodial versus filopodial mode of the actin nanomachinery: Pivotal role of the filament barbed end. *Cell*, 118(3):363–373, AUG 2004.

S Merlot and RA Firtel. Leading the way: directional sensing through phosphatidylinositol 3-kinase and other signaling pathways. *Journal Of Cell Science*, 116(17):3471–3478, SEP 2003.

D Michaelson, J Silletti, G Murphy, P Eustachio, M Rush, and MR Philips. Differential localization of Rho GTPases in live cells: Regulation by hypervariable regions and RhoGDI binding. *Journal Of Cell Biology*, 152(1):111–126, JAN 2001.

Y Miura, A Kikuchi, T Musha, S Kuroda, H Yaku, T Sasaki, and Y Takai. Regulation of morphology by Rho P21 and its inhibitory GDP/GTP exchange protein (Rho GDI) in Swiss 3T3 cells. *Journal Of Biological Chemistry*, 268(1):510–515, JAN 1993.

A Mogilner and L Edelstein-Keshet. Regulation of actin dynamics in rapidly moving cells: A quantitative analysis. *Biophysical Journal*, 83(3):1237–1258, SEP 2002.

A Mogilner and G Oster. Force generation by actin polymerization II: The elastic ratchet and tethered filaments. *Biophysical Journal*, 84(3):1591–1605, MAR 2003.

A Mogilner and G Oster. Cell motility driven by actin polymerization. *Biophysical Journal*, 71(6):3030–3045, DEC 1996.

SY Moon and Y Zheng. Rho GTPase-activating proteins in cell regulation. *Trends In Cell Biology*, 13(1):13–22, JAN 2003.

RD Mullins, JA Heuser, and TD Pollard. The interaction of Arp2/3 complex with actin: Nucleation, high affinity pointed end capping, and formation of branching networks of filaments. *Proceedings of the National Academy of Sciences of the United States of America*, 95(11):6181–6186, MAY 1998.

P Nalbant, L Hodgson, V Kraynov, A Touthkine, and KM Hahn. Activation of endogenous Cdc42 visualized in living cells. *Science*, 305(5690):1615–1619, SEP 2004.

A Narang. Spontaneous polarization in eukaryotic gradient sensing: A mathematical model based on mutual inhibition of frontness and backness pathways. *Journal of Theoretical Biology*, In press, 2006.

A Narang, KK Subramanian, and DA Lauffenburger. A mathematical model for chemoattractant gradient sensing based on receptor-regulated membrane phospholipid signaling dynamics. *Annals Of Biomedical Engineering*, 29(8):677–691, AUG 2001.

CD Nobes and A Hall. Rho, Rac and Cdc42 GTPases regulate the assembly of multimolecular focal complexes associated with actin stress fibers, lamellipodia, and filopodia. *Cell*, 81(1):53–62, APR 1995.

JS Orange, KD Stone, SE Turvey, and K Krzewski. The Wiskott-Aldrich syndrome. *Cellular And Molecular Life Sciences*, 61(18):2361–2385, SEP 2004.

- G Oster. Brownian ratchets: Darwin's motors. *Nature*, 417(6884):25–25, MAY 2002.
- NB Ouchi, JA Glazier, JP Rieu, A Upadhyaya, and Y Sawada. Improving the realism of the cellular potts model in simulations of biological cells. *Physica A - Statistical Mechanics And Its Applications*, 329(3–4):451–458, NOV 2003.
- D Pantaloni, R Boujemaa, D Didry, P Gounon, and MF Carrier. The Arp2/3 complex branches filament barbed ends: functional antagonism with capping proteins. *Nature Cell Biology*, 2(7):385–391, JUL 2000.
- CS Peskin, GM Odell, and GF Oster. Cellular motions and thermal fluctuations - the Brownian ratchet. *Biophysical Journal*, 65(1):316–324, JUL 1993.
- TD Pollard. Rate constants for the reactions of ATP-actin and ADP-actin with the ends of actin-filaments. *Journal Of Cell Biology*, 103(6):2747–2754, 1986.
- TD Pollard and GG Borisy. Cellular motility driven by assembly and disassembly of actin filaments. *Cell*, 112(4):453–465, FEB 2003.
- TD Pollard, L Blanchoin, and RD Mullins. Molecular mechanisms controlling actin filament dynamics in nonmuscle cells. *Annual Review Of Biophysics And Biomolecular Structure*, 29:545–576, 2000.
- A Ponti, M Machacek, SL Gupton, CM Waterman-Storer, and G Danuser. Two distinct actin networks drive the protrusion of migrating cells. *Science*, 305(5691):1782–1786, SEP 2004.
- A Ponti, A Matov, M Adams, S Gupton, CM Waterman-Storer, and G Danuser. Periodic patterns of actin turnover in lamellipodia and lamellae of migrating epithelial cells analyzed by quantitative fluorescent speckle microscopy. *Biophysical Journal*, 89(5):3456–3469, NOV 2005.
- M Postma and PJM Van Haastert. A diffusion-translocation model for gradient sensing by chemotactic cells. *Biophysical Journal*, 81(3):1314–1323, SEP 2001.
- M Postma, L Bosgraaf, HM Looovers, and PJM Van Haastert. Chemotaxis: signalling modules join hands at front and tail. *Embo Reports*, 5(1):35–40, JAN 2004.
- WH Press, SA Teukolsky, WT Vetterling, and BP Flannery. *Numerical Recipes in C*. Cambridge University Press, 2 edition, 1992.

- M Raftopoulou and A Hall. Cell migration: Rho GTPases lead the way. *Developmental Biology*, 265(1):23–32, JAN 2004.
- LE Rameh and LC Cantley. The role of phosphoinositide 3-kinase lipid products in cell function. *Journal Of Biological Chemistry*, 274(13):8347–8350, MAR 1999.
- T Redmond and SH Zigmond. Distribution of F-actin elongation sites in lysed polymorphonuclear leukocytes parallels the distribution of endogenous F-actin. *Cell Motility And The Cytoskeleton*, 26(1):7–18, 1993.
- AJ Ridley. Rho GTPases and cell migration. *Journal of Cell Science*, 114(15):2713–2722, AUG 2001a.
- AJ Ridley. Rho proteins: Linking signaling with membrane trafficking. *Traffic*, 2(5):303–310, MAY 2001b.
- AJ Ridley. Rho family proteins: coordinating cell responses. *Trends in Cell Biology*, 11(12):471–477, DEC 2001c.
- AJ Ridley, MA Schwartz, K Burridge, RA Firtel, MH Ginsberg, G Borisy, JT Parsons, and AR Horwitz. Cell migration: Integrating signals from front to back. *Science*, 302(5651):1704–1709, DEC 2003.
- R Rohatgi, L Ma, H Miki, M Lopez, T Kirchhausen, T Takenawa, and MW Kirschner. The interaction between N-WASP and the Arp2/3 complex links Cdc42-dependent signals to actin assembly. *Cell*, 97(2):221–231, APR 1999.
- R Rohatgi, P Nollau, HYH Ho, MW Kirschner, and BJ Mayer. Nck and phosphatidylinositol 4,5-bisphosphate synergistically activate actin polymerization through the N-WASP-Arp2/3 pathway. *Journal Of Biological Chemistry*, 276(28):26448–26452, JUL 2001.
- Y Sako, K Hibino, T Miyauchi, Y Miyamoto, M Ueda, and T Yanagida. Single-molecule imaging of signaling molecules in living cells. *Single Molecules*, 2(1):159–163, 2000.
- Y Sakumura, Y Tsukada, N Yamamoto, and S Ishii. A molecular model for axon guidance based on cross talk between Rho GTPases. *Biophysical Journal*, 89(2):812–822, AUG 2005.
- JM Sanger, R Chang, and F Ashton. Novel form of actin-based motility transports bacteria on the surfaces of infected cells. *Cell Motility and the Cytoskeleton*, 34(4):279–287, 1996.

DA Schafer, PB Jennings, and JA Cooper. Dynamics of capping protein and actin assembly in vitro: Uncapping barbed ends by polyphosphoinositides. *Journal Of Cell Biology*, 135(1):169–179, OCT 1996.

A Schmidt and A Hall. Guanine nucleotide exchange factors for Rho GTPases: turning on the switch. *Genes & Development*, 16(13):1587–1609, JUL 2002.

AAP Schmitz, EE Govek, B Bottner, and van Aelst L. Rho GTPases: Signaling, migration, and invasion. *Experimental Cell Research*, 261(1):1–12, NOV 2000.

G Servant, OD Weiner, P Herzmark, T Balla, JW Sedat, and HR Bourne. Polarization of chemoattractant receptor signaling during neutrophil chemotaxis. *Science*, 287(5455):1037–1040, FEB 2000.

JV Small, M Herzog, and K Anderson. Actin filament organization in the fish keratocyte lamellipodium. *Journal Of Cell Biology*, 129(5):1275–1286, JUN 1995.

JV Small, T Stradal, E Vignal, and K Rottner. The lamellipodium: where motility begins. *Trends In Cell Biology*, 12(3):112–120, MAR 2002.

S Srinivasan, F Wang, S Glavas, A Ott, F Hofmann, K Aktories, D Kalman, and HR Bourne. Rac and Cdc42 play distinct roles in regulating PI(3,4,5)P-3 and polarity during neutrophil chemotaxis. *Journal of Cell Biology*, 160(3):375–385, FEB 2003.

PRH Stark, LJ Rinko, and DN Larson. Fluorescent resolution target for super-resolution microscopy. *Journal of Microscopy - Oxford*, 212:307–310, 2003.

H Sternmark. *Phosphatidylinositol 3-kinase and membrane trafficking*, pages 32–108. Oxford University Press, Oxford, UK, 2000.

KK Subramanian and A Narang. A mechanistic model for eukaryotic gradient sensing: Spontaneous and induced phosphoinositide polarization. *Journal Of Theoretical Biology*, 231(1):49–67, NOV 2004.

S Suetsugu, H Miki, H Yamaguchi, T Obinata, and T Takenawa. Enhancement of branching efficiency by the actin filament-binding activity of N-WASP/WAVE2. *Journal Of Cell Science*, 114(24):4533–4542, DEC 2001.

- S Suetsugu, H Miki, and T Takenawa. Spatial and temporal regulation of actin polymerization for cytoskeleton formation through Arp2/3 complex and WASP/WAVE proteins. *Cell Motility and the Cytoskeleton*, 51(3):113–122, MAR 2002.
- TM Svitkina and GG Borisy. Arp2/3 complex and actin depolymerizing factor cofilin in dendritic organization and treadmilling of actin filament array in lamellipodia. *Journal Of Cell Biology*, 145(5):1009–1026, MAY 1999.
- TM Svitkina, AB Verkhovsky, KM McQuade, and GG Borisy. Analysis of the actin-myosin II system in fish epidermal keratocytes: mechanism of cell body translocation. *Journal of Cell Biology*, 139(2):397–415, OCT 1997.
- MH Symons and TJ Mitchison. Control of actin polymerization in live and permeabilized fibroblasts. *Journal Of Cell Biology*, 114(3):503–513, AUG 1991.
- Y Takai, T Sasaki, and T Matozaki. Small GTP-binding proteins. *Physiological Reviews*, 81(1):153–208, JAN 2001.
- JA Theriot and TJ Mitchison. Actin microfilament dynamics in locomoting cells. *Nature*, 352(6331):126–131, JUL 1991.
- A Toker. Phosphoinositides and signal transduction. *Cellular And Molecular Life Sciences*, 59(5):761–779, MAY 2002.
- KF Tolias, LC Cantley, and CL Carpenter. Rho-family GTPases bind to phosphoinositide kinases. *Journal Of Biological Chemistry*, 270(30):17656–17659, JUL 1995.
- KF Tolias, JH Hartwig, H Ishihara, Y Shibasaki, LC Cantley, and CL Carpenter. Type I alpha phosphatidylinositol-4-phosphate 5-kinase mediates Rac-dependent actin assembly. *Current Biology*, 10(3):153–156, FEB 2000.
- P Vallotton, SL Gupton, CM Waterman-Storer, and G Danuser. Simultaneous mapping of filamentous actin flow and turnover in migrating cells by quantitative fluorescent speckle microscopy. *Proceedings Of The National Academy Of Sciences Of The United States Of America*, 101(26):9660–9665, JUN 2004.

P Vallotton, G Danuser, S Bohnet, JJ Meister, and AB Verkhovsky. Tracking retrograde flow in keratocytes: News from the front. *Molecular Biology Of The Cell*, 16(3):1223–1231, MAR 2005.

PB van Hennik, JP ten Klooster, JR Halstead, C Voermans, EC Anthony, N Divecha, and PL Hordijk. The C-terminal domain of Rac1 contains two motifs that control targeting and signaling specificity. *Journal Of Biological Chemistry*, 278(40):39166–39175, OCT 2003.

AB Verkhovsky, OY Chaga, S Schaub, TM Svitkina, JJ Meister, and GG Borisy. Orientational order of the lamellipodial actin network as demonstrated in living motile cells. *Molecular Biology Of The Cell*, 14(11):4667–4675, NOV 2003.

F Wang, P Herzmark, OD Weiner, S Srinivasan, G Servant, and HR Bourne. Lipid products of PI(3)Ks maintain persistent cell polarity and directed motility in neutrophils. *Nature Cell Biology*, 4(7):513–518, JUL 2002.

R Wedlich-Soldner and R Li. Spontaneous cell polarization: undermining determinism. *Nature Cell Biology*, 5(4):267–270, APR 2003.

R Wedlich-Soldner, SJ Altschuler, LF Wu, and R Li. Spontaneous cell polarization through actomyosin-based delivery of the Cdc42 GTPase. *Science*, 299(5610):1231–1235, FEB 2003.

B Wehrle-Haller and BA Imhof. The inner lives of focal adhesions. *Trends In Cell Biology*, 12(8):382–389, AUG 2002.

OD Weiner, G Servant, MD Welch, TJ Mitchison, JW Sedat, and HR Bourne. Spatial control of actin polymerization during neutrophil chemotaxis. *Nature Cell Biology*, 1(2):75–81, JUN 1999.

OD Weiner, PO Neilsen, GD Prestwich, MW Kirschner, LC Cantley, and HR Bourne. A PtdInsP(3)- and Rho GTPase-mediated positive feedback loop regulates neutrophil polarity. *Nature Cell Biology*, 4(7):509–512, JUL 2002.

HCE Welch, WJ Coadwell, CD Ellson, GJ Ferguson, SR Andrews, H Erdjument-Bromage, P Tempst, PT Hawkins, and LR Stephens. P-Rex1, a PtdIns(3,4,5)P-3- and G beta gamma-regulated guanine-nucleotide exchange factor for Rac. *Cell*, 108(6):809–821, MAR 2002.

- HCE Welch, WJ Coadwell, LR Stephens, and PT Hawkins. Phosphoinositide 3-kinase-dependent activation of Rac. *Febs Letters*, 546(1):93-97, JUL 2003.
- S Wiesner, E Helfer, D Didry, G Ducouret, F Lafuma, MF Carrier, and D Pantaloni. A biomimetic motility assay provides insight into the mechanism of actin-based motility. *Journal Of Cell Biology*, 160(3):387-398, FEB 2003.
- T Wittmann and CM Waterman-Storer. Cell motility: can Rho GTPases and microtubules point the way? *Journal of Cell Science*, 114(21):3795-3803, 2001.
- K Wong, O Pertz, K Hahn, and H Bourne. Neutrophil polarization: Spatiotemporal dynamics of RhoA activity support a self-organizing mechanism. *Proceedings Of The National Academy Of Sciences Of The United States Of America*, 103(10):3639-3644, MAR 2006.
- W Wood and P Martin. Structures in focus - filopodia. *International Journal of Biochemistry and Cell Biology*, 34(7):726-730, JUL 2002.
- JS Xu, F Wang, A Van Keymeulen, P Herzmark, A Straight, K Kelly, Y Takuwa, N Sugimoto, T Mitchison, and HR Bourne. Divergent signals and cytoskeletal assemblies regulate self-organizing polarity in neutrophils. *Cell*, 114(2):201-214, JUL 2003.
- Y Yamaguchi, H Katoh, and H Yasui. RhoA inhibits the nerve growth factor-induced Rac1 activation through Rho-associated kinase-dependent pathway. *Journal of Biological Chemistry*, 276(22):18977-18983, JUN 2001.
- H Yasui, H Katoh, Y Yamaguchi, J Aoki, H Fujita, K Mori, and M Negishi. Differential responses to nerve growth factor and epidermal growth factor in neurite outgrowth of PC12 cells are determined by Rac1 activation systems. *Journal Of Biological Chemistry*, 276(18):15298-15305, MAY 2001.
- BL Zhang and Y Zheng. Regulation of RhoA GTP hydrolysis by the GTPase-activating proteins p190, p50RhoGAP, Bcr, and 3BP-1. *Biochemistry*, 37(15):5249-5257, APR 1998.
- Y Zheng. Dbl family guanine nucleotide exchange factors. *Trends In Biochemical Sciences*, 26(12):724-732, DEC 2001.
- Y Zheng, S Bagrodia, and RA Cerione. Activation of phosphoinositide 3-kinase activity by Cdc42HS binding to P85. *Journal Of Biological Chemistry*, 269(29):18727-18730, JUL 1994.

Appendix A

C code for simulating Equations (4.1)

Following is the C code for simulation Equations (4.1), the equations for actin dynamics in travelling coordinates, $\tau = t$, $z = x - x'_{edge}t$, where x'_{edge} is the speed of the membrane. In the code, I use c to denote the membrane speed. I do not assume it is constant and determine the membrane speed at every time step according to the number of barbed ends at the membrane.

```
//baf.c
//This program simulates barbed ends, Arp2/3 and filament density
//in a 1D domain
#include <stdio.h>
#include <math.h>
#include <stdlib.h>
#include <errno.h>
#include <time.h>

#define N 1001//number of grid spaces in the domain
//N=(int)(L/(dz))+1 where L is the length of the domain,
//10 \mu m and dz is the space step declared below
//The left boundary (grid space = 1) is the back of the cell,
//the right boundary (grid space = N-2) is the front of the cell.
//Grid spaces 0 and N-1 are used for declaring boundary conditions.

int main() {

    //variable declarations: barbed ends (b), Arp2/3 (a), filament density (f)
    double b[N], a[N], f[N];
    double bnew[N], anew[N], fnew[N];
    //parameter declarations
    double h0, h1, h2, v, kappa, Dr, gamma, c, w, A0;
    double dz=0.010, dt, total, num;
    int z, t;

    //assigning parameter values
    h0=0;//spontaneous branching rate
    h1=0;//tip branching rate
    h2=25.0;//side branching rate

    v=0.3;//polymerization speed
    kappa=1.0;//capping rate
```

```

Dr=3.0;//Arp/3 diffusion rate
gamma=0.03;//filament decay rate
w=5.0;//membrane resistance
A0=1;//Arp2/3 membrane source

dt=dz*dz/(20*Dr);//calculating the time step for numerical stability
total=200/dt;//total simulation time

num=(double)N;//converting the domain size to a double to use in calculations

//initial conditions: barbed ends have a linear gradient while Arp2/3
//and filament density is initially zero.
for(z=0;z<=N-1;z++) {
    b[z]=z/(num-1); bnew[z]=b[z];
    a[z]=0; anew[z]=a[z];
    f[z]=0; fnew[z]=f[z];
}

//boundary conditions
b[0]=0; bnew[0]=b[0]; //B(-infty)=0
a[0]=0; anew[0]=a[0]; //A(-infty)=0
a[N-1]=A0; anew[N-1]=a[N-1]; //A(x_{edge})=A0
f[N-1]=0; fnew[N-1]=f[N-1]; //F(x_{edge})=0

for(t=0;t<total;t++) {

    //calculating the membrane speed according to the thermal ratchet
    //according to the number of barbed ends at the membrane
    if(b[N-2]>0) c=v*exp(-w/b[N-2]);
    else c=0;// if there are no barbed ends, membrane speed is zero

    //calculating the values of barbed ends (b), Arp2/3 (r) and
    //filament density (f) in each interior grid space
    for(z=1;z<=N-2;z++) {
        bnew[z]=b[z]+dt*(h0*a[z]+h1*a[z]*b[z]+h2*a[z]*f[z]-kappa*b[z]
            +(c-v)*(b[z]-b[z-1])/dz);
        anew[z]=a[z]+dt*(Dr*(a[z+1]+a[z-1]-2*a[z])/(dz*dz)-h0*a[z]
            -h1*a[z]*b[z]-h2*a[z]*f[z]);
        fnew[z]=f[z]+dt*(v*b[z]-gamma*f[z]+c*(f[z+1]-f[z])/dz);
    }

    //updating the variables
    for(z=1;z<=N-2;z++) {
        b[z]=bnew[z]; a[z]=anew[z]; f[z]=fnew[z];
    }

}

//print the spatial profile of each variable at the end of the program
for(z=1;z<=N-2;z++) printf("%f %f %f %f\n",(z-1)*dz-4,b[z],a[z],f[z]);

```

```
    return(0);  
}
```